MESOSCALE ENSEMBLE-BASED DATA ASSIMILATION AND PARAMETER ESTIMATION

A Dissertation

by

ALTUG AKSOY

Submitted to the Office of Graduate Studies of
Texas A&M University
in partial fulfillment of the requirements for the degree of

DOCTOR OF PHILOSOPHY

August 2005

Major Subject: Atmospheric Sciences

MESOSCALE ENSEMBLE-BASED DATA ASSIMILATION AND PARAMETER ESTIMATION

A Dissertation

by

ALTUG AKSOY

Submitted to the Office of Graduate Studies of
Texas A&M University
in partial fulfillment of the requirements for the degree of

DOCTOR OF PHILOSOPHY

Approved by:

Co-Chairs of Committee,	Fuqing Zhang
	John W. Nielsen-Gammon
Committee Members,	Lee Panetta
	Ping Chang
	Chris Snyder
Head of Department,	Richard R. Orville

August 2005

Major Subject: Atmospheric Sciences

ABSTRACT

Mesoscale Ensemble-Based Data Assimilation

and Parameter Estimation. (August 2005)

Altug Aksoy, B.S., Bogazici University;

M.B.A., The George Washington University

Co-Chairs of Advisory Committee: Dr. Fuqing Zhang
Dr. John W. Nielsen-Gammon

The performance of the ensemble Kalman filter (EnKF) in forced, dissipative flow under imperfect model conditions is investigated through simultaneous state and parameter estimation where the source of model error is the uncertainty in the model parameters. Two numerical models with increasing complexity are used with simulated observations.

For lower complexity, a two-dimensional, nonlinear, hydrostatic, non-rotating, and incompressible sea breeze model is developed with buoyancy and vorticity as the prognostic variables. Model resolution is 4 km horizontally and 50 m vertically. The ensemble size is set at 40. Forcing is maintained through an explicit heating function with additive stochastic noise. Simulated buoyancy observations on land surface with 40-km spacing are assimilated every 3 hours. Up to six model parameters are successfully subjected to estimation attempts in various experiments. The overall EnKF performance in terms of the error statistics is found to be superior to the worst-case

scenario (when there is parameter error but no parameter estimation is performed) with an average error reduction in buoyancy and vorticity of 40% and 46%, respectively, for the simultaneous estimation of six parameters.

The model chosen to represent the complexity of operational weather forecasting is the Pennsylvania State University-National Center for Atmospheric Research MM5 model with a 36-km horizontal resolution and 43 vertical layers. The ensemble size for all experiments is chosen as 40 and a 41st member is generated as the truth with the same ensemble statistics. Assimilations are performed with a 12-hour interval with simulated sounding and surface observations of horizontal winds and temperature. Only single-parameter experiments are performed focusing on a constant inserted into the code as the multiplier of the vertical eddy mixing coefficient. Estimation experiments produce very encouraging results and the mean estimated parameter value nicely converges to the true value exhibiting a satisfactory level of variability.

DEDICATION

To my father

ACKNOWLEDGEMENTS

I would like to thank my advisors, Dr. Fuqing Zhang and Dr. John Nielsen-Gammon, for their tremendous support throughout this long and painful process. I am also grateful to my committee members, Dr. Lee Panetta, Dr. Ping Chang, and Dr. Chris Snyder, for their guidance and help. Many people in the Department of Atmospheric Sciences have also given me help and support for which I am very thankful. Dr. Gerald North has offered me support and wisdom at some very difficult times. Office staff, Pat Price, Barbara Straube, Jen Schwartz and Mary Gammon have offered help whenever I needed it. Finally, the members of our research group made this a very enjoyable working environment. I am especially thankful to Ellie Meng for her great technical support in many different areas and also for the many fruitful discussions.

Thanks to my friends and my family for believing in me and being patient at some very busy and tough times. My friends in College Station have become almost a second family to me and without them, I cannot imagine how I would have achieved all of this. My family, my mother Emel, my father Erdal, and my sister Gultug, have been my greatest support and inspiration throughout my life. I am most indebted to them for always being there for me. Finally, my girlfriend, Seniz, has stood by me with tremendous patience at my worst times and I am very grateful for that.

This research was sponsored by the EPA grant to Texas A&M University through the University of Houston, GTRI/HARC Project No. H24-2003, and the NSF grant ATM-0205599.

TABLE OF CONTENTS

Page

Page

LIST OF FIGURES

Page

Page

Page

Page

Page

Page

Page

Page

Page

LIST OF TABLES

Page

INTRODUCTION

Since its onset in the 1950s and during its explosive development from the 1960s forward, numerical modeling has been by far the most extensively employed tool in the attempt to predict the Earth's atmosphere, which has perhaps been subjected to such prediction attempts more than any other fluid system. Being a chaotic system, the atmosphere exhibits a very strong sensitivity on initial conditions. As a consequence, the improvement of the quality of initial conditions has been one of the major foci of numerical weather prediction (NWP) research. In this respect, data assimilation has emerged as the tool for estimation of the state of the atmosphere. Data assimilation can be briefly defined as the cumulative effort to combine all available information to estimate the best possible initial state of a system (Talagrand 1997). In meteorology, this data includes observations, the current model state (background information) and the uncertainties associated with each (Ham 2002). Mesoscale phenomena, in this context, are processes that occur on the scale of a few tens of kilometers to a few hundred kilometers and include such structures as jet streaks, fronts, and squall lines (Holton 1992). Among various data assimilation schemes, ensemble-based estimation techniques (such as ensemble Kalman filtering) have recently attracted much attention. Not only do they approximate the best linear unbiased estimate of the initial state, but they also offer a numerically economical way to estimate the background error covariance matrix.

This dissertation follows the style of *Journal of the Atmospheric Sciences*.

Another major limitation of NWP models pertains to the fact that even with perfect initial conditions, numerical models can be expected to quickly diverge from the true state of the atmosphere. Commonly known as model error, this divergence usually arises from such factors as misrepresentation of the actual physical system, numerics, resolution, boundary conditions, and parameterization of unresolved processes. Unlike imperfect initial conditions, influences of model error on the structure and propagation of forecast error covariances have received limited attention, both because many difficulties exist for assessing model error characteristics objectively and because of the immensely complicated and application-dependent nature of errors associated with operational models (Dee 1995; Etherton and Bishop 2004).

The recent trend in the research on model error has evolved into two branches. On one hand, limited (until very recently) attention has been focused on the dynamical properties of model error. Vukicevic and Errico (1990) compared error properties of global models and limited-area models as a function of lateral boundary conditions and domain size, although their primary concern was predictability rather than the structure of model error itself. Schubert and Chang (1996) used the output of the analysis of a general circulation model (GCM) in a multivariate regression model to establish a linear relationship between the random fluctuations of the analysis increments and the forcing terms of the GCM, constraining the systematic error of their regression model to be equal to zero. They also noted that such an approach may fail if appropriate corrections are not linear or the GCM does not include a physical process that is important in nature. In more recent years, research on model error appears to have intensified. A common

theme that has emerged from these very recent studies is the fact that error growth properties critically depend on the statistical properties of model error. To this end, Vannitsem and Toth (2002) investigated, both analytically and in a low-order chaotic atmospheric system, the relationship between short-time growth of mean square error and autocorrelation of model error when initial conditions are perfect. They observed that while mean error growth was linear in time for white-noise model error, it became quadratic for red-noise model error. In a complementing study, Nicolis (2003) showed that small deterministic parametric error (as opposed to the stochastic model error in Vannitsem and Toth) universally leads to short-time quadratic mean-square error behavior while also revealing that the probabilistic nature of model error is non-Markovian (exhibits infinite memory), insofar as model error is expressible in a functional form involving model variables. By a similar approach, Vannitsem (2003) investigated characteristics of model error due to boundary conditions in nested limited-area models while Nicolis (2004) analyzed the effects of omission of processes due to unresolved scales.

A second and much more popular route to accounting for model error has been the attempt to apply data assimilation techniques to the estimation of model error itself. One such branch of studies deals with the estimation of systematic forecast error (bias) through the use of weak-constraint four-dimensional variational (4DVAR) assimilation schemes. Derber (1989), in the context of a quasi-geostrophic model, successfully employed an additional bias term at the forecast step that is a product of a spatially-distributed bias variable and a time-dependent multiplier with various time profiles.

Zupanski (1993) applied a similar bias term with a parabolic time-dependent multiplier to an operational primitive-equation forecast model and concluded that the additional bias correction term resulted in significant improvement over the standard adjoint approach. The same bias-term method was also successfully used by Lee and Lee (2003) for the assimilation of retrieved satellite data. More complicated forms of model error have also been assumed within 4DVAR systems. Zupanski (1997) prescribed model error as a first-order Markov variable with the random component defined on a much coarser time scale (on the order of hours) than the model time step and pointed out the necessity for a weak constraint in order to obtain the full benefits of the 4DVAR method. D'Andrea and Vautard (2000) decomposed model error into time-constant, state-dependent, and stochastic parts where the state-independent part was parameterized through the construction of a transfer function that is obtained from analogue states. They concluded that flow-dependent model error contributed significantly to the reduction of systematic error. Bias correction approach was also adopted within sequential (Kalman) filtering framework by Dee and Da Silva (1998) through the use of a two-stage algorithm that consisted of a "bias-blind" state estimator and a bias estimator where a persistence model was assumed for the time evolution of bias.

A somewhat different means of approaching model error has been introduced by Zou et al. (1992), who used a 4DVAR scheme to estimate the parameters of an optimal nudging data assimilation scheme. This idea of estimating parameters for data assimilation was also employed by Dee (1995) who used a maximum-likelihood method to tune the parameters of the innovation covariance and then used the adjusted

innovation covariance to improve the performance of a simplified Kalman filter for a linearized two-dimensional shallow water model with stochastic forcing. In a later and more comprehensive study, this method was further developed (Dee and da Silva 1999; Dee et al. 1999) and not only issues such as parameter identifiability, estimation accuracy, and robustness of the method were addressed but the method was also applied to a wider variety of cases and with a more complex general circulation model. Mitchell and Houtekamer (2000) developed a method of accounting for model error in an ensemble Kalman filter context by adding an ensemble of realizations of model error to the ensemble of model predictions by a three-level quasigeostrophic model. Following Dee (1995), the method involved parameterizing the model error and using innovations to estimate the model-error parameters. Mitchell et al. (2002) extended the same method to a primitive-equation context where the model-error statistics were assumed to be known, eliminating the need to adaptively estimate the model error.

When uncertainties in model parameters are assumed to be a major source of model error, data assimilation schemes can also be utilized to estimate these uncertain model parameters. In the field of atmospheric sciences, studies that involve direct estimation of model parameters have been mostly limited to the application of variational techniques. Navon (1998) provides a detailed review of meteorological and oceanographic literature on parameter estimation through variational methods. One of the earliest applications of direct parameter estimation using contemporary techniques was by Rinne and Järvinen (1993) who, through the use of the adjoint of their model, attempted to estimate the Cressman term of a barotropic model, which is used to

parameterize the divergence associated with long waves. Gong et al. (1998) used a "toy" linear model of an equivalent barotropic vorticity equation for the streamfunction on a latitude circle and its adjoint to attempt adaptive on-line tuning of multiple weighting, smoothing, and physical parameters. They concluded that physical parameters to which the analysis is sensitive can be tuned along with one or two weighting parameters (a parameter that controls the trade-off between fits to the data and forecast and a parameter that controls the relative strength of the weakness of the constraint) and a smoothing parameter. In another application of simultaneous optimization of parameters and initial conditions with a 4DVAR scheme, Zhu and Navon (1999) employed a much more complex global spectral model and its adjoint where the estimated parameters were the biharmonic horizontal diffusion coefficient, the ratio of the transfer coefficient of moisture to the transfer coefficient of sensible heat, and the Asselin filter coefficient. An interesting conclusion was that, although the impact of optimal initial conditions dominated that of the optimal parameters at early stages of forecasts, the model tended to lose first the impact of the initial conditions while the impact of optimal parameters persisted beyond 72 hours. Nevertheless, it is, at this point, still an open question how the relative impacts of optimal initial conditions and optimal parameters would vary in a continuous data assimilation system with more frequent analysis cycles. Clearly, such an assessment would also depend on the underlying dynamics; in situations such as when diurnal forcing is strong, the relative impacts of optimal initial conditions and optimal parameters might also become a function of time.

The main approach of this doctoral study is to apply the ensemble Kalman filtering technique to a sea breeze setting. This is a novel application of the filter from several points of view. First of all, the ensemble Kalman filter has not been extensively applied to meso- and smaller scale atmospheric phenomena; and those applications that did attempt to do this have mainly focused on supercell modeling. In that respect, this study will be the first to apply ensemble Kalman filtering to a thermally-forced mesoscale circulation. Second, modeling of a thermally-driven sea breeze event imposes important challenges for the ensemble Kalman filtering technique that have not been previously addressed in the literature. For instance, surface-air interaction is very critical in sea breeze dynamics and it is usually a parameterized process in mesoscale models. Hypothetically, when such parameters are considered as part of the initial state vector, ensemble Kalman filtering could be utilized to estimate the values of such critical parameters, as well, which would potentially be a major improvement in terms of the performance of a numerical sea breeze model. In other words, the present study aims to address the model error problem by adopting the parameter estimation approach in an ensemble Kalman filter (EnKF) environment.

As noted earlier, in atmospheric sciences, treatment of model error, in general, and estimation of model parameters, almost exclusively, have been limited to variational data assimilation schemes. Anderson (2001) is the first study where the applicability of the ensemble-based data assimilation to the estimation of model parameters is briefly considered. In Anderson (2001), a demonstration of the idea is performed for the forcing parameter of the 40-parameter Lorenz model (Lorenz 1996) and it is concluded

that, "given the extreme difficulty of tuning sets of model parameters, an investigation of the possibility that this mechanism could be used seems to be of great importance". The current study provides a rigorous attempt to address this possibility and to establish the EnKF as a potential tool to treat parametric model error. In this regard, this study is the first known systematic analysis of the EnKF for the problem of parameter estimation for meteorological applications.

1. Theoretical Background

a. Data Assimilation

Imperfection in a forecast has four possible sources: imperfect theoretical knowledge of the physical processes underlying fluid motion, imperfect numerics of the model to resolve underlying mathematical equations, imperfect knowledge of the boundary conditions, and imperfect knowledge of the initial state. During the initial phase of NWP it was believed that our main limitation in NWP was the limited computing power which had resulted in the oversimplified representation of the dynamical equations in the numerical schemes. Therefore, effort had mostly focused on ways to improve predictability by improving the resolution and numerical schemes of the models [see, for instance, Charney et al. (1966)]. An alternative approach toward NWP was initiated by Thompson (1957) who recognized the importance of the uncertain initial state as a factor in determining the predictability of a system. Yet it would be Edward Lorenz who established the science of the chaotic nature of dynamical systems. Through his pioneering work [see, for instance, Lorenz (1963), Lorenz (1969a) and Lorenz (1969b)] meteorologists today appreciate that the atmosphere is sensitively

dependent upon initial conditions and that it possesses an intrinsic limit to its predictability.

Estimation of the initial state has become one of the key elements of NWP. In the context of numerical modeling, the phrase *data assimilation* refers to the cumulative effort of initial-state estimation. Broadly speaking, it involves combining all available information to yield a better prediction. Available information consists first of observations. The observations vary significantly in accuracy and nature, and have a highly irregular temporal and spatial distribution. Most importantly, they can be direct, which means that they bear on the same physical quantities to be used in the description of the flow, or they can be indirect, so that they bear on quantities that are related to the physical quantities of the flow through possibly complicated functions. The second source of information consists of the physical laws of fluid motion. It should be noted that incomplete theoretical knowledge of the fluid motion on many different scales, simplification of the mathematical forms of equations when transforming them into numerical form, choice of numerical methods to solve these equations, and truncations both in time and space all contribute to the errors associated with numerical models. In a data assimilation context, the estimate of the current state by a numerical model and its error structure are coined “background information” and “background error covariance matrix”, respectively.

From an algorithmic point of view, data assimilation can take two forms, sequential assimilation and variational assimilation. In sequential data assimilation, whenever the model time reaches an instant at which observations are available, the

predicted background state is updated with the new observations serially. On the other hand, in variational data assimilation, model solution is adjusted globally to all available observations by minimizing an objective function that measures the distance between the background and available information. Being purely a minimization problem, variational methods do not require any statistical assumptions about the state vector or observations. While sequential forms are easier to integrate into the overall flow of the prediction process and are computationally less costly, variational forms have the advantage of propagating available information both forward and backward in time [see, for instance, Ghil (1989), Talagrand (1997), and Sneddon (2000) for detailed overviews of the two forms].

The basic idea behind all of the estimation schemes is that it is possible to achieve, by the combination of independent sources of information, a state with improved error statistics. All sources of information are assumed to be composed of deterministic and stochastic ingredients, which require one to describe the combination process in a probabilistic manner. To be more specific, consider the simplest possible case where two independent scalar "measurements" x and y, with variances σ_x^2 and σ_y^2, respectively, are available in order to estimate the atmospheric quantity $\overline{x}$ (for instance, one can imagine that x is a model output and y is an independent instrument observation). Assuming that $\overline{x}$ can be expressed as a linear combination of x and y, one can define the estimation relationship in the following manner (Ghil 1989):

$$\overline{x} = \alpha_x x + \alpha_y y \,. \tag{1}$$

Assuming, in addition, that measurements (x and y) and estimates ($\bar{x}$) are unbiased, means that their expected values are equal ($E\{x\} = E\{y\} = E\{\bar{x}\}$) which automatically leads to

$$\alpha_x + \alpha_y = 1. \tag{2}$$

We can therefore write

$$\bar{x} = x + \alpha_y (y - x). \tag{3}$$

The optimal linear unbiased estimate of $\bar{x}$ can be calculated by choosing α_y so as to minimize the variance of the estimate, $\bar{\sigma}^2$. By elementary algebra it can be shown that the pair of α_x and α_y that minimizes $\bar{\sigma}$ is

$$\alpha_x = \bar{\sigma}^2 / \sigma_x^2 , \tag{4}$$

$$\alpha_y = \bar{\sigma}^2 / \sigma_y^2 , \tag{5}$$

where

$$\bar{\sigma}^{-2} = \sigma_x^{-2} + \sigma_y^{-2} . \tag{6}$$

By inspection we can qualitatively see that the variance of the estimate is smaller than variances of the measurements. Should any one of the measurements be missing or their variance be unreasonably large, the estimate will favor the other measurement. This very basic idea lies beneath all of the assimilation procedures. It is also interesting to note that, without actually making any statistical assumptions, one can still reach the same result by a variational method which would minimize the cost function

$$J \equiv \beta_x (\bar{x} - x)^2 + \beta_y (\bar{x} - y)^2 , \tag{7}$$

provided that $\beta_x = \alpha_x^2$ and $\beta_y = \alpha_y^2$ (Ghil 1989).

The approaches described by equations (1) - (6) and the equation (7) form the fundamental concepts of data assimilation. While equations (3) - (6) lend themselves easily applicable in a sequential assimilation setting, equation (7) makes it possible to define a constrained minimization function and solve it numerically to achieve the estimate.

b. The Kalman Filter

Although widely used in many different assimilation schemes with great success, variational methods have been criticized because of their inability to account for the evolution of background error. A relatively new approach, at least in atmospheric sciences, the *Kalman filter* (KF), addresses this problem and provides an alternative approach that constructs both the best linear unbiased estimate and the updated background error covariance matrix. First developed in an engineering context (Kalman 1960), applied systematically to meteorological problems by Ghil et al. (1981), and investigated for effectiveness in the presence of instabilities in a simple one-dimensional barotropic vorticity equation by Miller (1986), the KF has been widely applied in various modeling settings and has been gradually refined to become suitable for applications that would otherwise require vast amounts of computational power. Its main idea is actually very straightforward: Since we have a limited and imperfect set of observations, the true state of a system, $\mathbf{x}^t$, cannot be determined precisely. In other words, it would be more meaningful to treat $\mathbf{x}^t$ as a random variable and attempt to estimate its probability density function, instead. Naturally, given the limited number of

observations, $\mathbf{y}^0$, we could only extract the conditional probability distribution for $\mathbf{x}^t$ given observations, $p(\mathbf{x}^t \mid \mathbf{y}^0)$. Based on very basic statistical assumptions, the KF provides the exact formulae for calculating this conditional probability distribution.

The assumed stochastic forms of the forecast (background) estimate ($\mathbf{x}^f$) and the observation vector ($\mathbf{y}$) are, respectively:

$$\begin{aligned} \mathbf{x}^f &= \mathbf{x}^t + \boldsymbol{\varsigma}^f , \\ \mathbf{y} &= \mathbf{H}\mathbf{x}^t + \boldsymbol{\varepsilon} . \end{aligned} \tag{8}$$

Here, $\mathbf{H}$ is a linear transformation matrix that maps the model space into the observational space, while ς^f and $\boldsymbol{\varepsilon}$ are the errors of the forecast estimate and the observations, respectively. For the context of the KF, both the forecast estimate errors and the observational errors are assumed to be uncorrelated and of white noise type, i.e. they have a Gaussian distribution of the form $N(0,\mathbf{P}^f)$ and $N(0,\mathbf{R})$, where $\mathbf{P}^f = E\left\{\boldsymbol{\varsigma}^f \cdot \boldsymbol{\varsigma}^{f\mathrm{T}}\right\}$ and $\mathbf{R} = E\left\{\boldsymbol{\varepsilon} \cdot \boldsymbol{\varepsilon}^{\mathrm{T}}\right\}$ are the forecast and observation error covariance matrices, respectively. With these definitions and basic assumptions, the Kalman gain matrix is defined as:

$$\mathbf{K} \equiv \mathbf{P}^f \mathbf{H}^{\mathrm{T}} \left(\mathbf{H}\mathbf{P}^f \mathbf{H}^{\mathrm{T}} + \mathbf{R}\right)^{-1} . \tag{9}$$

The Kalman filter updates $\mathbf{x}^f$ and $\mathbf{P}^f$ with the observations through

$$\begin{aligned} \mathbf{x}^a &= \mathbf{x}^f + \mathbf{K}\left(\mathbf{y}^0 - \mathbf{H}\mathbf{x}^f\right), \\ \mathbf{P}^a &= \left(\mathbf{I} - \mathbf{K}\mathbf{H}\right)\mathbf{P}^f \left(\mathbf{I} - \mathbf{K}\mathbf{H}\right)^{\mathrm{T}} + \mathbf{K}\mathbf{R}\mathbf{K}^{\mathrm{T}} \\ &= \left(\mathbf{I} - \mathbf{K}\mathbf{H}\right)\mathbf{P}^f , \end{aligned} \tag{10}$$

where subscript "a" denotes updated or "analysis" values of the state vector and its covariance.

In order to put equations (8) - (10) to practical use, the final step that connects the solutions to the sequential assimilation process needs to be explained. In order to take the temporal progression of the problem into account, the true state of the system is assumed to evolve according to the following linear equation:

$$\mathbf{x}_{k+1}^{t} = \mathbf{M}\mathbf{x}_{k}^{t} + \boldsymbol{\eta}_{k} \tag{11}$$

where the subscript k stands for the current time step of the numerical model, while $\mathbf{M}$ is the transition matrix that corresponds to the dynamics of the model, and $\boldsymbol{\eta}_k$ is the model error, again of white noise type in time and with covariance matrix $\mathbf{Q}$ [has a Gaussian distribution of $N(0,\mathbf{Q})$ form].

If we now assume that the estimate of the true state $\mathbf{x}_k^t$ is available, in the form of $\mathbf{x}_k^a$, then the forecast estimate for the next time step will be:

$$\mathbf{x}_{k+1}^{f} = \mathbf{M}\mathbf{x}_{k}^{a} . \tag{12}$$

Additionally, the covariance matrix of the corresponding estimation error will be (Talagrand 1997):

$$\mathbf{P}_{k+1}^{f} = \mathbf{M}\mathbf{P}_{k}^{a}\mathbf{M}^{\mathrm{T}} + \mathbf{Q} . \tag{13}$$

At this step, the new observation vector $\mathbf{y}_{k+1}^{0}$ can be introduced so that the updated analysis vector $\mathbf{x}_{k+1}^{a}$ and the corresponding updated covariance matrix $\mathbf{P}_{k+1}^{a}$ can be computed with the equations (10).

This sequential process defined by the equations (9) and (11) - (13) is known as Kalman filtering (Kalman 1960). At any given time, the KF produces the best linear unbiased estimate of the state of a system, using all observations available at the time and the prior model output.

There are certain clear advantages of using the KF. First of all, its recursive nature is very intuitive and makes it relatively easy to apply numerically. Another very important advantage is the fact that the KF also produces the updated covariance matrix at every time step which is of enormous potential value to meteorologists. On the other hand, the application of the KF has some numerical complications that need to be resolved usually by simplifying assumptions and numerical estimations. One such very important problem is the fact that the calculation of $\mathbf{P}_{k+1}^{f}$ involves the computation of $\mathbf{M}\mathbf{P}_{k}^{a}\mathbf{M}^{\mathrm{T}}$. Since the dimension of the transition matrix $\mathbf{M}$ is equal to the dimension of the state vectors $\mathbf{x}^{a}$ and $\mathbf{x}^{f}$, for meteorological applications, its value is usually on the order of $10^{6} - 10^{7}$. This means that, in order to compute the value of $\mathbf{P}_{k+1}^{f}$ directly, two successive matrix multiplications by $\mathbf{M}$ are required, which is beyond the computational resources available today (Talagrand 1997).

c. The Ensemble Kalman Filter

As explained in the previous section, the calculation of the background error covariance matrix, $\mathbf{P}_{k+1}^{f}$, imposes numerical problems on the Kalman filtering approach. One very robust technique to address this problem, first proposed for geophysical applications by Evensen (1994), is the ensemble Kalman filter (EnKF). While an

ensemble, in this context, can be defined as a collection of model states that are obtained by perturbing the initial analysis in a way consistent with the analysis uncertainty [see Sivillo et al. (1997) for a historical background on ensemble forecasting], the EnKF is a version of the KF that uses an ensemble of model forecasts to directly estimate the background error covariance structure. The KF equations are modified to reflect the update of the ensemble mean, while the time integration of the covariance matrix is performed implicitly through the time integration of individual ensemble members:

$$\begin{aligned} \overline{\mathbf{x}}^{a} &= \overline{\mathbf{x}}^{f} + \mathbf{K}\left(\mathbf{y}^{0} - \mathbf{H}\overline{\mathbf{x}}^{f}\right), \\ \mathbf{K} &= \mathbf{P}^{f}\mathbf{H}^{\mathrm{T}}\left(\mathbf{H}\mathbf{P}^{f}\mathbf{H}^{\mathrm{T}} + \mathbf{R}\right)^{-1}. \end{aligned} \tag{14}$$

Here, $\overline{\mathbf{x}}^{f}$ and $\mathbf{P}^{f}$ represent the forecast (background) mean state and covariance matrix (sampled directly from the ensemble perturbations), respectively, while $\overline{\mathbf{x}}^{a}$ represents the updated analysis mean state. Observations are represented by the observation vector $\mathbf{y}^{0}$ and observational error matrix $\mathbf{R}$. The mapping between model space and observational space is accomplished through the matrix $\mathbf{H}$. In this form, $\mathbf{H}$ represents the first-order linear approximation to a possibly nonlinear observation function $\mathcal{H}$. The matrix $\mathbf{K}$ is known as the Kalman gain matrix and contains the coefficients of the linear combination of forecast state vector and observations.

The use of the ensemble technique in the Kalman filtering context has a relatively brief history that mostly focused on the theoretical aspects of the problem. The "adventure" began with Evensen (1994) who reported that the technique gave satisfactory results for a two-layer nonlinear quasigeostrophic model and an ensemble

size of the order of 100 members. In a further study, Evensen and van Leeuwen (1996) used a 500-member ensemble to assimilate gridded Geosat altimeter data into a similar model with higher resolution. Evensen (1997) also tested the technique, along with two weak-constraint variational methods (the "gradient descent" and the "ensemble smoother" methods), in a highly nonlinear setting and concluded that the ensemble Kalman filter adequately tracked the reference solution and that it could be a more practical method for larger primitive-equation models as it required smaller storage.

Preliminary evaluations of the EnKF since its introduction by Evensen (1994) for atmospheric applications have mainly focused on several theoretical and technical issues associated with the method (e.g. ensemble size, random variable form of observations, localization of observations – application of a radius of influence, inbreeding of the gain, and forecast-observation correlations) and have applied perfect-model assumptions to global-scale problems that mainly resolved large-scale instabilities [see Burgers et al. (1998), Houtekamer and Mitchell (1998), and van Leeuwen (1999) for detailed discussions on these subjects]. Further steps toward the operational application of the filter involved dropping the perfect-model assumption (Mitchell and Houtekamer 2000; Keppenne 2000); comparison of the EnKF to a 3DVAR scheme (Hamill and Snyder 2000); testing of the filter with an actual operational model (Mitchell et al. 2002, with Canadian Meteorological Centre's operational global model); and improving algorithm efficiency (Houtekamer and Mitchell 2001). Today, meteorological applications of the EnKF to large-scale flows have nearly reached the point of operational testing (Mitchell et al. 2002; Houtekamer et al. 2004), while assessments have also been performed for

massively-parallel ocean circulation models (Keppenne and Rienecker 2002). Although the results from the above-mentioned studies are very encouraging and almost complete at global and synoptic scales, there is much progress to be made before the EnKF is established as a viable assimilation technique for numerical modeling of meteorological phenomena at smaller scales, where applications of the filter have been much more limited due to the implementation challenges introduced by fully three-dimensional flow characteristics, highly nonlinear microphysical processes, and much more complicated boundary condition issues. At regional and mesoscales, Zhang et al. (2005) have shown for an explosive winter storm case that the EnKF is very effective in keeping the analysis close to the truth simulation while also showing that the most effective error reduction occurred at larger scales compared to the smaller, marginally resolvable scales where reduction in error was less effective. Only in recent years have there been attempts to assimilate Doppler radar observations into cloud-scale supercell models, albeit with partial success, first through simulated observations (Snyder and Zhang 2003; Zhang et al., 2004), and then subsequently using real observations (Dowell et al. 2004). The EnKF certainly needs further testing with more realistic model settings. In addition, the tests did not include time spans long enough and domains large enough to account for larger-scale processes that would possess different balance properties compared to convective scales. These additional complications may impose challenges for the EnKF.

Sequential processing of observations leads to considerable simplification of the analysis scheme and is therefore an attractive alternative to assimilating the entire observation vector at once (e.g., Whitaker and Hamill 2002; Snyder and Zhang 2003).

This is possible only if observation errors are assumed to be independent so that the order in which observations are processed does not influence the final estimate of the state (as long as the analysis error covariance, $\mathbf{P}^a$, is updated at each step). For a single, scalar observation y^0, the term $\mathbf{P}^f\mathbf{H}^{\mathrm{T}}$ of equation (14) becomes a column vector $\mathbf{c}$ of dimension of the state, while the term $\mathbf{H}\mathbf{P}^f\mathbf{H}^{\mathrm{T}}+\mathbf{R}$ becomes a scalar d. Similarly, the updating of the ensemble mean is performed by replacing the Kalman gain $\mathbf{K}$ by its simpler form as follows:

$$\overline{\mathbf{x}}^a = \overline{\mathbf{x}}^f + \mathbf{c}\left(y^0 - \mathbf{H}\overline{\mathbf{x}}^f\right)/d\,. \tag{15}$$

In addition to updating the ensemble mean, the covariance matrix also needs to be updated, which is achieved through updating the difference of each ensemble member from the mean. Following the ensemble square-root filter (EnSRF) formulation proposed by Whitaker and Hamill (2002), the update for the difference of each ensemble member from the mean (perturbations) is calculated by

$$\mathbf{x}^a - \overline{\mathbf{x}}^a = \left[\mathbf{I} - \beta(\hat{\mathbf{c}}/\hat{d})\mathbf{H}\right](\mathbf{x}^f - \overline{\mathbf{x}}^f)\,, \tag{16}$$

where $\beta = \left[1+(r/\hat{d})^{1/2}\right]^{-1}$, $\hat{\mathbf{c}}$ and $\hat{d}$ are sample estimates of $\mathbf{c}$ and d, and r is a scalar representing the observational error at the respective observation location. The analysis step defined in this manner is an alternative to perturbing observations in the analysis step of the EnKF (Burgers et al. 1998; van Leeuwen 1999). The idea behind this formulation is basically to derive an expression for the Kalman gain (which is called the "reduced" Kalman gain) that would yield the correct $\mathbf{P}^a$ in equation (10) (bottom part of $\mathbf{P}^a$ equation) when substituted into the top equation for $\mathbf{P}^a$ in equation (10) without the

term $\mathbf{KRK}^{\mathrm{T}}$ (because non-perturbed observations are not correlated). Since perturbing observations introduces noise that unavoidably becomes correlated with the background error for small ensemble sizes (due to insufficient sampling), the EnSRF is claimed to be a superior technique that both avoids the systematic variance underestimation problem with the EnKF and circumvents the issue of observation-background error correlation [see also van Leeuwen (1999) for a detailed discussion of this issue]. Once the analysis ensemble is determined by repeating the analysis step for all of the available observations, the forecast step simply evolves each member forward to the next time step of available observations.

In passing it is noted that the use of the acronym "EnKF", in its strictest sense, refers to the "standard" perturbed-observations formulation of the filter. However, because of the fact that the goal here is not to draw the attention to any differences between perturbed-observation and deterministic filters but merely to use the EnSRF due to practical and theoretical advantages, it is decided to use the acronym "EnKF" throughout the work to represent the broader class of ensemble-based Kalman filters.

Another modification that is commonly employed within recent EnKF applications pertains to the rank deficiency problem associated with undersampling when using small ensembles. Houtekamer and Mitchell (1998) noted that the EnKF analysis could be improved by preventing distant observations from influencing the update of a grid point. They argued that this was mainly due to the fact that small-sized ensembles tended to overestimate covariances between greatly separated grid points and, as a remedy, applied a cutoff radius beyond which covariances were not calculated.

Commonly known as covariance localization, Houtekamer and Mitchell (2001) have since experimented with a more sophisticated Schur product approach where the ensemble-based covariance estimates are multiplied element by element with a distance-dependent correlation function that varies from 1.0 at the observation location to 0.0 at some predefined cutoff distance (a widely used such correlation function is Gaspari and Cohn's (1999) compactly supported fifth-order function). Houtekamer and Mitchell (2001) maintain that "the effect of localization is to increase the effective size of the ensemble". For this study, Gaspari and Cohn's (1999) compactly supported fifth-order function is employed as a means to localize the covariance structure with no posterior covariance inflation applied.

d. Parameter Estimation

Without a doubt, engineers are the foremost investigators to have developed and matured contemporary research on parameter estimation. In fact, parameter estimation still remains one of the primary areas of study for engineering disciplines such as control theory, signal theory, telecommunications, robotics, and aeronautics. In these disciplines, the terms *parameter identification*, *system identification*, and *adaptive control* are frequently used interchangeably along with the term *parameter estimation*. In contrast to engineering applications, parameter estimation for numerical weather prediction purposes can be considered as a relatively new and evolving research area that has found its most extensive applications in parallel to the advent of modern data assimilation techniques. Here, further focus is directed toward how parameter estimation has been developed in engineering disciplines.

Perhaps the most significant contribution to practical parameter estimation was from Kalman (1960) who developed a recursive formulation of the solution to linear optimal estimation problems hence making it possible to apply it to numerical computations in a cheap and relatively simple manner. Some examples of the early works that have considered a Kalman-type filtering approach for the problem of state estimation with unknown parameters are Ho and Whalen (1963), Cox (1964), and Mayne (1966). On the other hand, while Kalman filtering had become the most popular area of research for parameter estimation, it was not the only approach considered by researchers. Other techniques such as stochastic approximation, maximum likelihood, and correlations were being proposed and tested, as well (Mehra 1971). Due to the large number of early papers written on these techniques and the more limited scope of the current article toward the Kalman filter, these other techniques are not investigated in as much detail here and the reader is instead referred to a review article by Åström and Eykhoff (1971) for a starting point.

A very important issue associated with parameter estimation is that, in the presence of unknown parameters, the general state estimation problem, even with linear system dynamics, becomes a nonlinear one. Gelb (1986) briefly discusses the nonlinear nature of parameter estimation by first demonstrating it for constant parameters. Constant parameters in a system can be thought of a set of random variables, $\boldsymbol{\theta}$, satisfying $d\boldsymbol{\theta}/dt = 0$. If the parameters to be estimated and the state vector $\mathbf{x}$ (of dimension m) are combined into a composite state vector $\mathbf{x}_\theta$, the combined equations of evolution for the system become

$$\frac{d\mathbf{x}_{\theta}(t)}{dt} = \begin{bmatrix} d\boldsymbol{\theta}(t)/dt \\ ----- \\ d\mathbf{x}(t)/dt \end{bmatrix} = \begin{bmatrix} \mathbf{0} \\ ----- \\ \mathbf{M}(\boldsymbol{\theta})\,\mathbf{x}(t) \end{bmatrix}, \tag{17}$$

where **M** is the $m \times m$ dynamics matrix and system noise is omitted for simplicity. The concatenation of unknown parameters and the state variable into one vector is often referred to as *state augmentation*. In this form, it is evident that the augmented estimation problem becomes nonlinear because the product $\mathbf{M}(\boldsymbol{\theta})\mathbf{x}(t)$ is a nonlinear function of $\boldsymbol{\theta}$ and $\mathbf{x}(t)$. Furthermore, the augmentation of the state vector leads to the following adjustment to the observation equation:

$$\mathbf{y}^0 = \left[\begin{array}{c|c} \mathbf{0} & \mathbf{H} \end{array}\right] \cdot \begin{bmatrix} \boldsymbol{\theta}(t) \\ --- \\ \mathbf{x}(t) \end{bmatrix} + \boldsymbol{\varepsilon}, \tag{18}$$

Where $\mathbf{y}^0$ is the observation vector of dimension n_0, **H** is a $n_0 \times m$ matrix that maps state variables onto observations, and $\boldsymbol{\varepsilon}$ represents observational error.

Given the nonlinear nature of the augmented state estimation problem, it is evident that the classical Kalman filter will only provide a suboptimal solution for it. The entire procedure also becomes more computationally expensive because of the required additional treatment of nonlinearity. As a result of such considerations, early engineering research on parameter estimation focused on developing techniques to maximize the optimality of the proposed method in the most efficient manner. One common modification to the standard Kalman filter that addresses the nonlinearity of a given system is known as the extended Kalman filter (EKF) where the tangent-linear version of the nonlinear model is used (Gelb 1986). For a brief discussion on the early

issues related to the nonlinearity of parameter estimation and shortcomings of the EKF, the reader is referred to Nelson and Stear (1976). A more systematic analysis of the divergence and bias issues associated with the EKF for parameter estimation purposes can be found in Ljung (1979) who suggests that while bias originates from incorrect noise assumptions associated with the model, divergence is a more direct result of the algorithm because it lacks coupling between the Kalman gain **K** and the parameter vector **θ**.

Another central issue concerning parameter estimation is the concept of *identifiability* of parameters which is related to the requirement that the cost function must have a global minimum (Dee and da Silva 1998). According to Niu and Fisher (1997), non-identifiability of model parameters results from the singularity of the information or covariance matrix which is usually a consequence of one of three conditions: (1) Input signals are autocorrelated, which is sometimes also known as non-persistent input excitation. Frequently observed when a process runs in near steady state, this condition leads to input variables that can be represented by a combination of their past values and hence no longer are informative enough to identify all of model parameters. (2) Due to lack of knowledge about the processes that are modeled, an overparameterization can emerge which would make the covariance matrix vulnerable to singularity. (3) Output feedback causes the input to be correlated with past output variables. Even though the first and the third conditions are more of an issue for applications to systems control, it is clear from these conditions that identifiability of parameters is dependent on both available data and the characteristics of the model.

Emery et al. (2002) provide a good analysis of how observations can influence the information content for identifiability. They emphasize that error autocorrelation, which is usually a result of data sampled at uniform intervals, with relatively high rates of sampling or linearization, is a major source of information loss and necessitates a careful choice of model definition, including boundary conditions, as such choices will inevitably influence parameter sensitivities and hence their identifiability. Another concise but useful discussion on parameter identifiability can be found in Dee and da Silva (1998) who maintain that a proof for identifiability for a given estimation problem is in general not possible, although there are numerical techniques to check for identifiability problems which are related to the evaluation of the Hessian of the cost function at its minimum.

In more recent years, research has increasingly concentrated on the applications of parameter estimation to specific engineering/science problems while a considerable effort has also been put forward for the development of new techniques not only as modifications to the traditional EKF but also as alternatives with different theoretical approaches. Several of these techniques are today accepted as equally mature and robust. The reader is referred to the following brief list of recent articles and their references for a review and/or comparison of these new techniques as a basis for further study or investigation: Beck and Woodbury (1998) review and compare some of the *inverse techniques* (variational methods) as applied to parameter estimation; Glielmo et al. (1999) compare the traditional EKF and two modified versions of it with their own interlaced EKF; Ananthasayanam (2000) reviews some of the estimation techniques in a

broader style from an aerospace engineering perspective; Bohn and Unbehauen (2001) perform a gradient-based sensitivity analysis of the EKF and three other filters; Liu and West (2001) provide an overview of particle filtering techniques as they are applied to combined state and parameter estimation; Timmer (2000) discusses the applicability of three estimation techniques to parameter estimation of stochastic differential equations; and Singer (2002) provides a technical discussion and comparison of the EKF and some other methods in the context of parameter estimation of nonlinear stochastic differential equations.

e. The Land and Sea Breeze

The sea breeze is perhaps one of the most extensively studied phenomena in atmospheric dynamics. Walsh (1974), Anthes (1978), and Rotunno (1983) provide a good review and a comprehensive list of references on the theoretical aspects of the phenomenon, and Wakimoto and Atkins (1994) and Atkins et al. (1995) give excellent reviews on the observational characteristics of the sea breeze. Simpson (1994) also provides an excellent "primer" mostly on the observational features and some theoretical aspects of the sea breeze and other local wind phenomena.

Although linear theory has been used to explain some of the interesting features of the sea breeze with success, its limitations, especially its lack of variability of vertical stratification and diffusivity, lead to symmetric land- and sea-breeze circulations and the strongly nonlinear sea-breeze front could not be modeled (Simpson 1994). Due to these crucial limitations, the linear model should only be treated as a general framework for the land/sea breeze phenomenon while the description of the detailed local structure

(which is mostly governed by the nonlinear features like the sea-breeze front) can be carried out more effectively by the help of numerical models.

Because of its strong sensitivity to small-scale variations and because of its highly nonlinear nature, accurate sea-breeze modeling has proven to be a very challenging task. Among the major difficulties that are involved, successful integration of parameterization schemes with the dynamic model turns out to be the most critical aspect of the sea-breeze modeling. Some of the factors which affect the land and sea breeze circulation are diurnal variation of the ground temperature, diffusion of heat, spatial and diurnal variation of static stability, and diffusion of momentum (Simpson 1994). Clearly, while these are variables/processes that are usually treated within the context of parameterization schemes, they are rarely observed at the spatial and temporal resolutions pertinent to land/sea breeze circulation. Both of these facts (the importance of parameterization schemes in the context of sea-breeze modeling, and the lack/insufficiency of observations critical for the parameterization schemes involved) contribute to the complexity of the problem and warrant the integration of a well-designed parameter identification scheme into the numerical model.

Another important motivation behind the application of the EnKF to a sea breeze environment pertains to the fact that all of the synoptic and mesoscale phenomena that have been put under the scrutiny of EnKF research to date can be regarded as a special class of flows exhibiting free dynamics; i.e., they do not proceed under the dominant influence of an external forcing. There is thus a wide range of dynamical systems, commonly known as chaotic forced-dissipative systems, that range from the sea breeze

circulation at the smaller-scale end of the spectrum to the climate at very large scales, that have not yet been subjected to assimilation experiments with the EnKF.

There are two possible lines of reasoning to suggest that chaotic forced-dissipative systems may exhibit a sufficiently dispersive nature to warrant the application of data assimilation. The first is of an empirical nature: daily experience with local phenomena such as the sea breeze or the mountain breeze circulations suggests that the timing, strength, and penetration properties of the nonlinear frontal structures, as exhibited through cloud formation, convective activity, changes in air quality, and/or strong wind shifts, can differ significantly from day to day even under seemingly similar synoptic conditions (Simpson 1994; Miller et al. 2003). The second argument is based on theoretical evidence related to the chaotic nature of nonlinear, forced-dissipative systems. At the large-scale end of atmospheric motions with time scales on the order of months to millennia, it has been shown that, even for severely truncated models, multiple stationary solutions exist with varying stability, and transitions between such solutions occur as a result of changes in the forcing parameters. There is in fact a plethora of published material on this topic; for an introductory discussion see, for instance, Charney and DeVore (1979), Vickroy and Dutton (1979), and Mitchell and Dutton (1981). At the smaller scales, a similar behavior has been recently demonstrated for the sea and land breeze by Feliks (2004) with a two-dimensional model. Moreover, due to the strong dependence of the chaotic nature of forced-dissipative systems on the forcing, one might also conjecture that the

predictability of such systems should be closely linked to the parameter space that controls the forcing and the system's response to forcing.

2. Objectives and Goals

The objectives of this study can be summarized in two main groups. The first and main objective is to apply the ensemble Kalman filtering technique to a sea breeze event in a perfect-model setting. Specific goals at this stage are:

(i) Set up an ensemble initiation mechanism in order to produce an ensemble with realistic background covariance structure.

(ii) Obtain a satisfactory filter setting that performs well under the "perfect model" assumption.

(iii) Simulate observations with different distribution scenarios (regularly distributed observations, regularly distributed observations with different characteristics on land and sea, randomly distributed observations with realistic spacing, and observations at actual real-world locations) in order to test the sensitivity of the filter on observation locations and frequency.

(iv) Examine the effects of several filter parameters on filter performance under different observation scenarios.

The second objective of this study is to employ the ensemble Kalman filter settings obtained from the first objective for the estimation of some of the model parameters (parameter identification). Specific goals pertaining to this objective can be listed as:

(i) Obtain a meaningful and simple parameter or set of parameters to estimate through sensitivity tests.

(ii) Establish realistic limits on the variability of these parameters based on the sensitivity tests.

(iii) Observe the effects of parameter estimation on model performance.

3. Structure and General Methodology

In this study, the application of the EnKF in the context of the problem of simultaneous state and parameter estimation has been performed for numerical models of the sea breeze environment of progressively increasing complexity. For lower complexity, the sea breeze is modeled as the nonlinear response to a specified oscillating interior heat source in two dimensions, as in the linear theory of Rotunno (1983). For this case, the EnKF is first applied to a perfect-model setting where model parameters are kept the same as the truth run and thus the filter performance is examined for the estimation of the model state only. As the following step, a set of model parameters are then perturbed about an incorrect (different than the truth) mean value in the ensemble and assimilation experiments are performed to retrieve both the state and imperfect parameters of the model.

As the final step, NCAR/PSU nonhydrostatic MM5 version 3 is chosen as the modeling environment of operational complexity. Similar to the two-dimensional sea breeze model, MM5 experiments are also based on the perfect model assumption and observations are simulated from a control run with the same model settings except slightly perturbed initial conditions and parameter set. Assimilation experiments are

then performed with the EnKF to estimate both the mean state and the imperfect parameters simultaneously.

All of the experiments in this study are based on the assumptions of a perfect forecast model, perfect uncertainty, and a perfect ensemble. In a *perfect model* scenario, there is assumed to be a model configuration with no model error, which enables the "truth" to be produced by the model. When the truth data is available, filter performance can be measured directly by comparing the analysis fields to the truth, facilitating a rigorous sensitivity analysis of the filter. Similarly, the p*erfect uncertainty* assumption also makes possible the testing of the numerical aspects of the EnKF, by presuming that the background error covariance matrix is available in its entirety for the initiation of the model. When this assumption is made, the EnKF is expected to produce the best linear unbiased estimate of the state vector at future times. In other words, the effect of imperfect model dynamics on error growth is eliminated. Finally, the *perfect ensemble* assumption indicates that the truth and the ensemble members are drawn from the same probability distribution. In other words, it is not possible to differentiate between the truth and the ensemble members statistically. To ensure perfect ensemble statistics, the truth is generated the same way as any other ensemble member. In practice, the ensemble contains one more member than the nominal ensemble size and the truth is randomly chosen as one of these members that contains a similar magnitude of initial error (in a root-mean-square sense compared to the ensemble mean) as the initial ensemble spread (in a standard deviation sense).

ESTIMATION EXPERIMENTS WITH THE TWO-DIMENSIONAL SEA BREEZE MODEL: STATE-ONLY ESTIMATION

1. The Sea Breeze Model and Filter Design

a. Model Numerics

As in the linear theory of Rotunno (1983), an idealized prototype problem is adopted in which the sea breeze circulation is modeled as the response to a specified oscillating heat source in the fluid interior. For simplicity, the flow is taken to be Boussinesq with only hydrostatic and non-rotating disturbances in two dimensions. The equations of motion can then be written in vorticity-streamfunction form as

$$\begin{aligned} &\frac{\partial \eta'}{\partial t} + (\overline{u} + u')\frac{\partial \eta'}{\partial x} + w'\frac{\partial \eta'}{\partial z} + \frac{\partial b'}{\partial x} = \kappa_\eta \frac{\partial^2 \eta'}{\partial z^2}, \\ &\frac{\partial b'}{\partial t} + (\overline{u} + u')\frac{\partial b'}{\partial x} + w'\frac{\partial b'}{\partial z} + N^2 w' = Q + \kappa_b \frac{\partial^2 b'}{\partial z^2}, \end{aligned} \tag{19}$$

where $\mathbf{u} = (u', w')$ is the disturbance fluid velocity, $\eta' = \frac{\partial u'}{\partial z}$ is the hydrostatic vorticity, and $b' = g\theta'/\theta_0$ is the Boussinesq buoyancy. Here g is the acceleration of gravity and $\theta = \theta_0 + \theta_B(z) + \theta'(x,z,t)$ is the potential temperature, where θ_0 and θ_B are reference and background potential temperatures, respectively, while $N^2 = (g/\theta_0)(\partial\theta_B/\partial z)$ is the square of the background Brunt-Väisälä frequency.

Dissipation in the model is represented through the vertical diffusion of vorticity and buoyancy, where κ_η and κ_b are the constant eddy diffusion coefficients for η and b,

respectively. Free-slip and thermal insulation conditions are applied at the lower boundary of the model domain by setting both η' and $\partial b' / \partial z$ to zero at $z = 0$.

Forcing takes the form of an explicit heating function Q defined by

$$Q = \left[A_0 \cos \omega t + \varsigma(t) \right] \left[\left(\frac{1}{2} + \frac{1}{\pi} \tan^{-1} \frac{x}{x_0} \right) e^{-z/z_0} \right]. \tag{20}$$

Here, A_0 is a constant heating amplitude; x_0 and z_0 are horizontal and vertical length scales of heating, respectively; ω is the diurnal frequency; and ζ is a stochastic white noise term. In this functional form, the initial time corresponds to a maximum heating phase.

Walter (2004) has shown through a scale analysis that, for weak background wind $\overline{u}$, the nonlinearity of the model is controlled by a non-dimensional amplitude parameter defined by $\varepsilon = A_0 \left(N^2 \omega z_0 \right)^{-1}$. His findings indicate that the system begins to demonstrate nonlinear effects (developing density currents) for $\varepsilon > 0.8$; for smaller values of ε, nonlinearity in the system remains weak. Following this reasoning, then, the heating amplitude A_0 becomes the controlling parameter of nonlinearity when the other parameters N^2, ω, and z_0 are kept constant. Moreover, it is important to note that in a viscous system nonlinearity will also be dependent on the strength of diffusion which is measured by the non-dimensional Reynolds number $\mathrm{Re} = \omega z_0^2 \kappa_\eta^{-1}$. Although there is no direct connection between the Reynolds number and the degree of nonlinearity in this formulation, one can in general argue that the smaller the Reynolds number becomes, the larger should be the critical value of ε where effects of nonlinearity begin to be observed.

In other words, all other parameters being equal, larger vertical diffusivity would require a larger heating amplitude to force the flow into the nonlinear regime.

The prognostic equations are integrated using leapfrog time differencing with a weak Asselin time filter (Asselin 1972) for all terms except the vertical diffusion. The diffusion terms are integrated using trapezoidal time differencing. All spatial derivatives are computed using second-ordered centered differences, and a weak horizontal filter is included to help stabilize the steep gradients that occur at the fronts. From a theoretical point of view, the leapfrog scheme with the Asselin filter may not be the optimal numerical integration technique for a stochastic dynamical system (see, for instance, Ewald et al. 2004; Penland 1996). However, the goal here is not to obtain the most accurate numerical solution to the analytic sea breeze equation (19). Rather, the truth and forecast integrations are consistently based on the sea breeze system defined through the numerics, time step, and noise handling.

The horizontal (cross-shore) and vertical dimensions of the forecast domain are 500 km and 3 km, respectively, with the coast located at the center (at $x = 0$) and the land located to the right of the coast. There are two Rayleigh-damping sponge layers to the left and right of the forecast domain, each of width 300 km, and another above the forecast domain with a 2-km depth. Grid spacing is 4 km horizontally and 50 m vertically, thus optimally resolving the mesoscale properties of the sea breeze circulation while marginally resolving the frontal structure.

b. Ensemble and Filter Characteristics

A "climatological" initialization scheme was utilized for this study. The key steps of this scheme are as follows: (1) Using the sea breeze model and an initial background state (zero perturbation vorticity and zero perturbation potential temperature throughout the domain), a 15-day hourly time series is produced. (2) To allow for the initial adjustment from the background state, only days 4 through 15 are used for choosing initial states of ensemble members. (3) Initial states are chosen randomly from the available time series with a normal probability distribution centered at the initial time of day (local noon or maximum heating phase for this application) of the ensemble runs. In other words, the maximum heating states within the 15-day time series have the highest probability to be selected into the ensemble and a standard deviation of 8 hours is used for the normal distribution around the central maximum heating state.

In most of the experiments, an ensemble size of 50 is used. In order to obtain a perfect ensemble, truth is taken as one of the ensemble members. Unless noted otherwise in the article, other properties of the filter chosen for this study are: radius of influence of 100 grid points (400 km horizontal and 5 km vertical), and simulated land surface buoyancy observations with error 10^{-3} ms^{-2} and spacing of 40 km.

2. Results

a. Model Behavior

To begin, a demonstration of the mean-state behavior of the sea breeze model will be presented for a moderately nonlinear regime. No EnKF analysis is performed during this run. Mean horizontal wind ($\overline{u}$) is set at a weak value of 0.5 ms^{-1} and the

Brunt-Väisälä frequency (N) is chosen to be 10^{-2} s^{-1}. For the heating profile, horizontal and vertical length scales (x_0 and z_0) are set at 10 km and 500 m, respectively. The vertical diffusion coefficients of buoyancy and vorticity (κ_b and κ_η) are both chosen to be 0.25 m^2s^{-1}, in order to have a Prandtl number $\Pr \equiv \kappa_\eta / \kappa_b = 1$. These settings correspond approximately to a Reynolds number on the order of 50-100 and indicate that the effects of vertical diffusion on nonlinearity should be relatively small. A mean value of 7×10^{-6} ms^{-3} is used for heating amplitude which roughly corresponds to a value of 1.9 for the nonlinearity parameter ε. With this ε, nonlinear features are expected to be locally significant near the coast while the overall nonlinearity is still expected to be moderate (Walter 2004). At higher heating amplitudes, the model becomes numerically unstable. Finally, the standard deviation of the stochastic heating amplitude is set at 4×10^{-6} ms^{-3}, resulting in an expected range of 0.8-3.0 for the nonlinearity parameter ε (although the actual influence of stochasticity on nonlinearity is smaller than the suggested range because of the effects of time filtering and diffusion).

Diagnosis of sea breeze and land breeze cycles

To demonstrate the model behavior, key stages of a 24-hour sea and land breeze cycle are presented in Figure 1. Panels from top to bottom indicate the time evolution of the corresponding sea/land breeze cycle, beginning with the 123-hour forecast time that corresponds to the onset of the sea breeze and continuing with 6-hourly intervals until the 141-hour forecast time that corresponds to the peak land breeze.

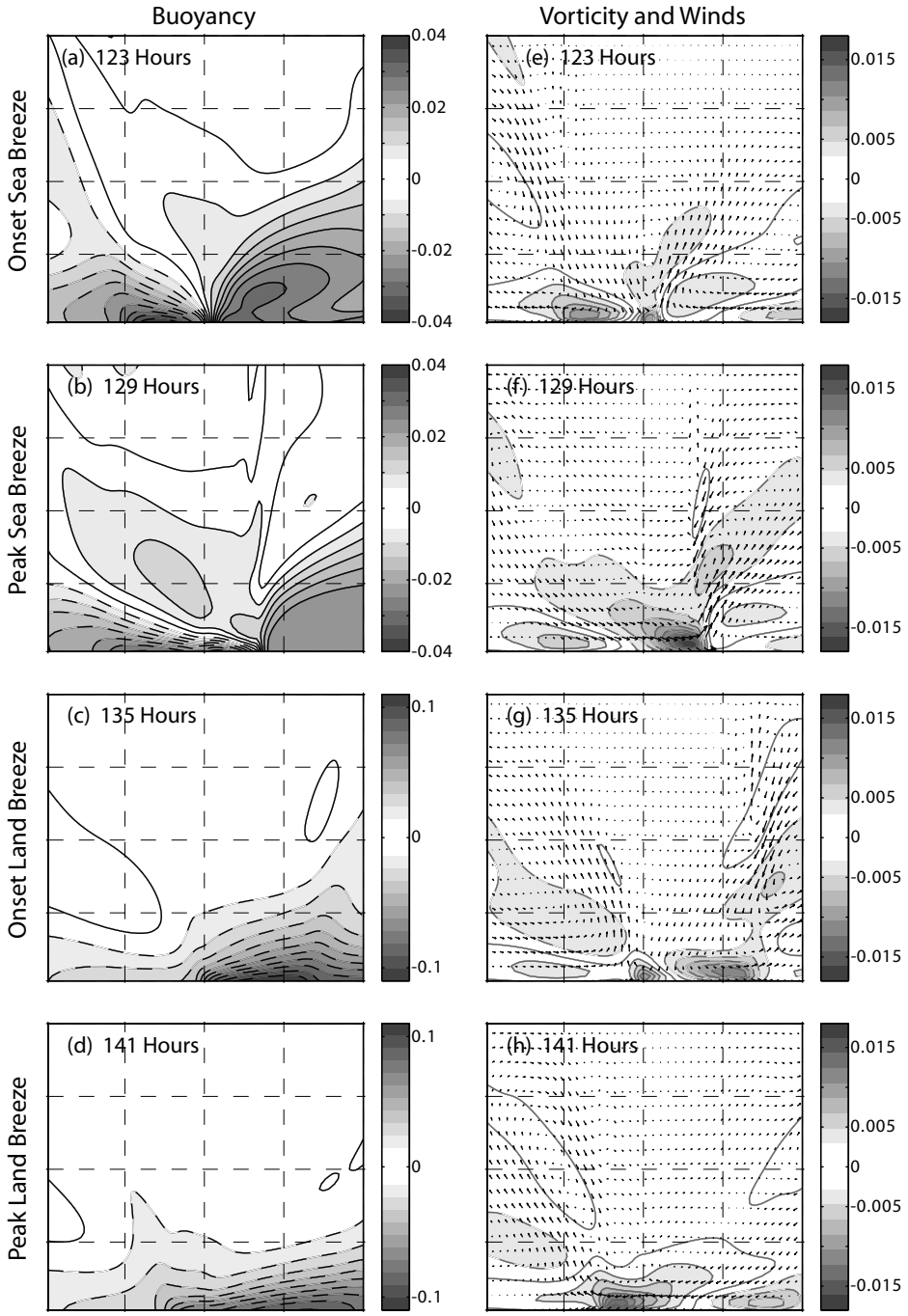

Figure 1. Evolution of the sea and land breeze cycles as observed through the distribution of buoyancy (left panels, ms^{-2}), vorticity (right panels, s^{-1}) , and the wind field (right panels, ms^{-1}) within t he forecast domain at following forecast times: 123 hours (onset of the sea breeze, panels a and e), 129 hours (peak sea breeze, panels b and f), 135 hours (onset of the land breeze, panels c and g), and 141 hours (peak land breeze, panels d and h). Solid (dashed) contours indicate positive (negative) values. Contour intervals are 0.004 ms^{-2} (panels a and b), 0.01 ms^{-2} (panels c and d), and 0.002 s^{-1} (panels e-h).

The sea breeze is triggered by the differential day-time heating that reaches its maximum on land at the 120-hour (noon, maximum heating phase) forecast time (not shown). At this time, while surface convergence and vertical motion set up at the coast, surface winds do not yet indicate the existence of a sea breeze circulation. At 123 hours (Figure 1a and e) the low-level convergence and vertical motion strengthen and the most intense convergence moves inland as weak onshore surface winds develop across the coastline. At 126 hours into the sea breeze cycle (not shown), which coincides with the neutral heating phase, a distinct frontal boundary forms at the leading edge of the sea breeze circulation. The surface buoyancy over land reaches its peak at this time, marking a 6-hour phase difference between maximum heating and maximum temperature over land. The associated buoyancy gradient continues to strengthen the circulation well into the cooling phase of the cycle, and both onshore and vertical winds reach their peak values at 129 hours (Figure 1b and f) The frontal boundary also matures and penetrates almost 100 km inland. While sloping regions of ascent (over land) and descent (over water) mark the ray paths of gravity waves forced by the heating gradient across the coastline, note also that the nonlinear convergence of the frontal boundary has led to a significant gravity-wave signal extending upwards from the boundary layer (Figure 1f and g).

As the cooling phase progresses, the temperature gradient across the coast becomes more negative and the flow at the coast eventually reverses to produce a land breeze. The time of peak land breeze is shown in Figure 1d and h. Note that an offshore-propagating front and associated gravity wave signal are again apparent.

However, comparison of the Figure 1c and d shows that the land breeze front is significantly weaker than the front associated with the sea breeze. This asymmetry in the intensity of the land and sea breezes, which is also commonly observed in real sea/land breezes (Simpson 1994), is apparently the result of the difference in stratification ahead of the respective fronts, with weak stratification ahead of the sea breeze front and essentially unaltered background stratification ahead of the land breeze (Walter 2004).

Structure and evolution of ensemble spread and covariance

The distributions of standard deviation, as a measure of ensemble spread, of variables buoyancy, vorticity, and vertical motion are shown in Figure 2 as they evolve in the sea and land breeze cycle corresponding to Figure 1. Figure 2 indicates a distinct diurnal variability of the ensemble spread both in space and intensity. Both buoyancy and vorticity exhibit spread that is mostly confined to the surface. For buoyancy, this is primarily a result of the initial condition spread projecting onto horizontally uniform perturbations, which can only weaken slowly through vertical diffusion. Vorticity spread is also influenced by heating through the $\partial b' / \partial x$ term in equation (19) yet has a more localized response with most of the signal concentrated around the frontal boundary. Thus, while the vorticity spread is large near the sea and land breeze fronts, the vertically-propagating diurnal gravity waves appear to have very weak signal in the vorticity spread. While the deterministic part of the forcing projects exclusively onto the diurnal frequency, the stochastic part of the forcing projects equally onto all frequencies.

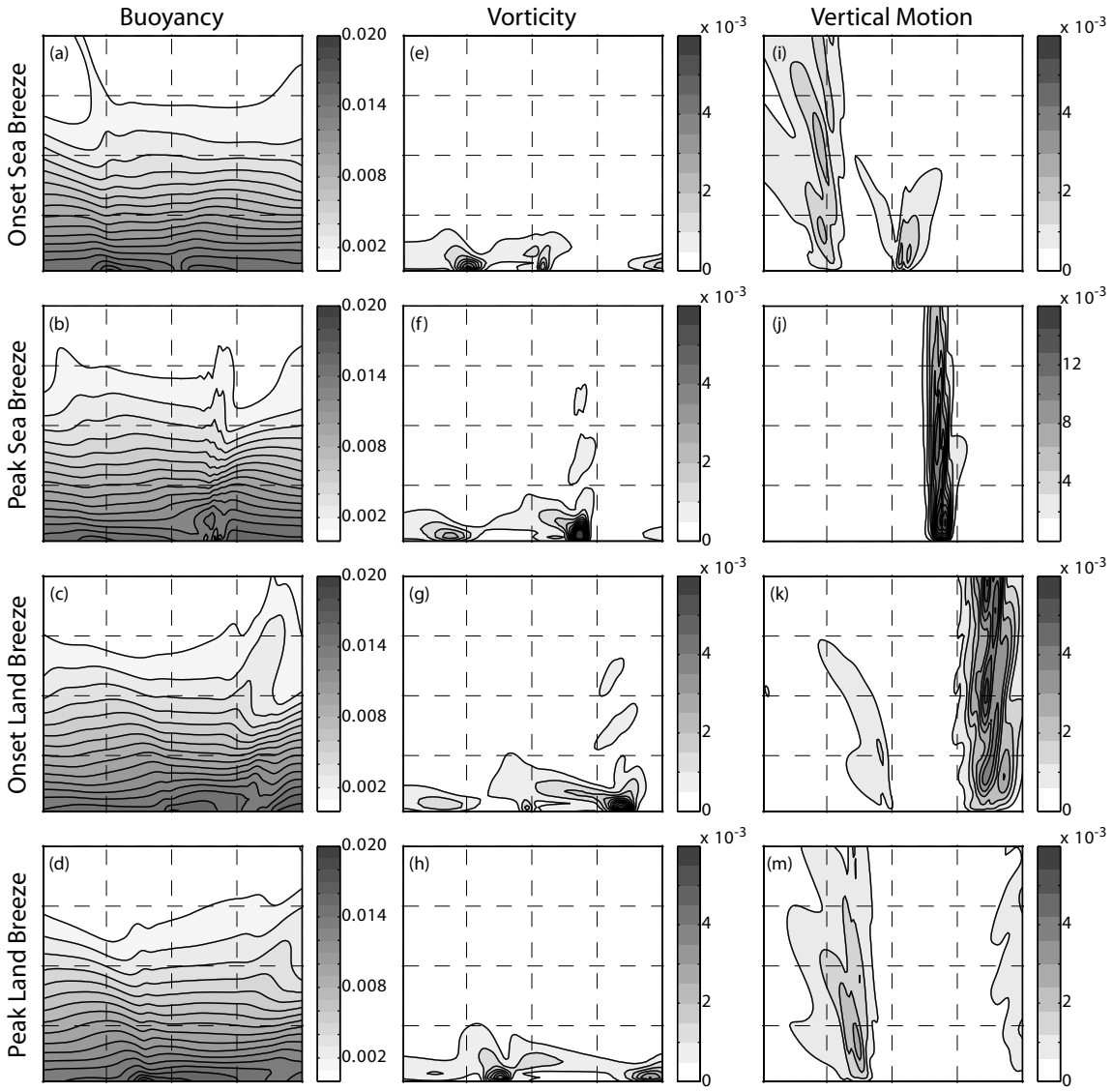

Figure 2. Evolution of the sea and land breeze cycles as observed through the distribution of the standard deviation of buoyancy (left panels, ms^{-2}), vor ticity (middle panels, s^{-1}) , and vertical motion (right panels, ms^{-1}) within the forecast domain at forecast times same as in Figure1. Contour intervals are 0.001 ms^{-2} (panels a-d), 5×10^{-4} s^{-1} (panels e-h), 6×10^{-4} ms^{-1} (panels i, k, and m), and $1.6\times10^{-3}ms^{-1}$ (panel j) .

Thus, while waves excited by the forcing follow a single ray path pair in the linear limit (Rotunno 1983), waves excited by the stochastic forcing exhibit no such preference. Furthermore, most of the diurnal gravity wave spread associated with initial condition uncertainty of vorticity (not shown) will have propagated out of the domain during the three days before the displayed times.

The spatial distribution of the spread of vertical motion is entirely attributable to the timing and location of the frontal boundary. Additionally, the vertically-propagating frontal gravity waves (Figure 1) appear to have their strongest signal in the ensemble spread of vertical motion. This is mainly due to these waves' projecting most of their kinetic energy in the vertical direction as they propagate away from the strong horizontal temperature gradient at the surface.

Corresponding to Figure 2, pointwise (i.e., computed at the same grid point) covariance and correlation coefficient between buoyancy and vorticity are plotted at the different phases of the sea breeze cycle (Figure 3). The covariance structure (Figure 3a-d) reflects the combined response of buoyancy and vorticity spread and thus is mostly concentrated at the surface and is triggered by the frontal boundary. Meanwhile, a much more intricate structure of the correlation coefficient (Figure 3e-h) is exhibited throughout the sea breeze cycle. In the linear limit (Rotunno 1983), variations in the heating intensity would lead to a dominantly negative (positive) correlation structure between buoyancy and vorticity over the sea (land) that is independent of the phase of the sea breeze circulation. This simple structure predicted by the linear theory is

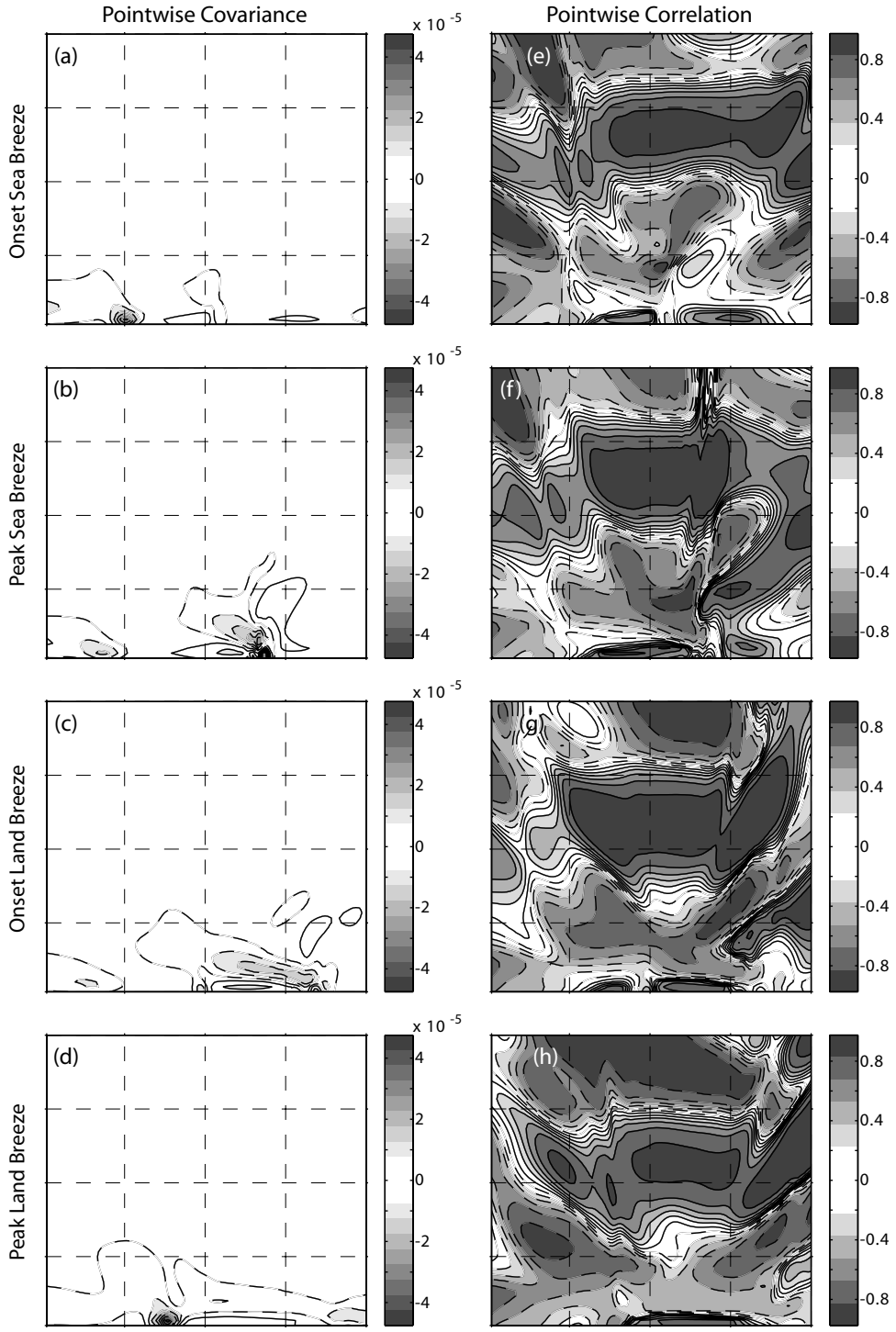

Figure 3. Distribution of pointwise covariance (left panels, ms^{-3}) and po intwise correlation coefficient (right panels) between buoyancy and vorticity at forecast times same as in Figur e 1. Solid (dashed) contours indicat e positive (negative) values. Contour intervals are $5\times10^{-6}ms^{-3}$ (panels a-d) and 0.2 (panels e-h).

modified considerably by the nonlinearities in the model. The global evolution of the buoyancy-vorticity correlation structure during the 6th forecast day (Figure 3e-h) reflects the remnants of the initial-condition correlation structure (not shown). Meanwhile, the local variations near the front are caused by the vertical gravity waves that emanate from the frontal boundary during the peak sea breeze phase (Figure 3f-h, over land). In contrast, during the land breeze phase, the global structure of the initial-condition correlation is only weakly modified by the presence of the front (Figure 3g-h, over sea).

Error dynamics

The 10-day evolution of the ensemble spread (measured by the domain-averaged standard deviation of the ensemble) shows that buoyancy (Figure 4a) and vorticity (Figure 4c) both converge during the first 96 hours, following an initial period of vorticity spread growth. After 96 hours, the buoyancy spread, which is nearly horizontally uniform (Figure 2a-d), exhibits little or no diurnal variation while the vorticity spread, which is associated primarily with fronts, reaches a diurnal maximum when the sea breeze is strongest. A corresponding asymmetry between the buoyancy and vorticity spread is also apparent in their response to initial phase error and stochastic heating error (not shown).

Because of its horizontally uniform structure, the overall distribution of buoyancy spread remains virtually unaltered by the diurnal sea breeze cycle (compare to Figure 2a-d). This is both because of the weak advective tendency due to the horizontal uniformity of the buoyancy spread and the weak vertical diffusion of buoyancy. By

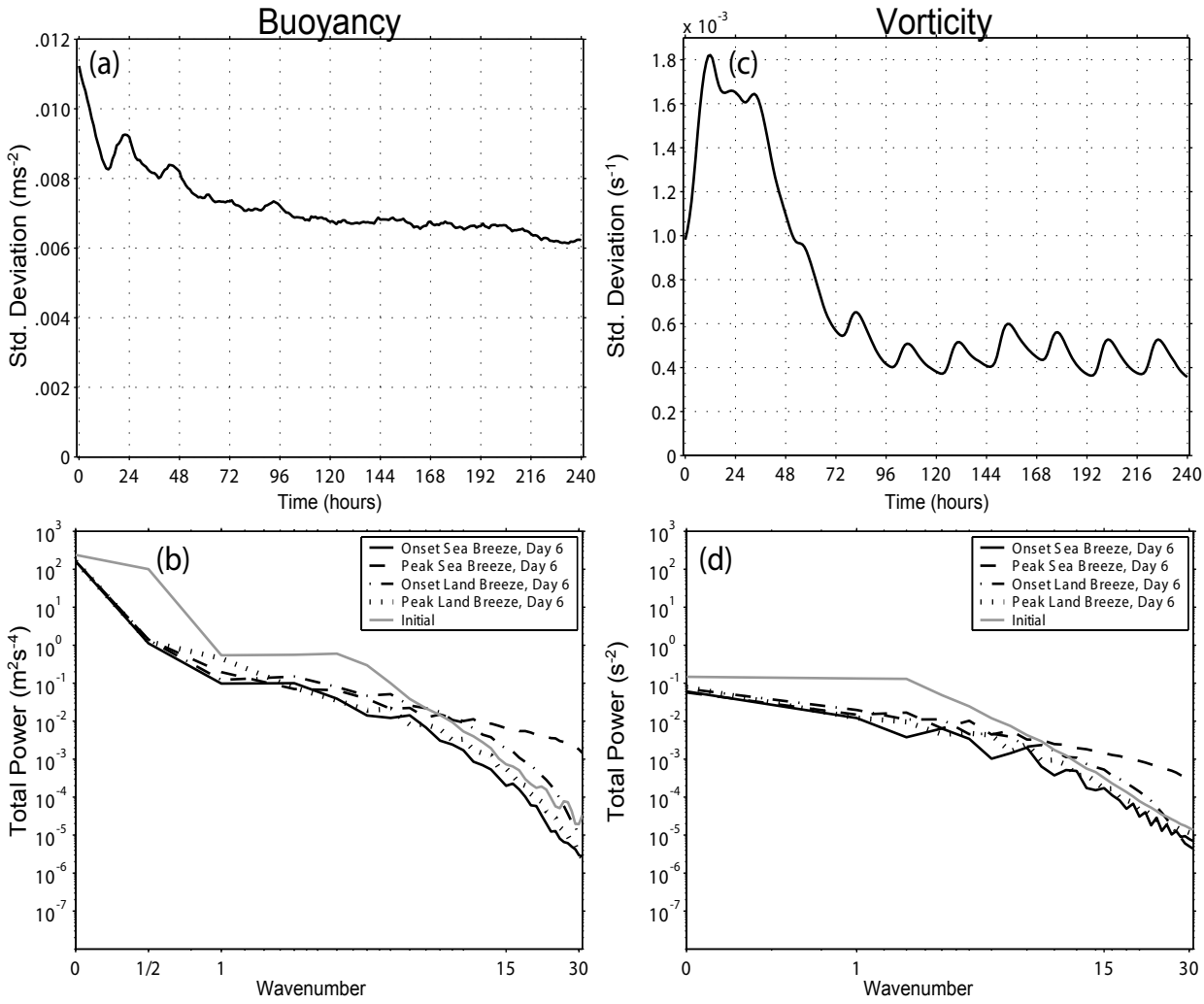

Figure 4. Upper panels: 240-hour evolution of domain-averaged standard deviation of buoyancy (panel a, ms^{-2}) and vorticity (panel c, s^{-1}) from a pure forecast run. Lower panels: Domain-total power spectra of the cumulative difference of each ensemble member and the ensemble mean for buoyancy (panel b, m^2s^{-4}) and vorticity (panel d, s^{-2}) at initial time and forecast times 123 hours (onset of the sea breeze phase, solid), 129 hours (peak sea breeze phase, dashed), 135 hours (onset of the land breeze phase, dashed-dotted), and 141 hours (peak land breeze phase, dotted). Wavenumber 1 corresponds to a wavelength of 500 km while wavenumber 31 approximately corresponds to the double Nyquist wavelength of 16 km.

similar reasoning, then, the localized structure of the vorticity spread that is correlated to the location and intensity of the sea breeze front (compare to Figure 2e-h) is quickly advected out of the domain through the propagation of the front. Consequently, domain-averaged vorticity spread exhibits a pronounced diurnal variability. In addition, because of the tendency to be advected out of the domain at the time scales of frontal propagation, the memory of initial vorticity spread is not retained within the system beyond 96 hours. Once initial spread information is "forgotten", vorticity spread is then controlled by the stochastic heating. During this period (96-240 hours in Figure 4c), vorticity spread grows rapidly through the intensification of the sea breeze front which, due to the stochastic heating, enhances location error (compare to Figure 2f) but does not decay as quickly both because of the lingering sea breeze front and the newly formed weaker land breeze front (compare Figure 2f to h, the vorticity spread within both the old sea breeze front and the newly formed land breeze front is about half of its value of its peak phase). As a result, the spread fluctuates diurnally about a mean value that linearly depends on the standard deviation of stochastic heating amplitude (not shown).

To further investigate the spatial structure of error and confirm the hypothesis about the differences between buoyancy and vorticity spread, spectra of total power of the difference buoyancy (Figure 4b) and difference vorticity (Figure 4d) are plotted as a function of horizontal wavenumber at the four different phases of the sea breeze cycle, where differences are determined from the mean for each ensemble member and then the spectra are summed across ensemble members and vertical levels. In order to minimize aliasing due to the "half-wavelength structure" of buoyancy (i.e. the common case of

alternating values from one half of the domain to the other), its power spectra are computed after patching the entire forecast domain horizontally. This gives rise to wavenumber "1/2" on buoyancy power spectra plots. The large-scale structure of spread is evident for both variables. Yet, as conjectured in the previous paragraph, while both variables lose power selectively at larger scales as the experiment proceeds into the sixth day, buoyancy remains to be dominated by wavenumbers 0 and 1/2, which is an indication of retained memory of initial conditions. Vorticity power, on the other hand, appears to have become almost "white" between wavenumbers 0-10 and exhibits a much "flatter" spectrum compared to buoyancy. This confirms the hypothesis that, compared to buoyancy, initial conditions have a much smaller impact on the later evolution of the vorticity spread.

Active frontal dynamics in the sea breeze change the power spectra considerably and introduce smaller-scale structure to both variables. While the power of buoyancy spread increases by about 3 orders of magnitude at wavenumber 30, the overall spectrum remains "red" with power in wavenumbers 0 and 1/2 still larger by about 5 and 3 orders of magnitude, respectively. Consequently, domain-averaged buoyancy spread exhibits no noticeable diurnal signal at later stages of the experiment. On the other hand, the vorticity spread reveals a much more pronounced influence of smaller scales at the peak sea breeze phase so that the power at smaller scales becomes almost comparable in magnitude to the power at larger scales. The relatively large power at smaller scales projects into rapid error growth and results in the distinct diurnal signal in the vorticity spread. Despite this considerable contribution of error at smaller scales during the peak

sea breeze phase, the system appears to lack a mechanism to grow smaller-scale errors into larger scales. As a result, beyond day-to-day variability, overall level of error remains relatively stable (i.e., error saturation), not showing signs of long-term growth.

b. Filter Performance

Filter evaluation is carried out using the sequential square-root EnKF as explained in the first chapter and its basic properties as described in section 1.b of this chapter. In these tests, simulated land-surface observations (thus spanning only half of the domain at surface) of buoyancy were used with 40-km horizontal spacing and an assumed observational error of 10^{-3} ms^{-2}. Analyses are performed every 3 hours, beginning with the 3-hour forecast. While the entire simulation domain (including the sponge layers) are used to perform analyses and simulate observations, statistics are computed within the main (interior) domain. Thus, the dimension of the state vector is 55000, while the number of observations simulated for each analysis cycle is 13 and the ensemble comprises 50 members. In the following sections, results are presented through the investigation of error structure and filter sensitivity.

Error characteristics

The evolution of root-mean square (rms) error and ensemble spread of prognostic variables buoyancy and vorticity from a 144-hour run is shown in Figure 5. During the first analysis cycle, a large reduction in buoyancy error occurs with a correction of about 83% (Figure 5a), while vorticity error reduction is 42% (Figure 5c). Subsequent error reduction between hour 3 and hour 144 analysis is about 90% for both variables. In

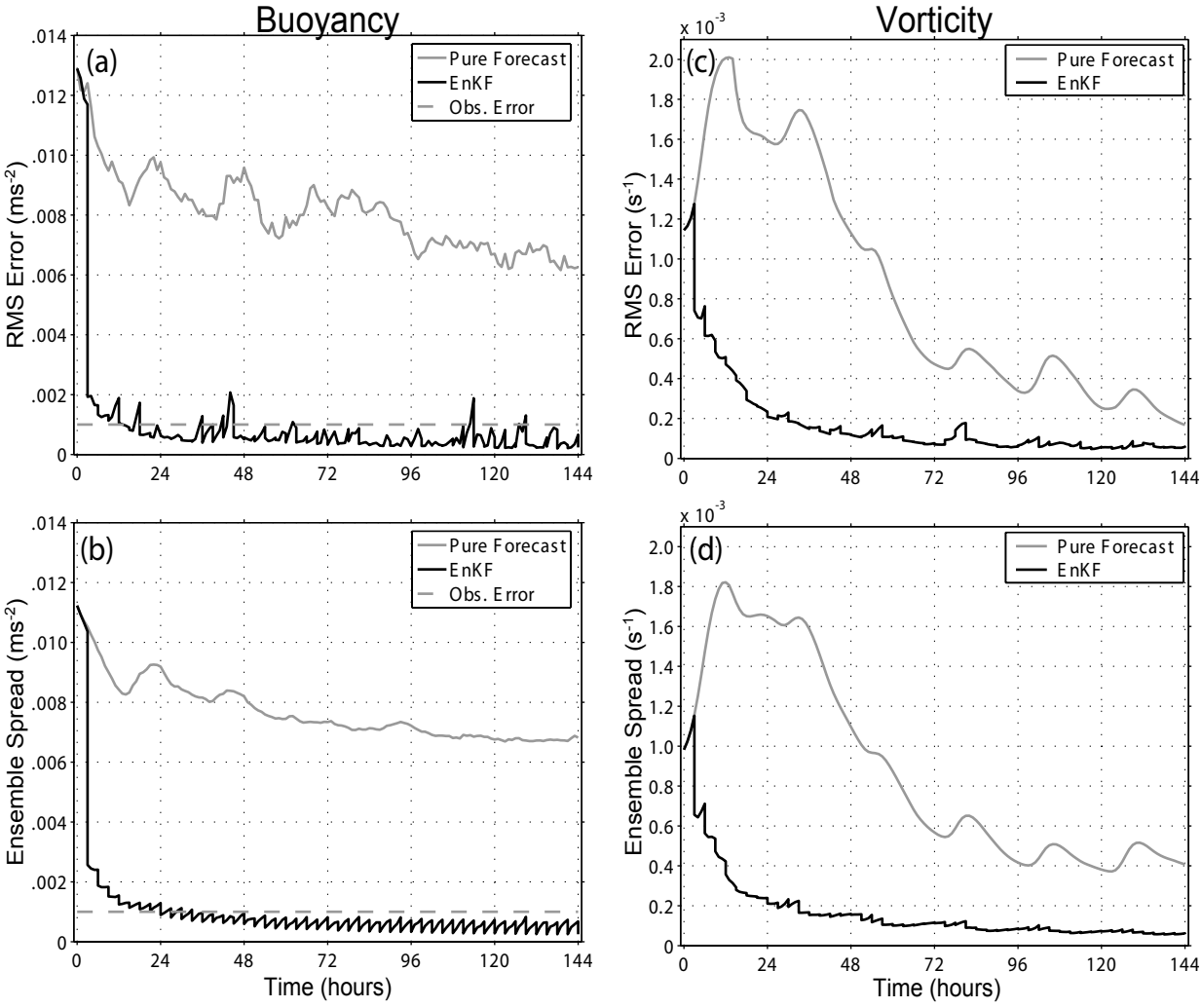

Figure 5. 144-hour evolution of EnKF buoyancy rms error (panel a, ms^{-2}), buoyancy domain-averaged standard deviation (panel b, ms^{-2}), vorticity rms error (panel c, s^{-1}), and vorticity domain-averaged standard deviation (panel d, s^{-1}) plotted in solid black. Analyses are performed at 3-hour forecast intervals. In each panel, respective metric from the pure forecast run is plotted in solid gray for comparison.

addition, buoyancy error appears to grow considerably during the 3-hour forecast runs between each analysis cycle although the error introduced in that manner is immediately removed at the following analysis step so that the overall error saturates at a level that is comparable to the observation accuracy (10^{-3} ms^{-2}). Meanwhile, vorticity error growth between analysis cycles has a diurnal nature with strongest error growth occurring during the peak sea breeze phases. Eventually and similar to buoyancy, vorticity error settles to a level that is both controlled by observational accuracy and stochastic uncertainty. The error settling time for both variables is about one day.

To compare how error is reduced during an analysis step, the domain-wide distribution of prior and posterior rms error of buoyancy and vorticity is shown in Figure 6 at the first analysis step (3 hours) and two peak sea breeze phases (9 and 129 hours). At 3-hour model time (Figure 6a-d), domain-wide error of both variables is removed considerably in accordance with the large first-analysis error reduction that is observed in Figure 5 (errors in the left quarter of the domain are not reduced due to the constraint of the radius of influence). Further investigation reveals that most of the error removed is larger-scale error that is associated with the ensemble initialization (mostly phase differences between different times that were chosen as ensemble members). Remaining errors are concentrated mostly around the strong temperature gradients which are the focus of nonlinear frontal dynamics.

At 9 hours, which is the third analysis step and coincides with the peak sea breeze phase, the forecast rms error (Figure 6e, g) of both variables exhibit significant

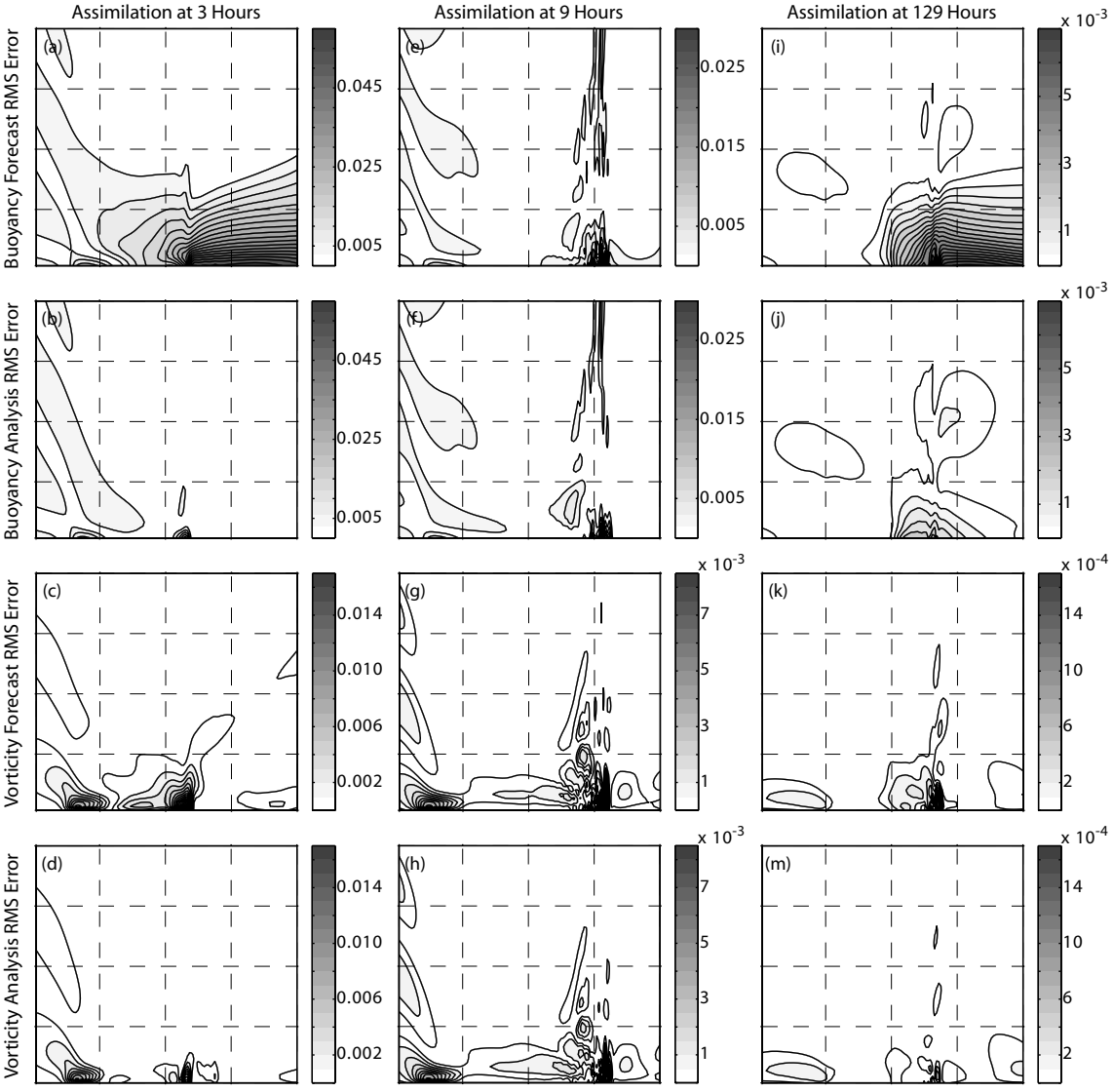

Figure 6. Domain distribution of prior (forecast) and posterior (analysis) rms error of buoyancy (ms^{-2}) and vorticity (s^{-1}) at 3 hours (first analysis, panels a-d), 9 hours (peak sea breeze phase of day 1, panels e-h) and 129 hours (peak sea breeze phase of day 6, panels i-m) from the same EnKF run as in Figure 5. Contour intervals are 0.003 ms^{-2} (panels a and b), 0.001 s^{-1} (panels c and d), 0.0015 ms^{-2} (panels e and f), 5×10^{-4} s^{-1} (panels g and h), 3.5×10^{-4} ms^{-2} (panels i and j) , and 1×10^{-4} s^{-1} (panels k and m).

small-scale error growth compared to the 3-hour analysis rms error. For both variables, the strongest error is located at the surface around the front with weaker error extending vertically and showing a distinct gravity wave structure. In addition, a much weaker buoyancy error is found at the surface that extends uniformly over land which is the result of the stochastic heating error. At this time, small-scale errors due to active frontal dynamics dominate over larger-scale errors due to stochastic heating, illustrating that initial frontal errors are not immediately eradicated by the first few analyses. On the other hand, the larger-scale buoyancy error over land surface is completely removed.

At 129 hours, which is the peak sea breeze phase of the sixth day of the experiment, the distribution of forecast rms error of buoyancy (Figure 6i) shows a distinct large-scale structure much similar to the forecast error distribution at 3 hours (Figure 6a). Embedded in that structure, a small-scale signal is also discernible at the sea breeze front location which is strong in magnitude yet very localized at the surface and weakly extends upward. Comparison of this structure to the 9-hour distribution (Figure 6e) suggests that repeated 3-hour analyses have removed most of the remaining small-scale error caused by initial conditions, so that forecast error is now predominantly generated through the stochastic uncertainty of heating. In contrast to buoyancy but consistent with Figure 2f, forecast rms error of vorticity appears to have retained its small-scale structure (Figure 6k). As explained before, this is the result of vorticity's sensitivity to the location error of the front that also enables the error to be advected out of the forecast domain. Similar to previous times, the filter at this time successfully removes most of the large-scale error of buoyancy (Figure 6j), leaving some buoyancy

error behind the sea breeze. Similarly, considerable reduction also occurs in vorticity error (Figure 6m) and most of the error within the frontal and gravity-wave structure is eliminated. From this visual analysis, surface buoyancy observations with 40 km spacing, in addition to their information content at their natural large-scale resolution, appear to contain valuable information relevant at the scales of frontal convergence. As a result, the filter not only effectively removes large-scale errors due to stochastic heating but performs also well at reducing small-scale error due to nonlinearities at the front.

To further examine the scale-sensitive behavior of the filter, power spectra of the two variables are plotted at 3, 9, and 129 hours (Figure 7). At the first analysis step of the model (Figure 7a and d), both variables exhibit the greatest error reduction at large scales primarily as a result of the error content of initial conditions being predominantly large-scale. At 9 hours, because of the fact that considerable small-scale error still exists in the forecast domain (compare to Figure 6b and h) that further intensifies during the active sea breeze phase, power spectra of both variables exhibit significantly larger energy at small scales compared to the initial time (Figure 7b and e). This small-scale buoyancy error growth naturally occurs faster than the large-scale error growth normally induced by stochastic heating so that the increase in the power at wavenumbers 0, 1/2, and 1 is smaller for the 9-hour forecast. Consequently, the larger-scale information content of buoyancy observations at 9 hours contributes very little to the EnKF analysis and thus reduction in large-scale power is small (almost nonexistent for vorticity). At

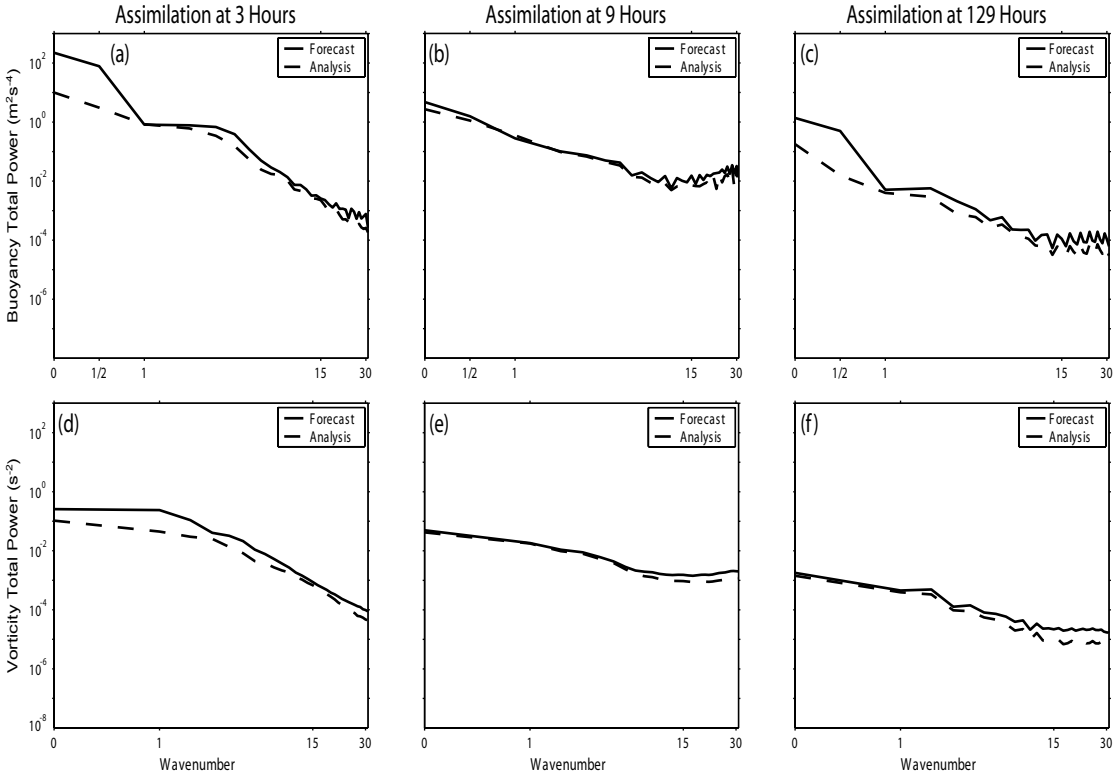

Figure 7. Domain-total power spectra of the cumulative difference of each ensemble member and the ensemble mean for buoyancy (panels a-c, $m^2 s^{-4}$) and vo rticity (panels d-f, s^{-2}) at forecast (prior, solid lines) and analysis (posterior, dashed lines) steps of 3 hours, 9 hours, and 129 hours.

129 hours, as the small-scale error becomes saturated after repeated 3-hourly analyses, stochastic heating uncertainty becomes dominant and generates large-scale buoyancy error which is then more effectively removed by the filter (Figure 7c). On the other hand, vorticity error still continues to be mainly concentrated at the front and retains its small-scale structure. As a result, reduction in power occurs mostly at smaller scales (Figure 7f) and its magnitude becomes comparable to that of the large-scale reduction at the 3-hour assimilation (Figure 7d). This confirms the hypothesis that surface buoyancy observations with 40-km spacing contain sufficient small-scale information so that the filter performs well at reducing especially the small-scale vorticity errors associated with the nonlinear frontal processes.

Sensitivity to observation accuracy, ensemble size, analysis frequency, radius of influence, observation spacing, and type of observations

Experiments are also carried out to investigate the extent and nature of the sensitivity of the filter to various filter-related parameters. The results are presented in the form of comparative rms error plots of the unobserved variable vorticity (Figure 8). In these plots, comparison is made between the parameter value in the control experiment (discussed on pp. 35-47) and two other parameter values, one larger and one smaller than the control parameter value. In general, vorticity error is found to be sensitive to all parameters especially during the first 24 hours of the assimilation experiments. In all of the cases, errors begin with a relatively large

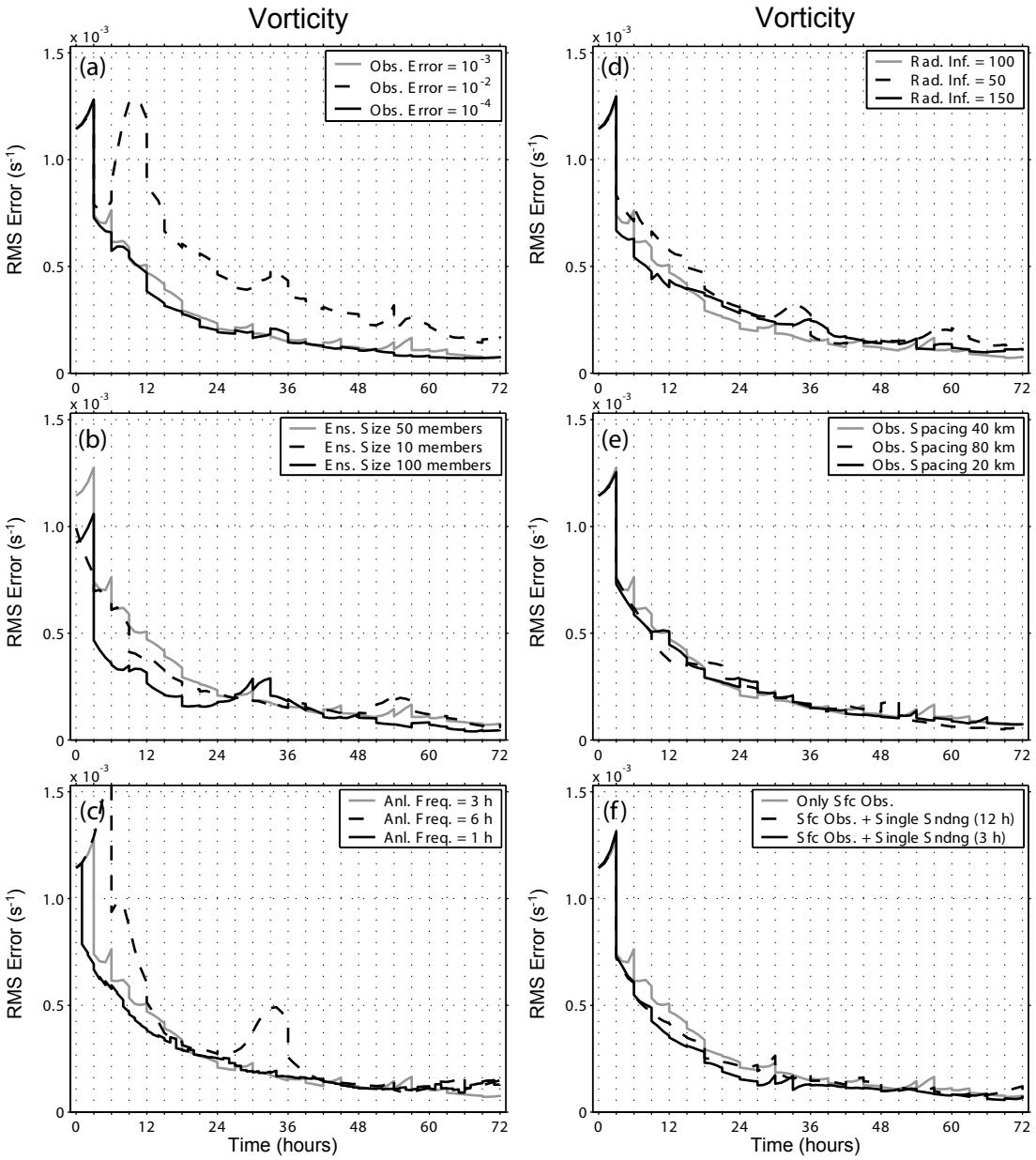

Figure 8. Sensitivity of rms error of the unobserved variable vorticity (s^{-1}) to (a) observation accuracy, (b) ensemble size, (c) analysis frequency, (d) radius of influence, (e) observation spacing, and (e) assimilation of a single additional sounding.

difference between the experiments and, except observation accuracy, converge toward each other at later stages of the experiments so that error differences become progressively smaller. An interesting behavior is observed with the sensitivity to observation accuracy: While more accurate observations (10^{-4} ms^{-2}, one order of magnitude smaller than the control experiment) have almost no positive impact on vorticity error, loss of observation accuracy (10^{-2} ms^{-2}) results in considerably larger error (a more proportional response to observation accuracy is exhibited by buoyancy error which is not shown here).

Finally, one common behavior is believed to be linked to the large-scale nature of buoyancy. Parameters that exhibit similar characteristics in this respect are observation spacing (Figure 8e) and assimilation of an additional buoyancy sounding observation located about 90 km inland from the coast (Figure 8f). In both cases, vorticity error is not particularly sensitive to the variations in the chosen parameter. Apparently, the information content of buoyancy observations remains mostly unchanged so that the smaller-scale features of the flow are not sampled more effectively by either an additional sounding or a reduction of observation spacing to 20 km.

SIMULTANEOUS STATE AND PARAMETER ESTIMATION WITH THE TWO-DIMENSIONAL SEA BREEZE MODEL

1. Modifications to the Model and the Filter to Accommodate Estimation of Parameters

a. Initialization of Parameters

As there is no "climatological information" available for model parameters, a random perturbation technique was chosen for the ensemble initialization of the model parameters to be estimated. An important issue at this point is the magnitude of variance since no straightforward guidance exists for the proper range of variance of the individual parameters to be estimated, although clearly the magnitude to be chosen will have a direct and significant impact on how well the parameter in question can be estimated. Moreover, the initial spread of the parameter should ideally be also restricted by the amount of parameter error the system is likely to possess. In this study, the ensemble spread for each parameter is initialized such that the standard deviation is equal to the initial error (absolute difference between initial mean parameter value and true parameter value) to ensure reliable initial ensemble statistics.

b. Treatment of Parameter Variance

Another modification to the original form of the EnKF analysis scheme is related to the treatment of parameter variance. This is a fundamental issue because, if not given special attention, it may lead to filter divergence. In filtering applications, filter divergence commonly occurs when prior distribution becomes too narrow so that

observations have progressively smaller impact (Anderson and Anderson 1999). In this regard, parameter estimation imposes a special challenge because parameters are not dynamical variables. In other words, while the variance of both model variables and parameters is reduced at an analysis step, between analysis steps the model can only contribute to the variance of model variables while parameters remain constant. As a result, parameter spread remains unchanged between analysis steps only to be reduced again during the following analysis step. This leads to a progressively decreasing parameter variance and eventually may cause filter divergence especially if the mean parameter value does not promptly converge toward the true value or the true parameter value varies in time.

The method chosen to treat posterior parameter spread is related to the inflation technique Anderson and Anderson (1999) employed; although here, instead of multiplying the posterior standard deviation of a given parameter by a constant factor as they did, posterior standard deviation is inflated back to a minimum predefined value when necessary. In the present study, the predefined standard deviation is empirically chosen as 1/4 of the initial standard deviation. When the posterior standard deviation is smaller than this value, the parameter spread is adjusted back to it. In the experiments described here, the posterior standard deviation usually decreases to 1/4 of its initial value in the first few analysis cycles, and then remains constant at that predefined value throughout the remainder of the experiment. With this technique, a respective parameter is guaranteed to contain a minimum amount of spread, and this spread cannot grow uncontrollably through inflation. The minimum amount of spread specified through the

variance inflation technique would ideally reflect the acceptable variability of a given parameter with negligible impact on the state variables, although the level chosen here is somewhat empirical and the sensitivity of the performance of the estimation process to the chosen limit is further analyzed in this chapter.

c. Selection of Parameters to Be Estimated

The criterion for the selection of parameters to be estimated was motivated by the necessity to work with a parameter space that would reflect the realistic model error associated with the sea breeze circulation. In this regard, several factors influence the circulation and, for this reason, are critical from a numerical modeling point of view (Simpson 1994): (1) Diurnal variation of the ground temperature, (2) diffusion of heat, (3) spatial and diurnal variation of static stability, (4) Coriolis force, (5) diffusion of momentum, (6) topography, and (7) prevailing winds. Up to six model parameters that control many of these critical factors are subjected to estimation attempts in various experiments. In their current form, these parameters are global and not varied spatially. For each model parameter, its true value must be chosen along with the value initially used by the imperfect model. These parameters and their values are given in Table 1. In all cases, the initial standard deviation of each parameter is chosen to be equal to the respective initial error. Parameters that are not estimated are left unperturbed at their perfect (true) value.

Table 1. Model parameters and their values as they were used in estimation experiments.

Parameter (Symbol, unit)	True Value	Initial Imperfect Mean Value
Mean horizontal wind ($\overline{u}$, ms^{-1})	0.50*	1.00
Static stability (N^2, s^{-2})	10^{-4}	1.2×10^{-4}
Vertical diffusion coefficient of vorticity (κ_η, ms)	0.50	0.75
Vertical diffusion coefficient of buoyancy (κ_b, m^2)	0.50	0.75
Heating amplitude (A_0, ms^{-3})	7.00×10^{-6}	6.25×10^{-6}
Heating depth (z_0, m)	500	600

* When $\overline{u}$ was not among estimated parameters, its value was set at 0 ms^{-1} for computational efficiency purposes.

2. Results

a. Single-Parameter Results

Results from the individual estimation of the six parameters mean horizontal wind ($\overline{u}$), static stability (N^2), vertical diffusion coefficients of vorticity (κ_η) and buoyancy (κ_b), heating amplitude (A_0), and heating depth (z_0) are presented in Figure 9 and Figure 10. Thus, in each experiment, only one such parameter is perturbed (about its imperfect mean value) and the estimation is performed through state augmentation and updating of the composite state vector while other parameters are kept unperturbed at their correct (true) value. For each parameter case, the averages of five independent experiments are computed to reduce random variations. Figure 9 shows the 72-hour evolution of the mean parameter values along with the true parameter values that stay constant in time. The shaded area around the estimated mean parameter value is intended to provide a visual guidance for the variability: It represents the 1-σ (one standard deviation) limits of the parameter spread. When ensemble statistics are perfect, the true parameter value should be expected to be found within this interval 68% of the time. In addition to the mean parameter value, the evolution of the rms error of buoyancy and vorticity can be observed in Figure 10 where the results are shown for 4 of the 6 parameters ($\overline{u}$, N^2, κ_η , z_0) for which the strongest sensitivity in terms of rms error is exhibited. In all of the rms error panels, the rms error from the respective estimation experiment is plotted along with the rms error from the best-case and worst-case experiments. Best-case results are obtained with perfect parameters; they represent the

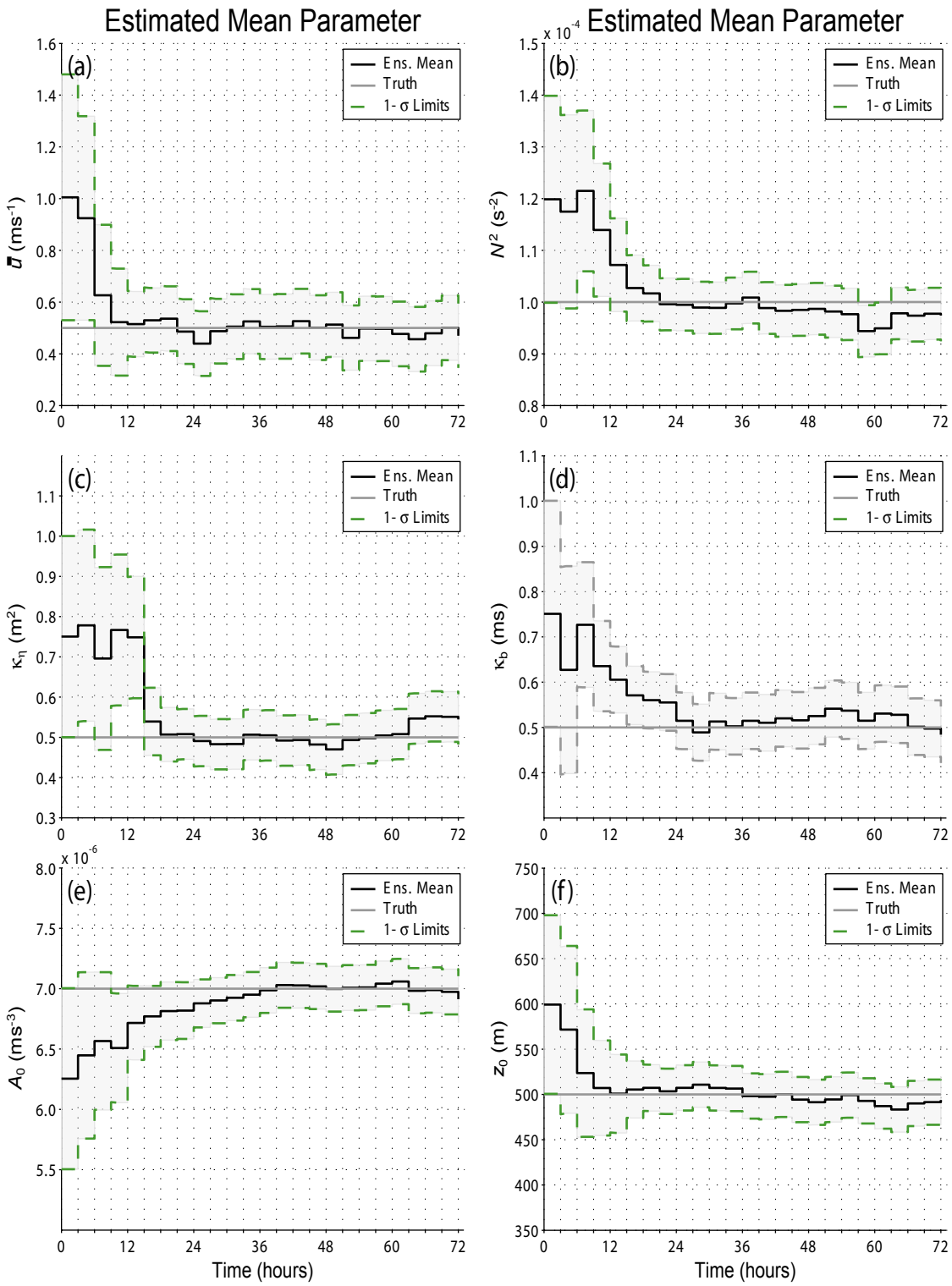

Figure 9. The time evolution of the mean parameter value (solid black) vs. the true parameter value (solid gray) from single-parameter estimation results. Estimated parameters are mean horizontal wind (panel a), static stability (panel b), vertical diffusion coefficient of vorticity (panel c), vertical diffusion coefficient of buoyancy (panel d), heating amplitude (panel e), and heating depth (panel f). The shaded area represents the one-standard-deviation limits of the parameter spread.

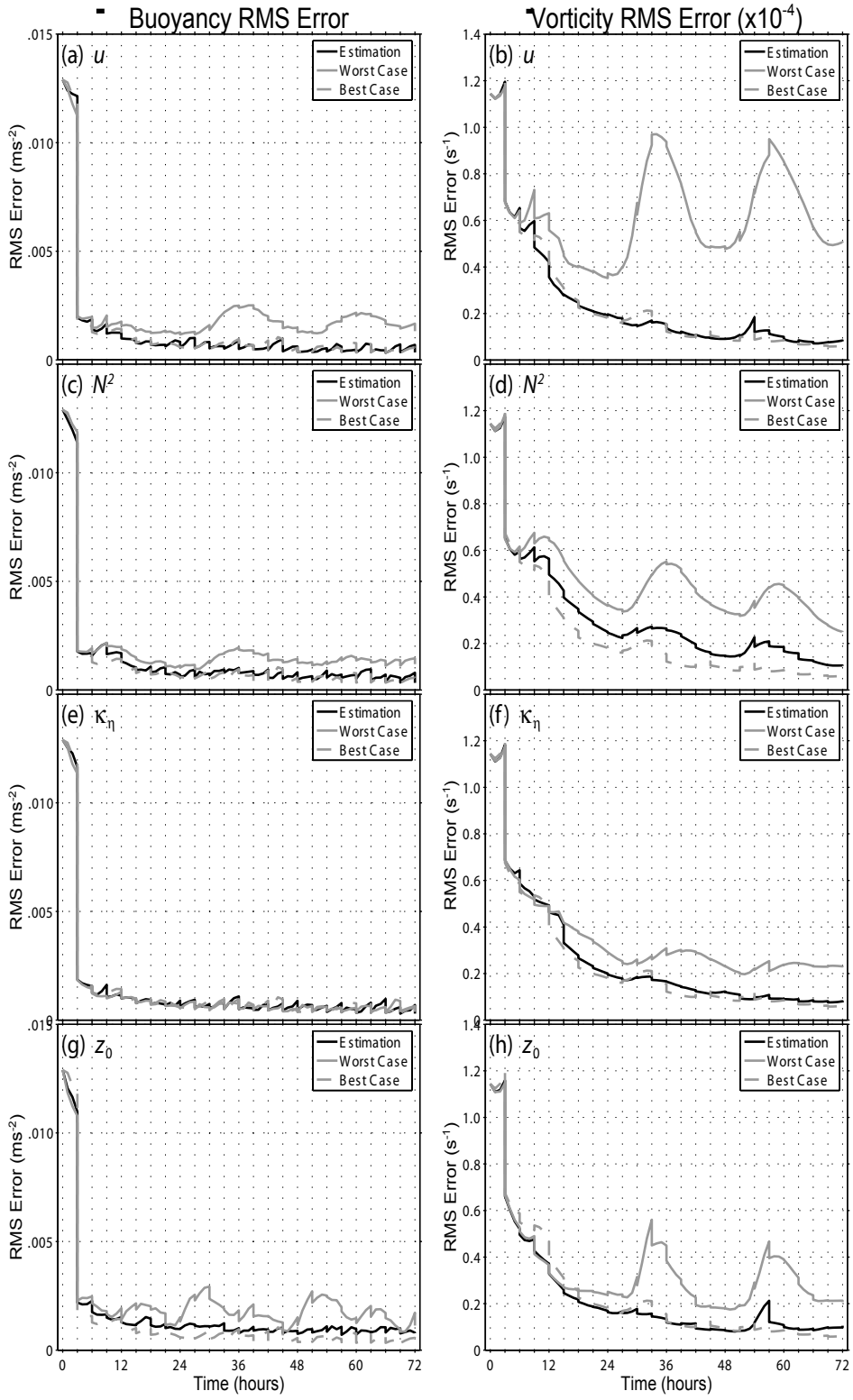

Figure 10. The time evolution of the rms error (solid black) of buoyancy (left panels) and vorticity (right panels) from single-parameter estimation results compared to the rms error of the worst-case (solid gray) and best-case (dashed gray) experiments. Parameters shown are horizontal wind (panels a, b), static stability (panels c, d), vertical diffusion coefficient of vorticity (panels e, f), and heating depth (panels g, h).

upper bound for how well the filter performance can be expected to be. Worst-case results are obtained with imperfect parameters and no parameter estimation; they represent the lowest acceptable bound for filter performance.

Comparing the evolution of the mean estimated parameter values, it can be seen that estimated values of all six parameters approach true values within the first 24 hours (8 assimilation cycles) of respective experiments and subsequently the true values stay almost always within the 1-σ interval. Further analysis reveals that the rate of approach to the true values varies among the six parameters. As a measure of the rate of approach to truth, "approach time" is defined as the duration it takes for a true parameter value to frst fall within the 1-σ interval about the estimated mean that corresponds to the "desired" uncertainty level of 1/4 initial error (ideally, acceptable uncertainty). It can be seen that the approach times of all parameters are ~12-18 hours. The six parameters also show similarities with respect to the variability of their mean estimated values; the respective true values remain exclusively within the 1-σ interval even exceeding the 68% expectancy. In general, it is concluded that the estimation of the mean values of all six parameters individually is successful with acceptable variability of mean estimated values.

The evolution of the rms error of both model variables is also consistent with the findings on the behavior of the mean estimated parameter values. A quick visual comparison reveals that, for all parameters, the rms error of the estimation experiments is lower than that of the worst-case experiments. While the estimation experiments are indistinguishable from the best-case experiments for the parameters $\overline{u}$ and κ_η, for N^2 and

z_0 the rms error remains slightly above but nevertheless very close to its best-case value. As a result, both time-averaged rms error and standard deviation of rms error demonstrate comparable magnitudes for the parameter estimation and best-case experiments (not shown).

One metric for the quantitative comparison of relative filter performance is what is coined the "marginal rms error" (MRE) and is computed as follows:

$$\mathrm{MRE} = \frac{\left(\left\langle \mathrm{RMSE}_{\mathrm{Experiment}} \right\rangle \; - \; \left\langle \mathrm{RMSE}_{\mathrm{Best\ Case}} \right\rangle\right)}{\left(\left\langle \mathrm{RMSE}_{\mathrm{Worst\ Case}} \right\rangle \; - \; \left\langle \mathrm{RMSE}_{\mathrm{Best\ Case}} \right\rangle\right)} \times 100, \qquad (21)$$

where RMSE stands for rms error and the operation $\langle \cdot \rangle$ denotes time averaging over the entire experiment. The MRE is a relative measure of how much error remains from the initially imperfect parameter specification. From a buoyancy MRE point of view, the worst estimation performance is exhibited by the parameters z_0 (33%) and N^2 (18%), while from a vorticity point of view by N^2 (30%) and κ_η (15%). While these findings further substantiate the conclusion about the success of the estimation of single parameters, they also hint to minor variabilities among parameters in terms of the potential impact of the EnKF for more complicated situations.

b. Multiple-Parameter Results

Having established the potential of the EnKF for parameter estimation through single-parameter experiments, a rigorous approach of testing the filter for an increasing number of parameters has been adopted to obtain a more systematic picture of the EnKF's capability and limits in providing improved analyses when multiple imperfect parameters are involved. Here, the results from two different 3-parameter cases and

subsequently the 6-parameter estimation case are presented. Again, for each case, the averages of five independent experiments are computed to minimize random variations. The 3-parameter experiments are performed with N^2 / κ_η / A_0 and $\overline{u}$ / N^2 / z_0 as imperfect triplets. Imperfect parameters that were estimated in the six-parameter experiments are $\overline{u}$, N^2, κ_η, κ_b, A_0, and z_0.

Figure 11 and Figure 12 show the evolution of the mean parameter values from the 3-parameter experiment with N^2 / κ_η / A_0 and $\overline{u}$ / N^2 / z_0 as imperfect parameters, respectively. The performance of the simultaneous estimation of both of the parameter triplets is comparable to that of their individual estimations. Similar to single-parameter experiments, the approach time for all parameters is ~12-18 hours (Figure 11). Once within the 1-σ acceptable uncertainty range, all parameters appear to show similar variability, with respective true values staying within the 1-σ interval most of the time. Furthermore, error evolution of model variables is also very good for both cases. Because of their similarity, only the rms error evolution for the triplet $\overline{u}$ / N^2 / z_0 is shown here (Figure 13). We see that while the vorticity MRE is 20%, for buoyancy it is 30%. In general, it is concluded that the estimation with 3 uncertain parameters produces consistently improved results (relative to the worst-case experiments) that are independent of the parameters estimated and are very similar in nature to single-parameter estimation results. Similar results are also obtained from four-parameter estimation experiments (not shown) that are performed with sets $\overline{u}$ / N^2 / κ_b / z_0 and $\overline{u}$ / N^2 / κ_η / z_0.

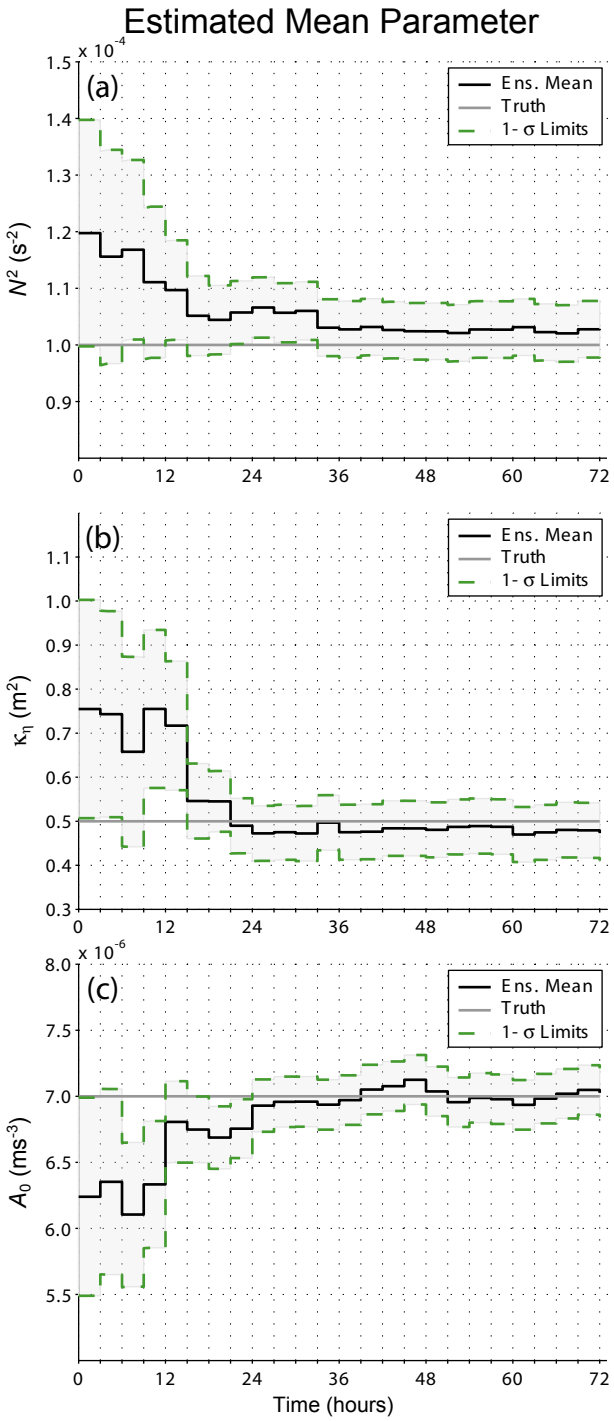

Figure 11. As in Figure 9 but for the simultaneous estimation of 3 parameters (static stability, vertical diffusion coefficient of vorticity, and heating amplitude).

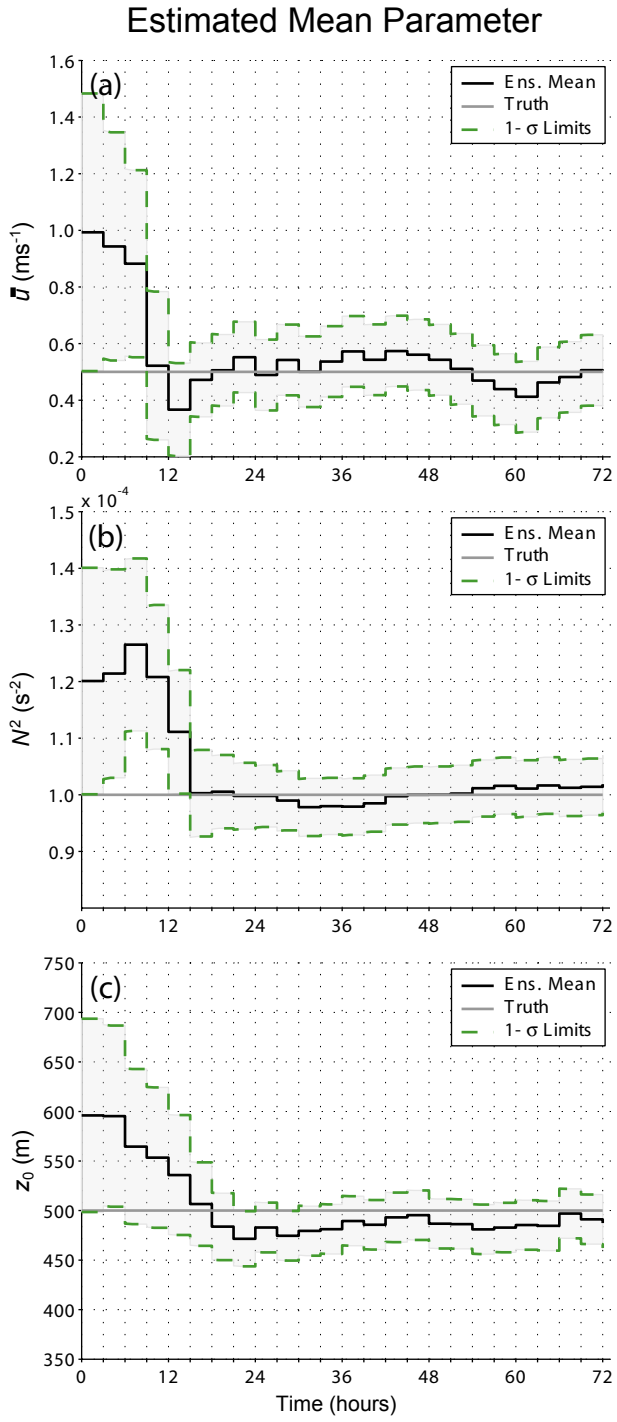

Figure 12. As in Figure 9 but for the simultaneous estimation of 3 parameters (mean horizontal wind, static stability, and heating depth).

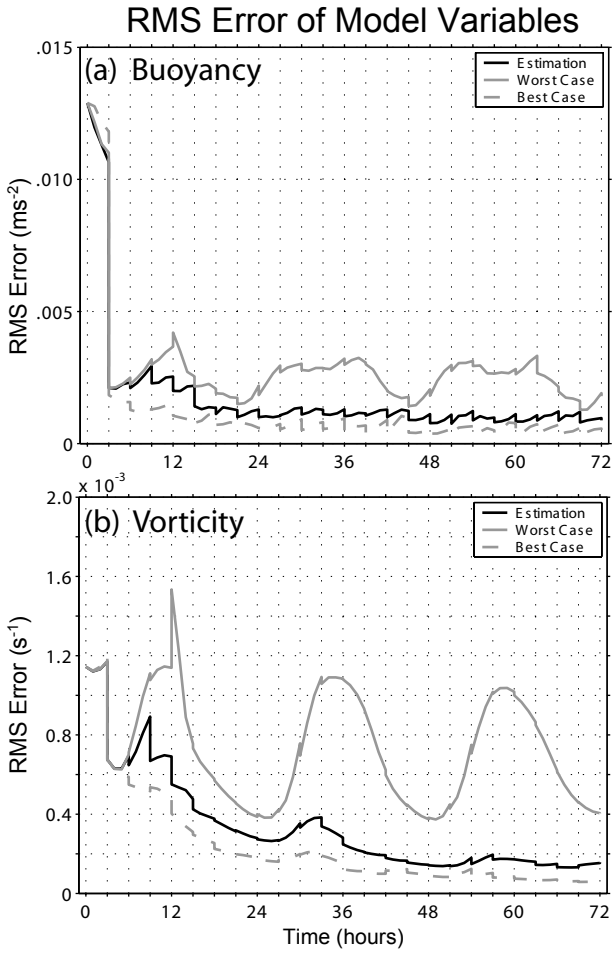

Figure 13. As in Figure 10 but for the simultaneous estimation of 3 parameters (mean horizontal wind, static stability, and heating depth) corresponding to Figure 8.

When the uncertainty is extended to the entire set of 6 parameters, some deterioration of the estimation performance is observed (Figure 14). We see that while the mean values of the parameters $\bar{u}$, κ_b, A_0, and z_0 (Figure 14a, d, e, f) are still successfully estimated so that the true values remain within the respective 1-σ interval most of the time, this is not the case for N^2 and, to a smaller extent, for κ_η (Figure 14b, c). The weakened performance in the estimation of N^2 is especially noteworthy as its true value stays systematically below the 1-σ interval during the entire 72-hour duration, although some convergence between the true and estimated mean values is still noticeable. We also see that there is a distinct increase in both the buoyancy and vorticity rms errors (Figure 15). For the 6-parameter experiments, the buoyancy MRE is computed as 60% and the vorticity MRE is a relatively lower 54%, both of which are consistently higher than their respective 3-parameter estimation counterparts.

Despite the worsened estimation of N^2 and κ_η, it is nevertheless concluded that the overall performance of the filter in reducing the parameter-related model error is still very good. While, out of the 6 uncertain parameters, the mean values of the 4 converge toward their respective true values, the rms error associated with the 6 uncertain parameters is on average also reduced by 40% and 46% (compared to the worst-case rms error) for buoyancy and vorticity, respectively. It is believed that, for the most part, deterioration of the estimation performance of N^2 is linked to the effect that surface observations do not provide an appropriate sampling for its correlation with buoyancy, mainly because stability's influence on buoyancy is not local but rather extends vertically in any given column of air. For the parameter κ_η, however, the low signal of

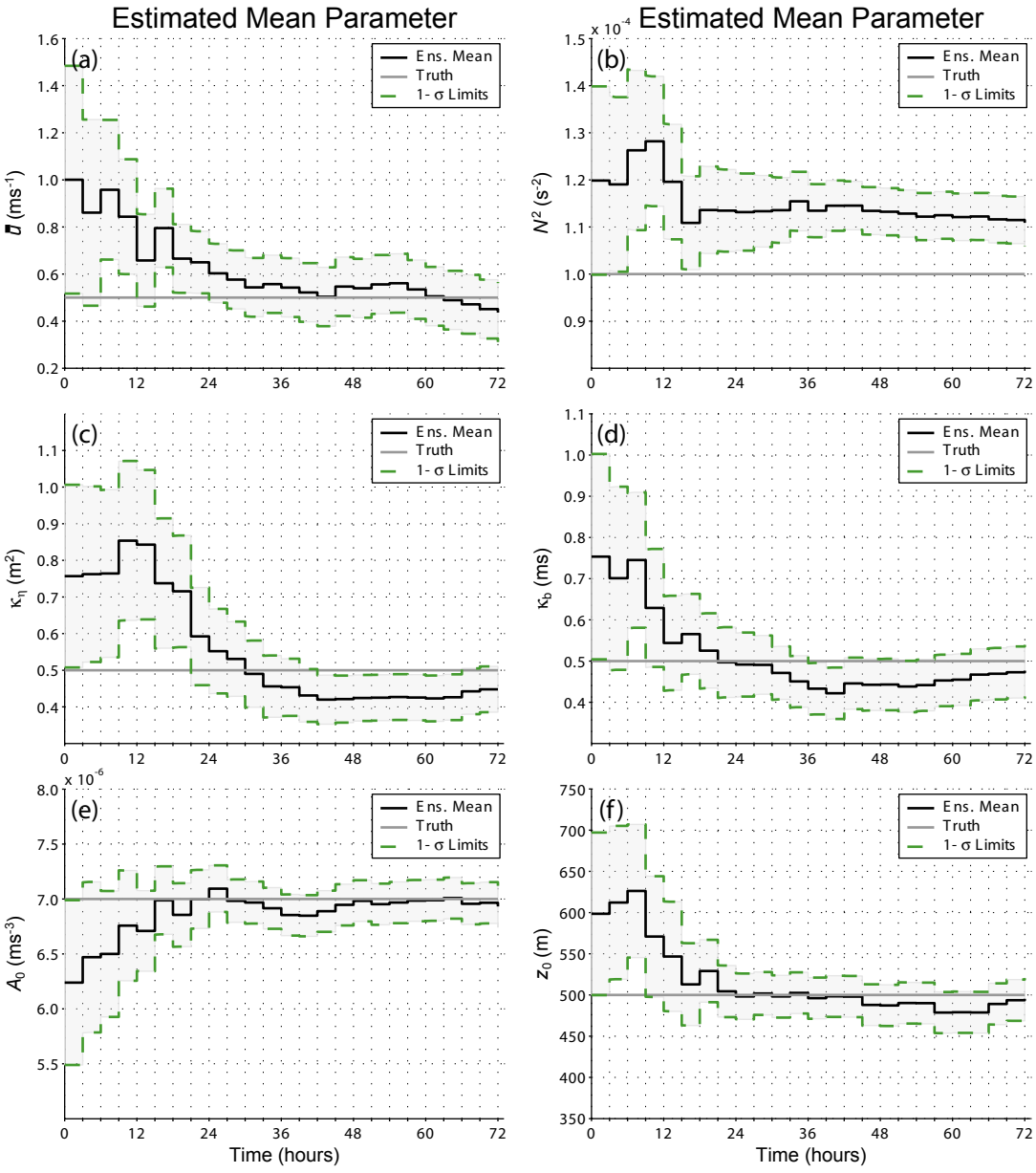

Figure 14. As in Figure 10 but for the simultaneous estimation of 6 parameters (mean horizontal wind [a], static stability [b], vertical diffusion coefficient of vorticity [c], vertical diffusion coefficient of buoyancy [d], heating amplitude [e], and heating depth [f]).

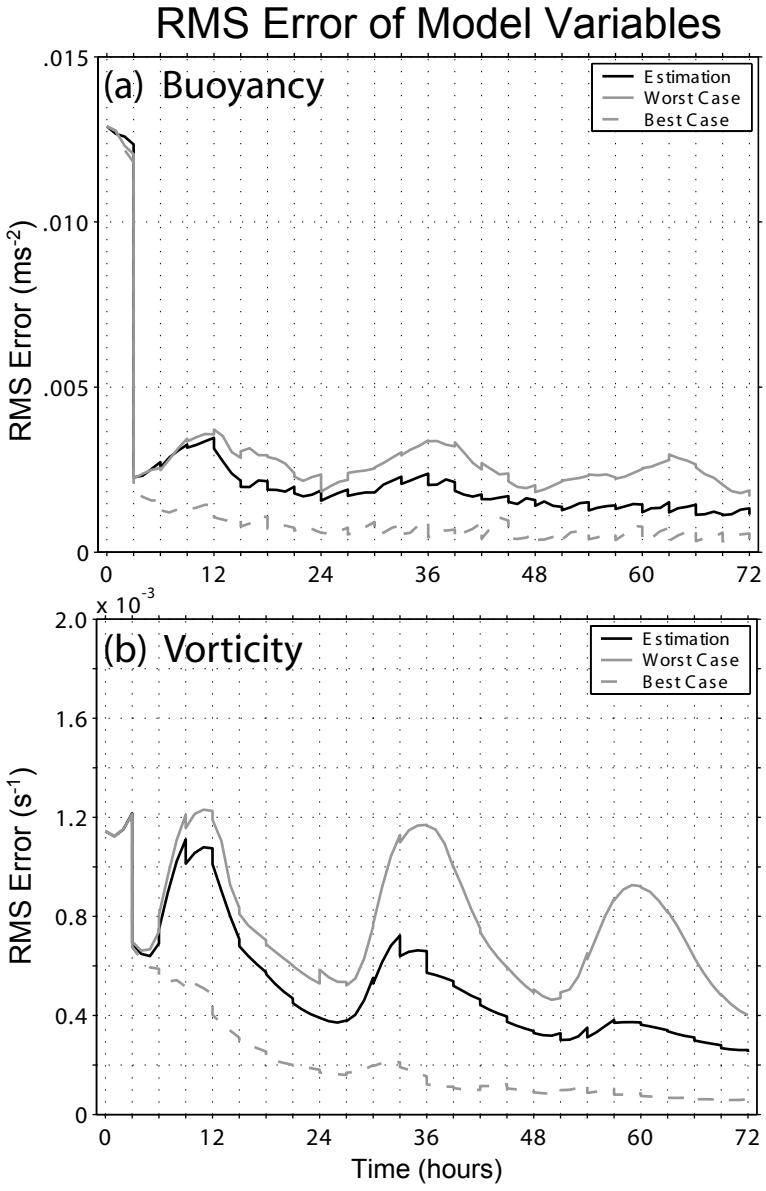

Figure 15. As in Figure 10 but for the simultaneous estimation of 6 parameters (mean horizontal wind, static stability, vertical diffusion coefficient of vorticity, vertical diffusion coefficient of buoyancy, heating amplitude, and heating depth) corresponding to Figure 14.

correlation with buoyancy is believed to be a numerical phenomenon. During the process of random perturbations, some ensemble members are occasionally assigned critically low κ_η values to force the model into a regime that it was not designed for. This divergent behavior among the ensemble members naturally causes the correlation signal between buoyancy and κ_η to be weak compared to other parameters for which the instability issue is much less critical. The nature of the behavior of the correlation between buoyancy and such poorly identified parameters is further explored in the following sections through both a more detailed investigation of the correlation itself and sensitivity analyses.

c. Parameter Identifiability

Identifiability refers to the propensity of a parameter to be estimated from given information content. With regard to parameter estimation, an important indication of identifiability is the level of absolute pointwise correlation between observed variables and parameters which is taken as an approximate measure of the relative signal-to-noise magnitude for individual parameters to be estimated. Because of the one-way dynamical interaction between model variables and parameters, a clear-cut answer to the issue of how the signal-to-noise ratio for the parameters compares to the signal-to-noise ratio for unobserved fully dynamical variables (vorticity) is not readily available. The matter is further complicated by the question of how the spatial nature of the information contained by the observed variables is related to the global characteristic of the model parameters. One metric that measures the absolute correlation and hints at an average magnitude so that the influence of spatial variability is minimized is the "rms

correlation" ($\overline{r}$) between a respective parameter and the observed variable (buoyancy) where $\overline{r}$ is computed as follows:

$$\overline{r} = \left\{ \frac{1}{M} \sum_{i=1}^{M} \left[\mathrm{cor}(\theta, b_i) \right]^2 \right\}^{1/2} . \tag{22}$$

Here, cor(θ, b_i) represents the sample correlation between the ensemble values of any (global) parameter θ and the ensemble values of buoyancy b at grid point i. The rms computation is carried out over M which denotes any collection of grid points. By definition, $\overline{r}$ values range between 0 and 1, thus representing an absolute measure of correlation between a global parameter and spatially varied buoyancy. In the analyses, $\overline{r}$ is computed for land surface or a sounding to represent the cumulative effect of observations.

Figure 16 shows the time evolution of $\overline{r}$ from pure ensemble forecasts (no state or parameter estimation is performed). In each of these experiments, one parameter is randomly perturbed about its mean value in addition to the initial state uncertainty contained in the 50-member ensemble. Each member is then integrated forward for 72 hours in pure forecast mode with the initially assigned, perturbed parameter value remaining constant in time. For each case, the average spatial influence of an observation network is compared by separately computing $\overline{r}$ for the entire domain, land surface, and a single vertical sounding located approximately 90 km inland from the coast. In the figure, the results for 4 of the 6 parameters ($\overline{u}$, N^2, κ_η, and z_0) are shown. We see that the $\overline{r}$ values appear to range between 0.1-0.6 yet there is also considerable variability within and across the parameters depending on the location of observations.

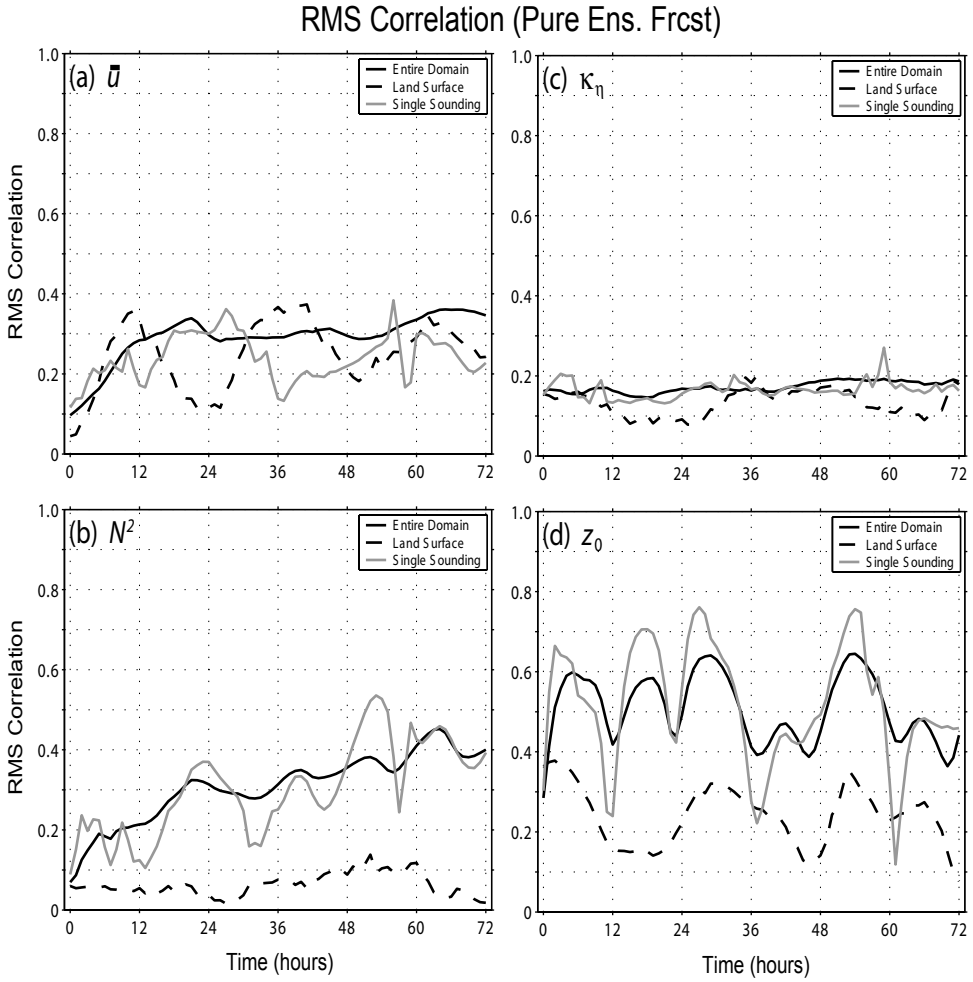

Figure 16. The time evolution of the rms correlation between a parameter and the observed variable buoyancy from pure forecast experiments with single perturbed parameter. Parameters shown are mean horizontal wind (panel a), static stability (panel b), vertical diffusion coefficient of vorticity (panel c), and heating depth (panel d). Rms correlations are computed over the entire domain (solid black), land surface (dashed black), and for a single sounding (solid gray).

In terms of absolute magnitudes, the correlation signal becomes especially low for N^2 over the land surface, while z_0 exhibits lower land surface correlations than a single sounding, although the overall level of correlation is still significantly higher for z_0 than N^2. Furthermore, the correlation signal is also considerably low for κ_η.

Overall, we see that the two parameters (N^2 and κ_η), for which the estimation performance deteriorated most dramatically as the number of simultaneously estimated parameters is increased to 6, also appear to exhibit the weakest sensitivity in terms of their rms correlations with the observed variable buoyancy. To analyze some of the potential factors that may explain the differences between the estimation performances as the number of parameters is increased, the time evolution of the land-surface $\overline{r}$ is compared between the single-parameter and 6-parameter estimation experiments (Figure 17) for the parameters $\overline{u}$, N^2, κ_η, and z_0 as a rough measure of how much the signal-to-noise ratio is affected by the increasing number of parameters. For presentation purposes, the $\overline{r}$ values at analysis steps are omitted and only the values at forecast steps are shown. The results present some hints for the differences in the identifiability of the parameters. When the time averages of the rms correlation values are computed, a small yet consistent decrease emerges from single-parameter to 6-parameter cases for all parameters (for $\overline{u}$ from 0.23 to 0.18, for N^2 from 0.18 to 0.15, for κ_η from 0.19 to 0.15, and for z_0 from 0.19 to 0.16). Such a decrease can partially be responsible for a potential loss of identifiability, especially considering the fact that the smallest 6-parameter time-averaged values coincide with the two poorly-estimated parameters N^2 and κ_η.

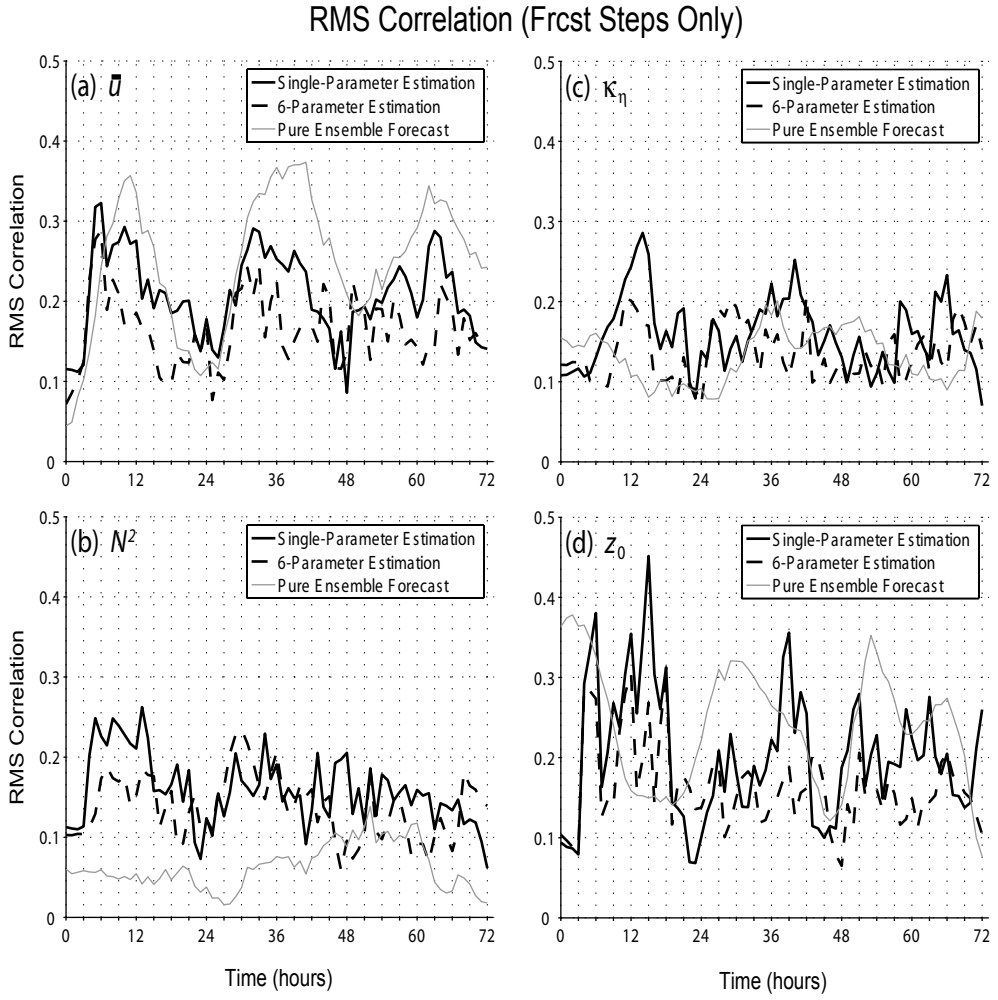

Figure 17. The time evolution of the rms correlation on land surface between a parameter and the observed variable buoyancy from single-parameter (solid black) and 6-parameter (dashed black) estimation experiments. Parameters shown are mean horizontal wind (panel a), static stability (panel b), vertical diffusion coefficient of vorticity (panel c), and heating depth (panel d). Rms correlations computed on land surface from respective pure ensemble forecast experiments are shown in solid gray for comparison.

To further test these findings, it is now attempted to isolate the effects of the two low-correlation parameters, N^2 and κ_η, in two separate experiments. In the first experiment, κ_η is excluded from the set of uncertain parameters so that only 5 parameters are estimated. As was the case for the previous experiments, here the average results from five independent experiments are presented here. The results of this 5-parameter experiment (Figure 18) produce no striking differences from the 6-parameter experiment of the previous section. Most importantly, we see that the behavior of the mean value of the critical parameter N^2 does not change significantly and, similar to the 6-parameter case, the true value stays outside the 1-σ interval at all times, although the convergence between the true and estimated mean values is more persistent than the 6-parameter counterpart. Similarly, there are also no significant differences apparent in the behavior of the other parameters. As a result, the rms error performance of the 5-parameter experiment (Figure 19) does not exhibit noticeable differences compared to the 6-parameter experiment. The MRE values for buoyancy and vorticity are 67% (higher than the 6-parameter experiment) and 47% (lower than the 6-parameter experiment), respectively. Thus, although being a critical parameter by itself, κ_η has limited influence on the overall identifiability of other parameters when more critical parameters dominate the error evolution in the system.

As another test on identifiability, all 6 parameters are again made uncertain but a 3-hourly single sounding observation is simulated (vertically-sampled buoyancy with 250-m spacing) located 90-km inland instead of the land surface observations with 40-km spacing. The previous experiments revealed that, especially for N^2

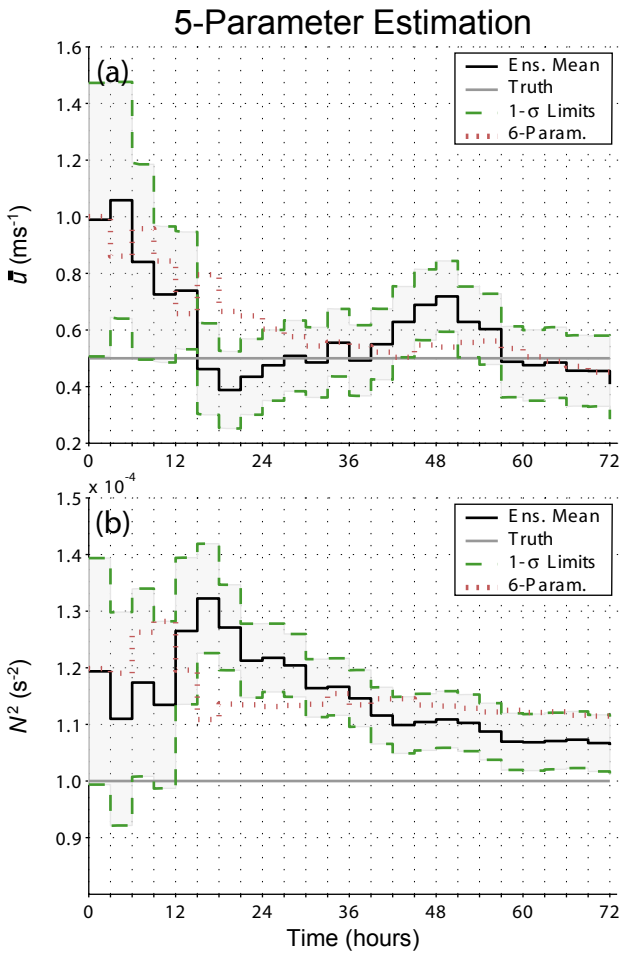

Figure 18. The time evolution of the mean parameter values (solid black) from the 5-parameter estimation results with a perfect vertical diffusion coefficient of vorticity. The control experiment (6 simultaneous parameters) is shown with gray dotted line for comparison. Parameters shown are mean horizontal wind (panel a) and static stability (panel b).

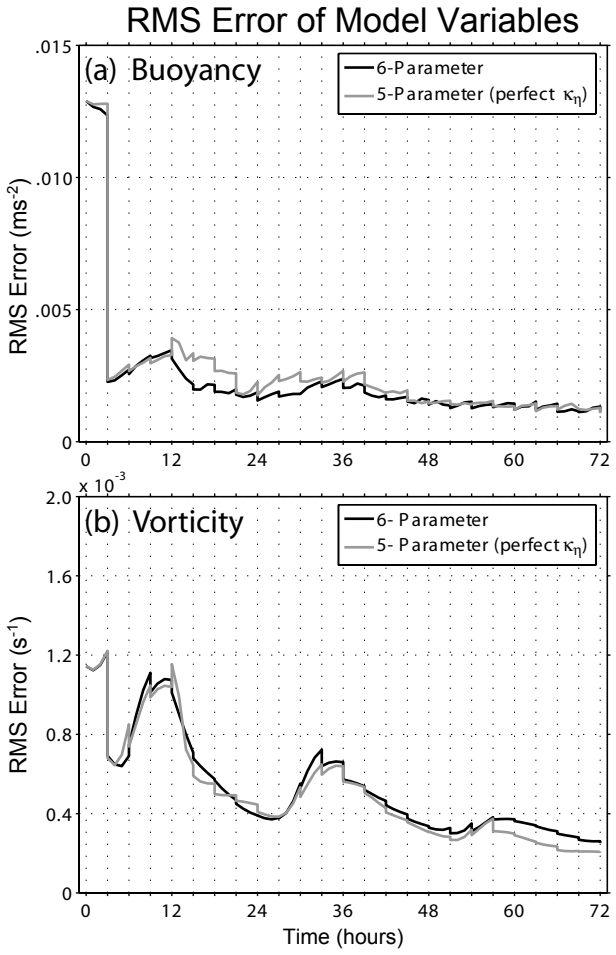

Figure 19. The time evolution of the rms error (solid black) of buoyancyt(op panel) and vorticity (bottom panel) from the 5-parameter estimation results with a perfect vertical diffusion coefficient of vorticity. The control experiment (6-parameter estimation) is shown in solid gray for comparison.

(Figure 16b and Figure 17b), the overall level of correlation with the observed variable buoyancy is very sensitive to the location of observations. As was determined in Chapter II, the state estimation itself is not very sensitive to a sounding observation as opposed to land surface observations, so that any significant difference in filter performance can be confidently interpreted as a contribution from the parameter estimation part, exclusively. The behavior of the mean parameter values (Figure 20) indicates interesting differences from the 6-parameter experiment with land surface observations. To begin with, consistent with its stronger sounding correlations, there is an improvement in the evolution of the mean value of N^2. On the other hand, some deterioration in the mean value of $\overline{u}$ is also evident while κ_η continues to exhibit a relatively weak performance. The cumulative consequence of these individual parameters is that no significant change is observed in the rms error of the model variables (Figure 21). While there is a slight decrease of the buoyancy MRE to 56%, compared to the 6-parameter experiment with land surface observations, the vorticity MRE increases to 62%. Thus, in general, the sounding observations, as applied to the estimation of all 6 parameters, do not lead to a qualitative improvement in the overall performance of the filter. Although, on one hand, the improved estimation of N^2 contributes positively to the error reduction, the slightly worsened performance of $\overline{u}$ apparently counterbalances this improvement. On the other hand, different parameters respond to the spatial configuration of observations differently. Thus, in principle, a data assimilation system could be optimized to take advantage of such differences in the spatial information content of observations.

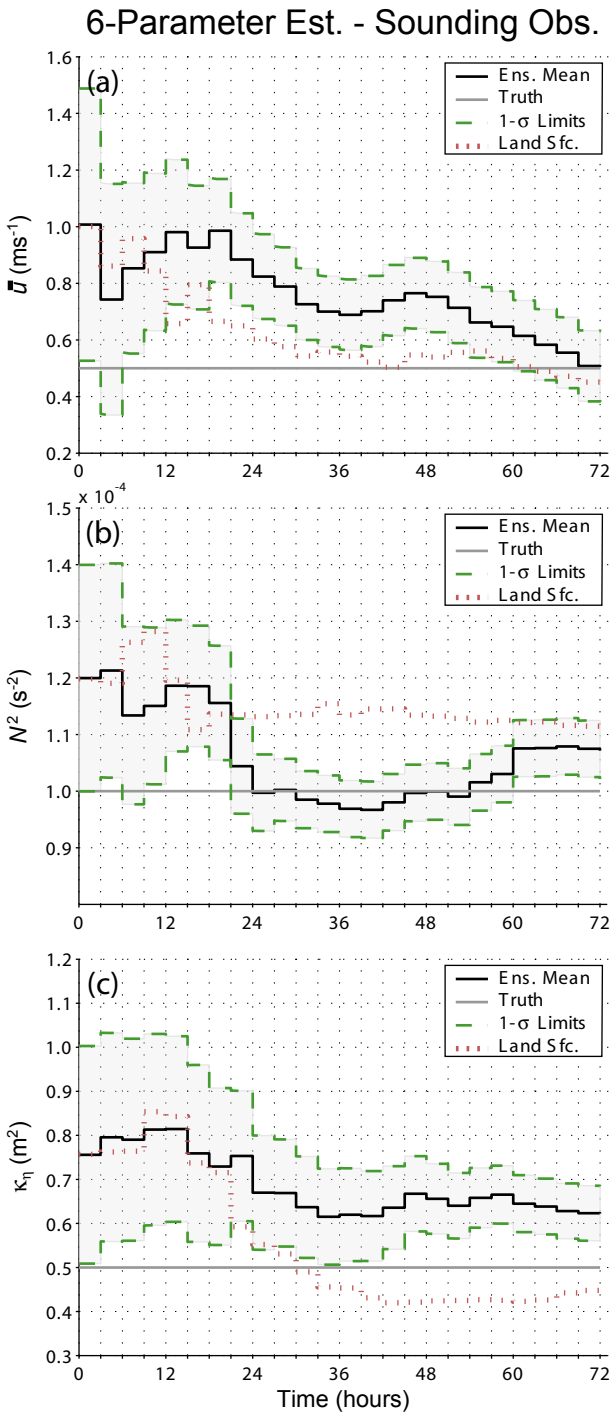

Figure 20. The time evolution of the mean parameter values (solid black) from the 6-parameter estimation results with 3-hourly single sounding observations. The control experiment (land surface observations) is shown with red dotted line for comparison. Parameters shown are mean horizontal wind (panel a), static stability (panel b), and vertical diffusion coefficient of vorticity (panel c).

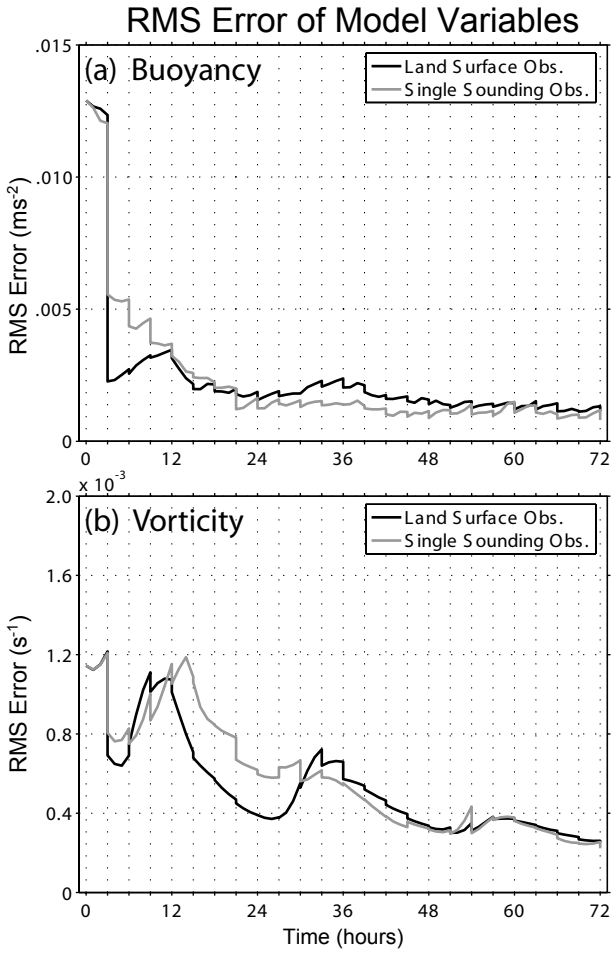

Figure 21. The time evolution of the rms error (solid black) of buoyancy (top panel) and vorticity (bottom panel) from the 6-parameter estimation results with 3-hourly single sounding observations. The control experiment (land surface observations) is shown in solid gray for comparison.

d. Sensitivity of Parameter Estimation to Filter Configuration

The attention is finally turned to how the filter configuration influences the performance of the parameter estimation. Filter configuration encompasses some of the numerical attributes that control the available information content and thus the identifiability of the parameters. As was the case for the previous experiments, here too, the average results from five independent experiments are reported.

One of the most critical filter parameters in terms of its influence on parameter identifiability is believed to be the ensemble size. In addition to the control experiments with 50 members, additional 6-parameter sensitivity experiments are performed with 20 and 100 members and the results are summarized in Figure 22 (mean estimated parameter values of 3 noteworthy parameters $\overline{u}$, N^2, and κ_η) and Figure 23a and b (evolution of the rms error of model variables). As anticipated, we see that the estimated mean parameter values exhibit a considerable sensitivity to ensemble size, especially the parameters N^2 and κ_η. This is believed to be mainly due to the deteriorated sampling quality that becomes critical for the two parameters N^2 and κ_η that exhibited the lowest overall level of correlation to buoyancy (on land surface) in the pure-forecast experiments (Figure 16b, c). As a result, the mean values of N^2 and κ_η become non-responsive to the estimation attempt and meander about their initial value. Furthermore, although the estimated mean value of $\overline{u}$ converges toward its true value, we see that it exhibits a much more pronounced variability as a direct consequence of the deteriorated sampling quality associated with smaller ensemble size. At the higher ensemble size of 100 members, the improvement in the estimation performance is not as dramatic

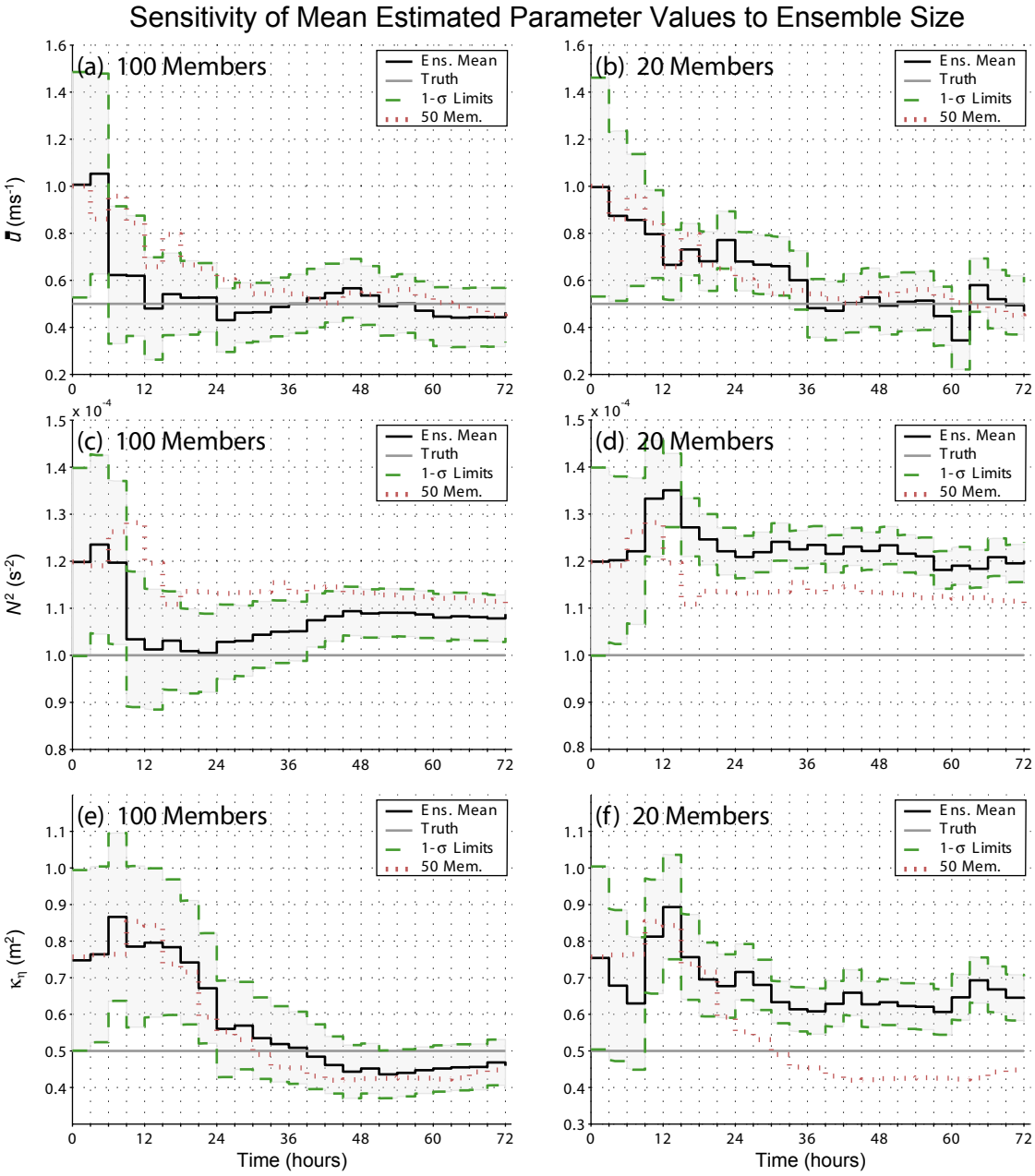

Figure 22. Sensitivity of the evolution of mean parameter values to ensemble size. Left panels are from 100-member experiments while right panels are from 20-member experiments. The control experiment (50 members) is shown with red dotted line for comparison. Parameters shown are mean horizontal wind (panels a, b), static stability (panels c, d), and vertical diffusion coefficient of vorticity (panel e, f).

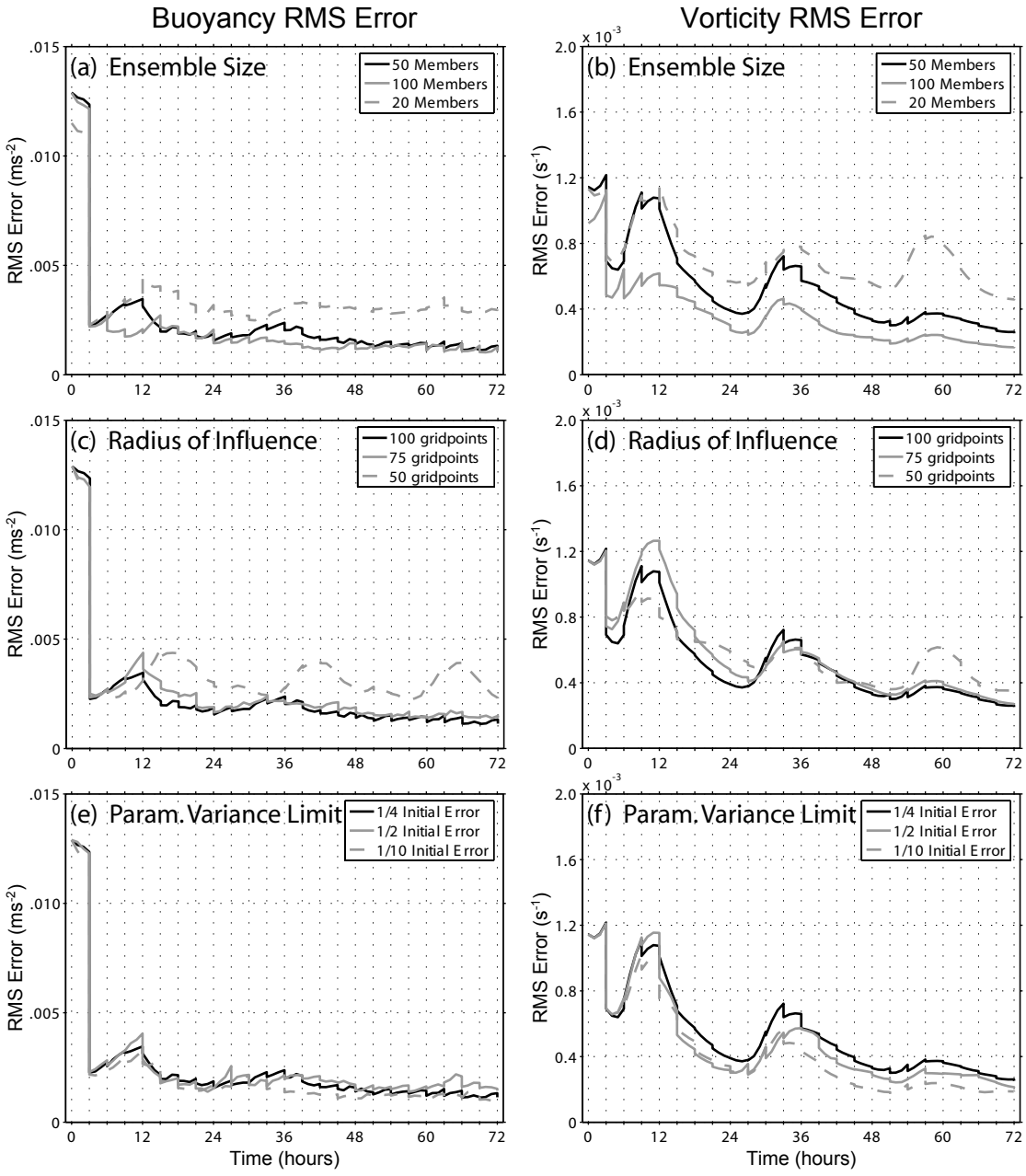

Figure 23. Comparison of the evolution of rms error of buoyancy (left panels) and vorticity (right panels) from the sensitivity experiments for ensemble size (top panels), radius of influence (middle panels), and parameter variance limit (bottom panels). For each case, the two sensitivity experiments are shown in solid gray and dashed gray while the control experiment is shown in solid black.

compared to the differences between 50 and 20 members, although especially N^2 appears to be positively influenced by the increased sampling quality. Meanwhile, the differences in the performance of individual parameters as a result of the varied ensemble size are also reflected proportionally in the rms error of the model variables. We see that both buoyancy and vorticity error increase dramatically for the 20-member case while with 100 members, the decrease in the buoyancy error is much less distinct compared to the vorticity error.

Another filter parameter that is tested for sensitivity is the radius of influence. In the control experiments, the radius of influence is kept at a large 100 grid points to minimize the effects of localization. For sensitivity purposes, experiments with progressively smaller values of 75 and 50 grid points are performed and the results are summarized in Figure 24 (mean estimated parameter values of 3 noteworthy parameters N^2, κ_b, and z_0) and Figure 23c and d (evolution of the rms error of model variables). In general, a distinct decrease in estimation quality is observed as the radius of influence is reduced. However, the response of individual parameters to the reduction in the radius of influence varies across parameters. For instance, the estimation of N^2, which is generally found to be one of the most critical parameters to estimate, appears to improve with decreasing radius of influence. On the other hand, parameters κ_b and z_0, that normally do not exhibit critical identifiability, become non-responsive to the estimation attempt. Such differences in the behavior of the parameters further reinforce the conviction that the complicated relationship between global parameters and spatial observations plays an intricate and critical role in determining the identifiability of each

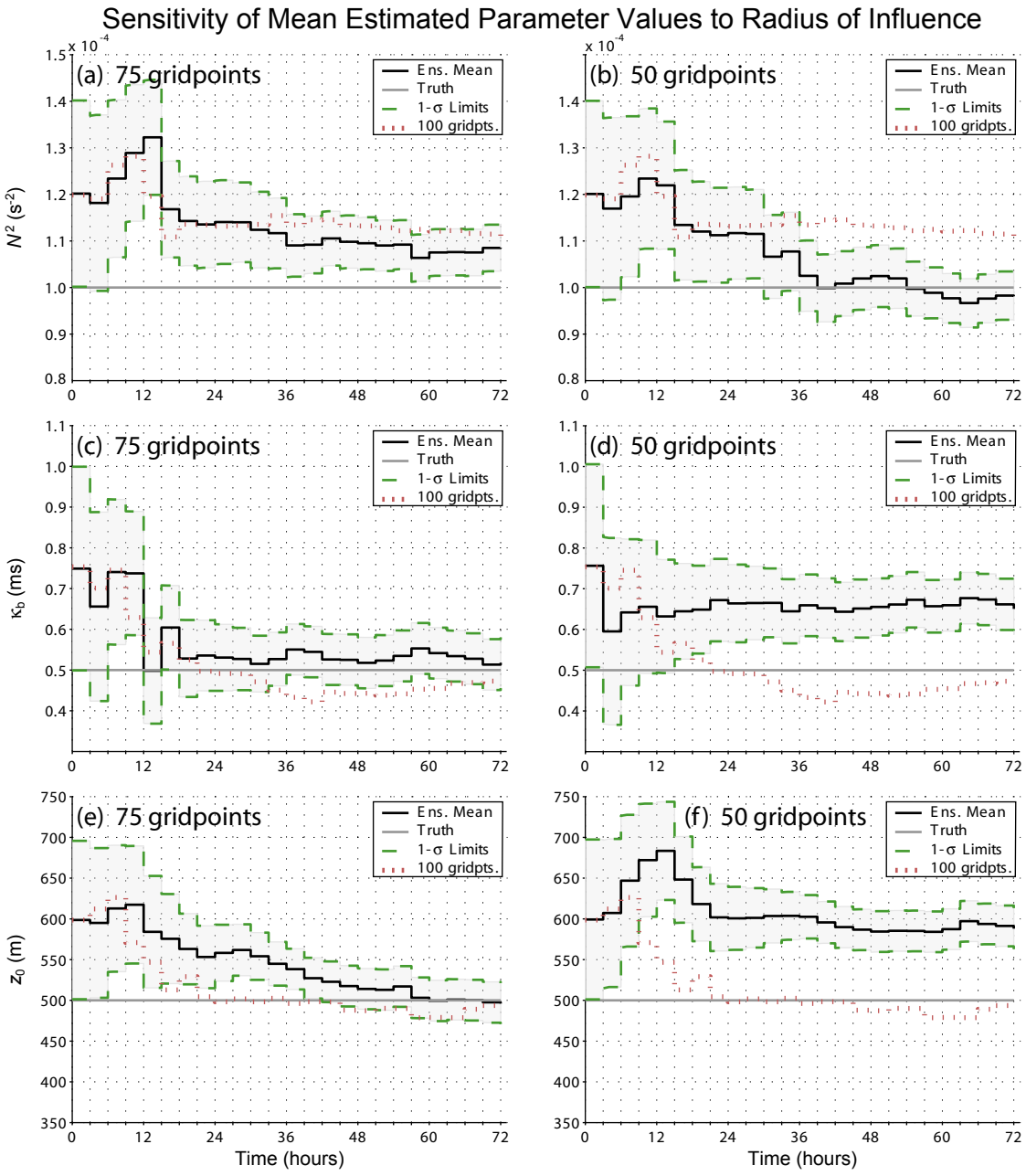

Figure 24. Sensitivity of the evolution of mean parameter values to radius of influence. Left panels are from 75-gridpoint experiments while right panels are from 50-gridpoint experiments. The control experiment (100 grid points) is shown with red dotted line for comparison. Parameters shown are mean horizontal wind (panels a, b), static stability (panels c, d), and vertical diffusion coefficient of vorticity (panel e, f).

parameter. As was the case with the difference between surface-based and sounding observations, a non-global, parameter-specific strategy in the application of localization could be necessary to optimize the estimation process and ensure identifiability.

Finally, the sensitivity of the parameter estimation to the limit applied to parameter variances is also briefly discussed. Obviously, the variance treatment method that is employed is ad hoc in nature and, therefore, the findings are not as generalizable in terms of identifiability as other filter characteristics such as ensemble size or radius of influence. However, it is also believed that the relatively straightforward application of the method does enable one to establish some links between the acceptable variability of a given parameter and how that may be accounted for in an estimation system. For sensitivity purposes, in addition to the control experiments with a global variance limit that is 1/4 of the initial error for each parameter, experiments with a larger limit of 1/2 and smaller limit of 1/10 of the initial error are performed and the results are summarized in Figure 25 (mean estimated parameter values of 3 noteworthy parameters $\overline{u}$, N^2, and κ_η) and Figure 23e and f (evolution of the rms error of model variables). Similar to previous sensitivity experiments, we see varying results for different parameters. While $\overline{u}$ and κ_η respond positively to the smaller variance limit, the estimation of N^2 is clearly improved (compared to the control experiment) when a larger variance limit is applied (although, while its estimation is also better than the control experiment for the smaller variance limit in absolute terms, its mean estimated value still drifts outside the acceptable limits after about 36 hours, hinting at filter divergence).

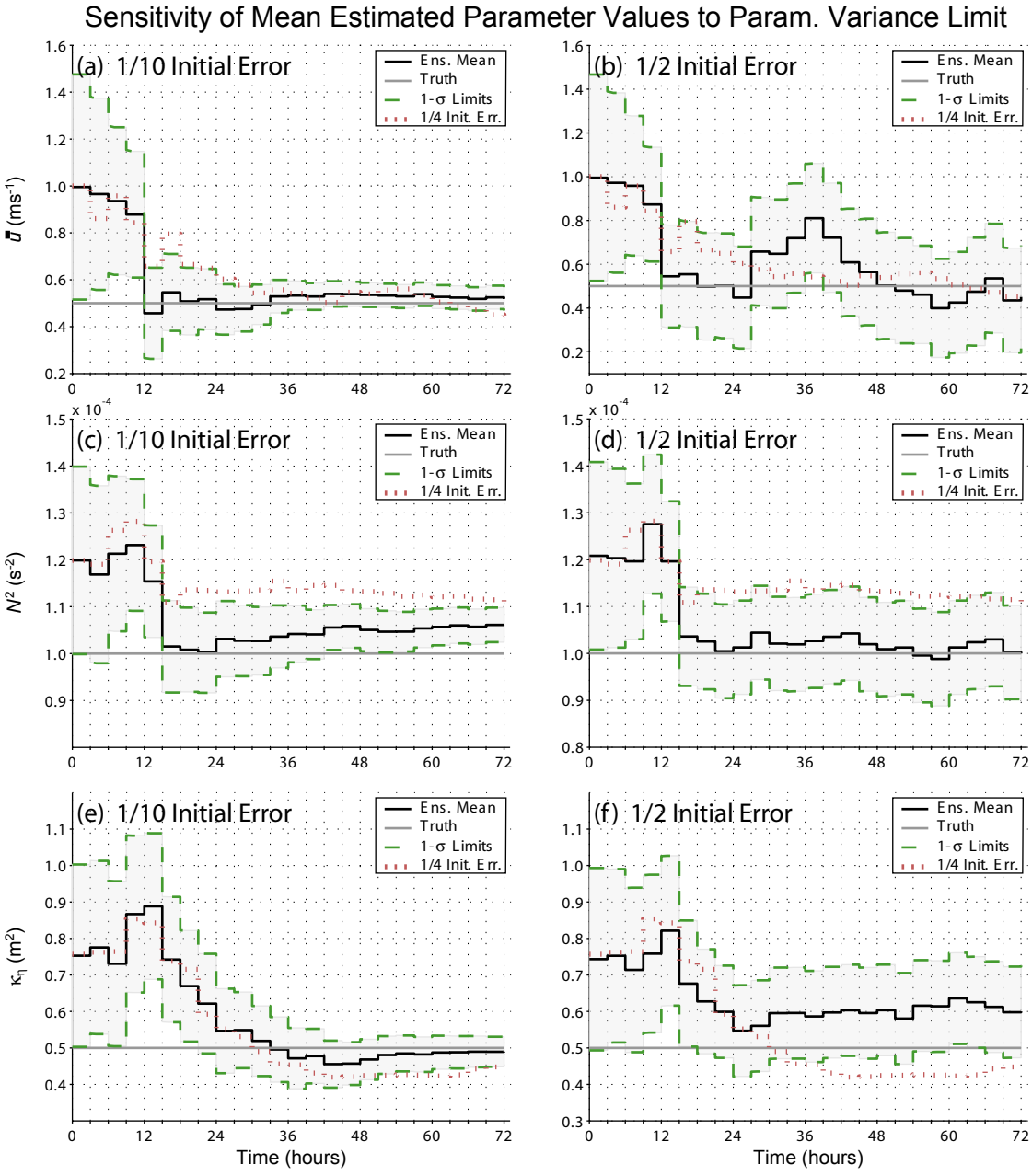

Figure 25. Sensitivity of the evolution of mean parameter values to parameter variance limit. Left panels are from 1/10 initial error experiments while right panels are from 1/2 initial error experiments. The control experiment (1/4 initial error) is shown with red dotted line for comparison. Parameters shown are mean horizontal wind (panels a, b), static stability (panels c, d), and vertical diffusion coefficient of vorticity (panel e, f).

From an rms error point of view, however, we see that, despite the positive contribution from N^2, the larger variance limit does not consistently reduce the rms error of model variables (on average, there is ~4% increase in buoyancy error as opposed to a ~10% decrease in vorticity error). Conversely, the smaller variance limit produces a 9% and 20% decrease in buoyancy and vorticity errors, respectively. In general, the overall estimation process benefits more from the smaller variance limit of 1/10 of the initial parameter error. Yet there is also a distinct difference in response among the 6 parameters tested and consistency in the success of parameter estimation will necessarily depend on prior knowledge of the acceptable variability of each parameter estimated and the ability to devise an estimation scheme that takes maximum advantage of this knowledge.

EVALUATION OF ENSEMBLE-BASED PARAMETER ESTIMATION FOR A NUMERICAL MODEL OF OPERATIONAL COMPLEXITY

1. Experimental Design

a. The Forecast Model

Having documented in previous chapters the effectiveness of the EnKF for the application to simultaneous state and parameter estimation in a proof-of-concept setting and for a dynamical model of intermediate complexity, this section aims to lay the groundwork for the investigation of the subject for operational numerical modeling environments. For this purpose, the Pennsylvania State University-National Center for Atmospheric Research (Penn State-NCAR) fifth-generation nonhydrostatic mesoscale model (MM5; Dudhia 1993) is used to represent the numerical and implementation complexities associated with an operational forecasting system. Since the introduction of its first hydrostatic version as a publicly accesible research tool (Anthes and Warner 1978), this model has been widely accepted and used in the atmospheric science community for a variety of numerical modeling purposes.

As the dynamical focus of the numerical simulations is on the thermally-forced sea breeze circulation, the model domain is chosen such that it covers mostly the Southcentral United Stated and the northern half of Gulf of Mexico (Figure 26) where such local circulations are very prominent during summer months. Horizontally, it has

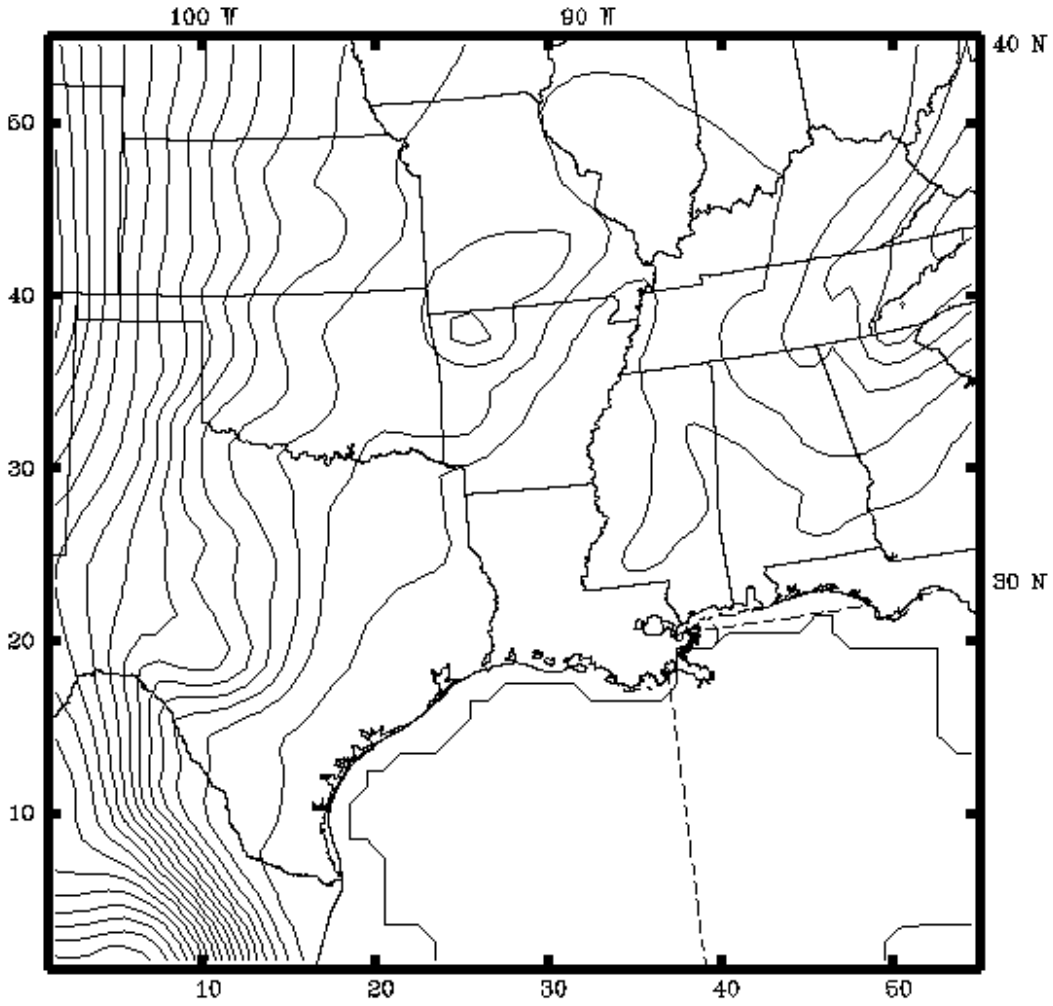

Figure 26. Map of the MM5 model domain. Terrain heights plotted with solid contours (100m spacing).

55×55 grid points with 36 km grid spacing. There are 43 layers in the terrain-following vertical coordinate with the model top at 50 hPa (approximately 20 km) and vertical spacing smallest within the boundary layer. For the parameterization of the planetary boundary layer (PBL), the Medium Range Forecast model (MRF) scheme (Hong and Pan 1996) is used in all of the simulations, the details of which are given in section d. For the cumulus parameterization, the Grell scheme (Grell 1993) is used with the shallow cumulus option turned on for the handling of nonprecipitating clouds, while for the parameterization of microphysical processes, a simple ice scheme is chosen that contains ice processes above the freezing level yet adds no memory for any of the ice species. The model has a total of 6 prognostic variables including the Cartesian velocity components (u, v, w), pressure perturbation (p'), temperature (T), and the mixing ratio for water vapor (q). The simple ice scheme defines and utilizes the mixing ratios for cloud water (q_c), and rain water (q_r) during model integration but these two variables are not saved in the final model output.

b. Ensemble Initialization and Treatment of Lateral Boundaries

All MM5 forecasts are performed in an ensemble setting with 40 members. A 41st member is generated with the same ensemble statistics and used as the "truth simulation". The control period for the experiments is chosen as 28-31 August 2000 which coincides with an ozone pollution period experienced in Houston, Texas during the Texas 2000 Air Quality Study (TexAQS-2000) which was a major field program that ran from 15 August to 15 September 2000 with the goal of understanding the formation

and transport of ozone and particulate matter in eastern Texas, particularly around Houston.

To reflect the climatological variability of the state of the atmosphere during the summer months, a "climatological ensemble initialization" method is devised that is similar to the initialization technique used for the two-dimensional sea breeze model (described on p. 35). The major steps involved are: (i) To represent the summer-time climatological statistics, a data set for the period of 1 June – 15 September 2000 is generated from the Global Energy and Water Cycle Experiment (GEWEX) Continental-Scale International Project (GCIP) data which consist of the Eta model's 3-hourly gridded (40-km nominal horizontal resolution and 25 constant-pressure surfaces between 1000 hPa and 25 hPa) 3-dimensional and 2-dimensional analysis fields. One advantage of using this dataset for the initialization is the fact that there is little inconsistency between the horizontal model resolution employed for the experiments and the nominal horizontal resolution of the dataset. This minimizes the errors associated with lateral boundaries and ensures that the interior domain does not become contaminated by the advection of errors from the lateral boundaries during model integration. (ii) Ensemble member initial conditions were randomly selected from this climatological data set. Similarly, boundary conditions for each ensemble member were generated as the data of the same length as the control period but beginning with the randomly selected initial time of the corresponding member. (iii) Deviations of the initial and boundary condition data for each member from the climatological mean for the entire period is then rescaled

down to 20% (see Fig. 6.5.6 of Kalnay 2003) to adjust for the fact that climatological variability is usually much larger than model spread.

c. State Estimation for MM5

In general, the characteristics of the EnKF used for the analysis of MM5 state data is very similar to the filter that is designed for the two-dimensional sea breeze model. Specifically, an ensemble square-root filter after Whitaker and Hamill (2002) is used with sequential updating of observations. Sounding and surface observations of u, v, and T are simulated from the truth simulation with observational errors of 1 ms^{-1} for u and v and 0.5 K for T. To mimic the operational observational spacing for the continental United States, a 324 km (9 grid points) horizontal spacing between sounding observations is chosen while the surface observation spacing is set at 72 km (2 grid points). The assimilation of both sounding and surface simulated observation data is performed every 12 hours starting with the 12-hour forecast (thus, in total, 6 assimilation cycles were performed in the 72-hour forecast period). Finally, localization of observations is achieved by utilizing Gaspari and Cohn's (1999) compactly supported fifth-order correlation function with a radius of influence of 30 grid points both horizontally and vertically.

d. Parameter Estimation for MM5

<u>The MRF PBL scheme and the vertical diffusion coefficient multiplier</u>

The MRF PBL parameterization scheme is a nonlocal turbulence scheme described by Hong and Pan (1996). This scheme differentiates between vertical diffusion in the mixed layer and the free atmosphere. In the mixed layer the scheme

assumes that thermals and eddies of boundary-layer scale transport heat and other properties according to bulk gradients which may be much different than local-scale gradients (Troen and Mahrt 1986). The simplest way to account for this nonlocality is to incorporate a countergradient term, γ_c, to the local form of the flux equation for c, where c represents any vertically transported quantity by diffusion:

$$\frac{\partial c}{\partial t} = \frac{\partial}{\partial z}\left[K_c \left(\frac{\partial c}{\partial z} - \gamma_c \right) \right]. \tag{23}$$

Here, w and K_c are the vertical wind component and the eddy diffusivity coefficient, respectively. The prime denotes a perturbation quantity while the overbar symbolizes Reynolds averaging. The magnitude of the countergradient term, γ_c, is given by

$$\gamma_c = b \frac{\overline{w'c'}}{w_s}, \tag{24}$$

where b is a proportionality constant, and $w_s = u_* \phi_m^{-1}$ is the mixed-layer velocity scale and depends on the surface frictional velocity, u_*, and the wind profile function, ϕ_m^{-1}, which depends on the stability properties of the mixed layer and the boundary layer height, h. Meanwhile, free-atmosphere diffusion above the mixed layer is resolved by a local diffusion scheme proposed by Louis (1979).

Parameter estimation computations for this study are based on the global uncertainty of the eddy mixing coefficient. In order to represent a global uncertainty in the value of this parameter without individually incorporating the effects of many other parameters that influence its value, the MRF PBL code is modified such that the final K_c value determined within the code is multiplied by an externally-defined multiplier, m_c,

before the implicit computation of the vertical diffusion is performed. Thus, for m_c = 1.0, the original MRF PBL computation is simply repeated. Varying the values of m_c generates an uncertainty in the overall magnitude of K_c without having to explain the underlying causes that might have led to such variability. As the resulting variability exhibits a global influence on vertical diffusion, it also has a better physical justification compared to the numerous empirical parameters, influences of which on K_c may appear to be more numerical than physical.

In the numerical experiments described in this study, the parameter that is subject to estimation is thus the vertical diffusion coefficient multiplier, m_c. To represent initial uncertainty in the parameter value, a standard deviation of ~0.3 is chosen as the initial ensemble spread.

Spatial updating of a global model parameter

Although m_c is treated as a global parameter during model integration, its scalar nature represents a rank inconsistency during an assimilation step because of the much higher dimension associated with the observational vector (~10^3). This is a much more serious problem compared to the two-dimensional model (where the observational vector has a dimension on the order of 10^1) and preliminary tests with various configurations of the filter involving the updating of the scalar form of m_c produced inadequate filter performance (results not shown). Because of this reason, a new method is devised that calls for the transformation of the prior m_c from a scalar into a two-dimensional vector defined at the surface with the same prior value at every grid point. The updating of the parameter is then performed spatially using Gaspari and Cohn's

(1999) compactly supported fifth-order correlation function. Once the updating is completed, spatial averaging is performed to obtain the updated global value for m_c (for each ensemble member) which is then fed into the subsequent forecast cycle.

Sensitivity experiments (not shown) revealed that the optimal values for both horizontal and vertical radii of influence are very similar to the radii of influence used for the updating of the state. Furthermore, the spatial distribution of the updated parameter exhibited consistent structure over many random trials (not shown) suggesting that the observations contained meaningful spatial correlation signal with m_c, justifying the proposed technique. Consequently, all of the results presented in this work are based on the spatial updating of global parameters where observation localization with a radius of influence of 30 grid points is used horizontally and vertically (same as the updating of the state).

2. Results

a. The Perfect-Model Control Ensemble Forecast

To begin, a brief overview of the 72-hour control ensemble forecast, initialized at 00Z 28 August 2000 (7pm CST which is nearly the peak sea breeze phase) and performed with perfect-model statistics, will be presented in this section. With the chosen relatively large domain and resolution, the diurnal signal within the PBL arises both from to the sea breeze circulation and the Great Plains low level jet. To illustrate the diurnal signal embedded in the large-scale flow, the horizontal distributions of (ensemble mean) u, v, T, and q are plotted for 24-hour, 30-hour, 36-hour, and 42-hour

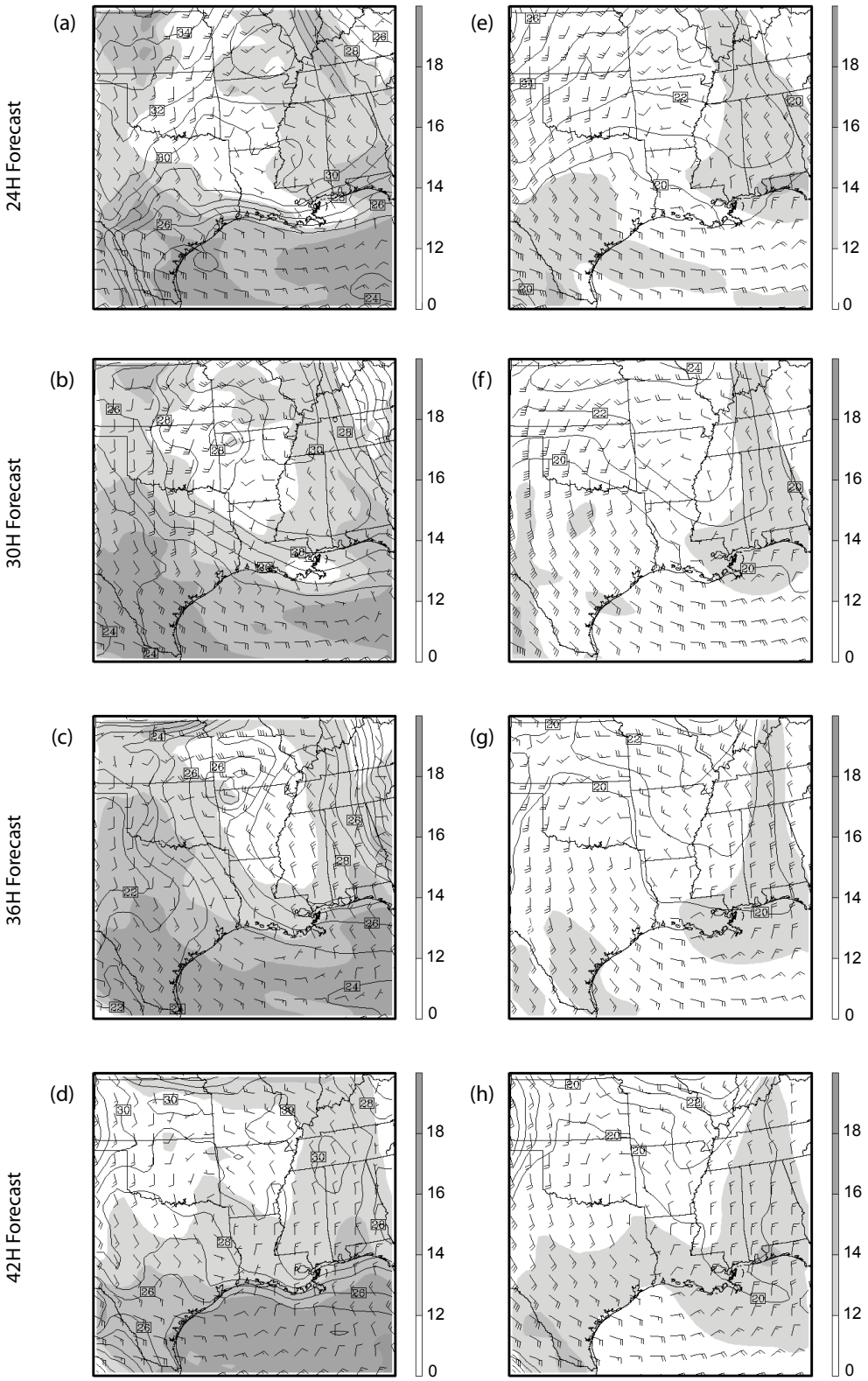

Figure 27. Perfect-model forecast distributions of horizontal wind (full barbs 5 ms^{-1}), T (contours with interval of 1.0°C) and q (shading with interval of 4 gkg^{-1}) at forecast times 24 hours (a, e), 30 hours (b, f), 36 hours (c, g), and 42 hours (d, h) at heights 0.5 km (left panels) and 1.5 km (right panels).

forecast times at heights 0.5 km and 1.5 km (Figure 27). A persistent anti-cyclonic circulation centered around Louisiana is evident at all forecast times and both heights. Nevertheless, the impacts of the local circulation are discernible especially across the coastline between East Texas to Louisiana and at the height of 0.5 km. At 24 hours (Figure 27a), which is nearly the peak sea breeze phase, 0.5-km winds are southeasterly with sharp temperature and moisture gradients situated over the coast or slightly inland. Within 6 hours (30-hour forecast, Figure 27b), the 0.5-km winds veer to the right and become almost southerly while both the temperature and moisture gradients penetrate further inland and weaken at the same height. By 36 hours (Figure 27c), a northerly return flow associated with the land breeze establishes itself just inland from the coast which then strengthens and penetrates southward at 42 hours (Figure 27d). By this time, the 0.5-km temperature and moisture gradients become stronger and penetrate back south to be again situated along the coastline. Meanwhile, at the height of 1.5 km, the diurnal variability is much less dramatic and the larger-scale anti-cyclonic circulation around the high pressure center remains almost intact during the entire period (Figure 27e-f). It should also be noted that the described diurnal signal at 0.5 km is relatively weak compared to the larger-scale circulation and only modifies it in the immediate vicinity of the coastline. During the third day of the simulation, the high pressure area strengthens even further and suppresses the sea breeze circulation almost completely (not shown).

The comparison of the control ensemble forecast to the truth simulation is carried out by plotting the difference fields of the same variables as in Figure 27 (u, v, T, and q)

in terms of differences of the ensemble mean and the truth at the same forecast times (24, 30, 36, and 42 hours) and heights (0.5 km and 1.5 km). The results of this comparison is shown in Figure 28. As a direct consequence of the weak diurnal signal associated with the sea breeze circulation, the difference field, in general, is dominated by the errors associated with the large-scale flow. This is especially evident in the 1.5-km fields (Figure 28e-f) which show most of the errors concentrated along a frontal boundary that propagates southwestward across the western half of Gulf of Mexico. Meanwhile, the 0.5-km differences are much smaller and contain almost no evidence of the local sea breeze circulation, which is an indication that largest uncertainties in the meteorological prediction arise from the large-scale circulations and their associated frontal systems while the sea breeze circulation is more predictable and does not contribute to the uncertainty significantly.

The evolution of the forecast error growth revealed from the difference between the truth simulation and the reference ensemble forecast mean can be best summarized in terms of difference total energy (DTE):

$$\mathrm{DTE} = \frac{1}{2}\left(u'^2 + v'^2 + kT'^2\right), \tag{25}$$

where primes denote the difference between any two simulations and $k=C_p/T_r$ (C_p=1004.7 $\mathrm{Jkg^{-1}K^{-1}}$ and the reference temperature T_r = 270K). The horizontal distribution of the (vertically-averaged) root-mean (RM) of DTE (RM_DTE) at 24, 30, 36, and 42 hour forecast times are displayed in Figure 29a-d. Consistent with the

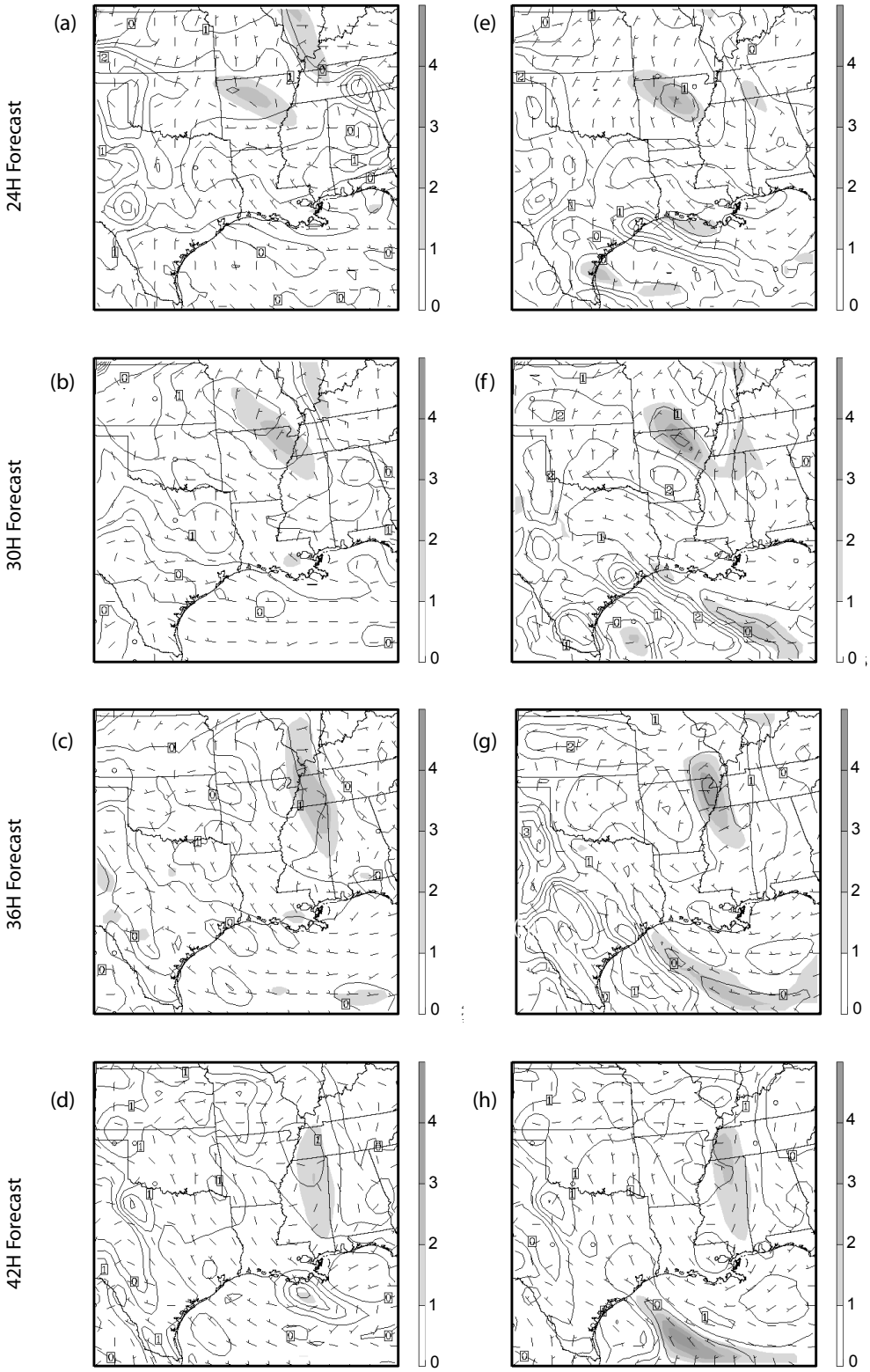

Figure 28. As in Figure 27 but for the differences between the control forecast and the truth. Contour intervals are 0.5°C for T and 1 gkg^{-1} for q.

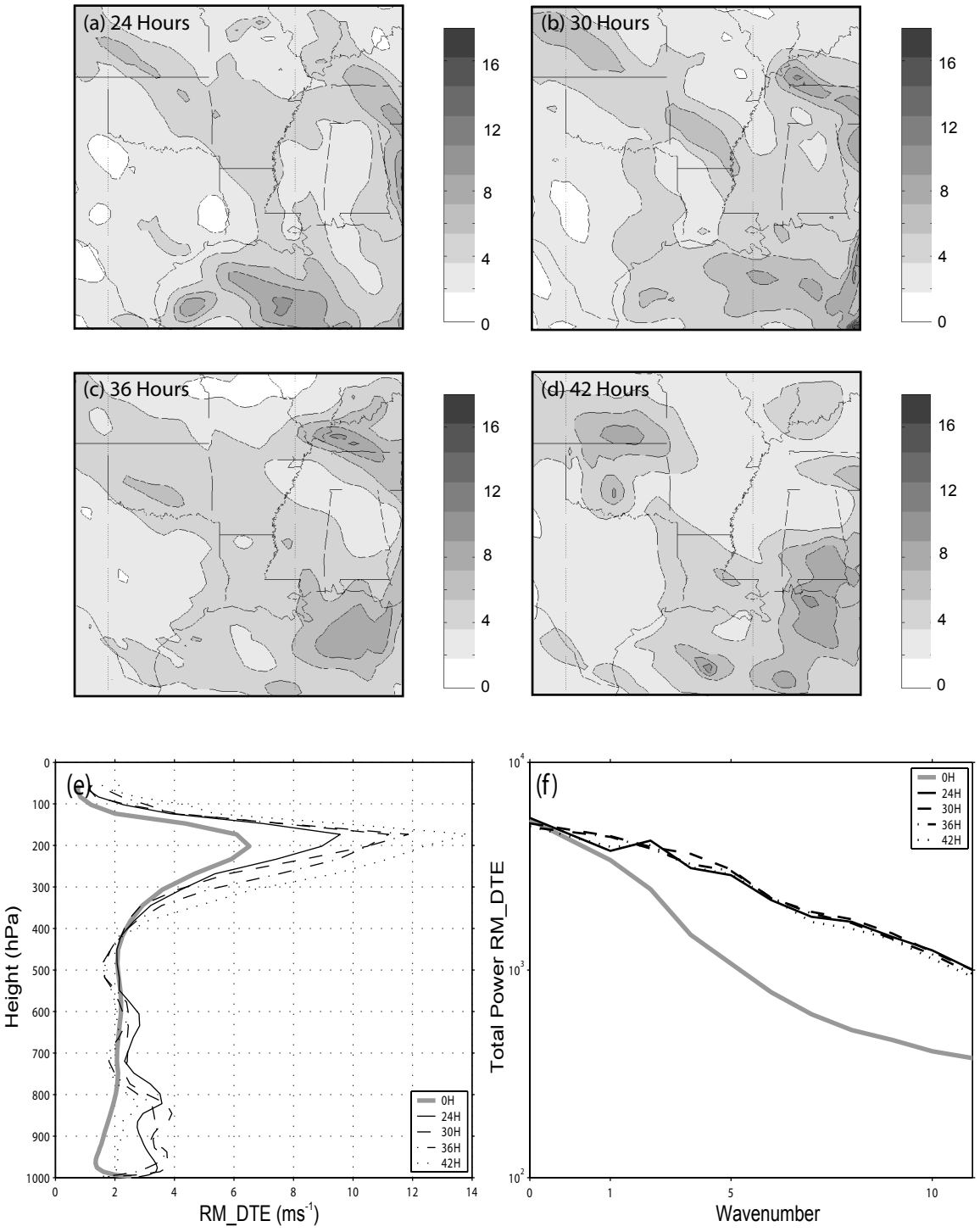

Figure 29. The horizontal distribution of RM_DTE (ms^{-1}) at forecast times 24 hours (a), 30 hours (b), 36 hours (c), and 42 hours (d). Panel (e): The vertical profile of RM_DTE for times 0 hours (solid gray), 24 hours (solid black), 30 hours (dashed black), 36 hours (dashed-dotted black), and 42 hours (dotted black). Panel (f): The total power spectrum of RM_DTE for the same times as (e). Wavenumber 1 corresponds to a wavelength of 1800 km while wavenumber 12 approximately corresponds to the double Nyquist wavelength of 72 km.

previous findings that most of the forecast uncertainty is associated with the large-scale flow, RM_DTE exhibits persistently high values over the Gulf of Mexico where the large-scale frontal boundary is located, which is especially evident at 24 and 30 hours. Meanwhile, the diurnal sea breeze circulation is not detectable in the RM_DTE field at the shown times. To obtain a better understanding of the vertical structure of the RM_DTE, the vertical profile of the horizontally-computed RM_DTE at the forecast times 24, 30, 36, and 42 hours is plotted along with its initial profile in Figure 29e. Compared to the initial profile, there is considerable growth both at lower levels (800 hPa and lower) and upper levels (with the peak at around 200 hPa), although, in terms of its absolute magnitude, RM_DTE is generated dominantly at the upper levels, which is a direct result of the fact that horizontal winds are in general strongest near the tropopause due to the existence of upper-level jets. To supplement the time evolution of the vertical profiles, the domain-total power spectra are also computed for the same forecast times (Figure 29f). The large-scale dominance of the initial forecast time reflects the fact that the initial ensemble state is obtained through climatological averaging and thus mostly reflects the phase variability within the climatological time series. While RM_DTE undergoes noticeable initial error growth (between 0 and 24 hours), most of the growth occurs at smaller scales (especially for wavenumbers 5 and higher). Meanwhile, the closely spaced spectra for the forecast times 24-42 hours is an indication that saturation for RM_DTE is reached within the first 24 hours of model integration.

As RM_DTE is a quantity that exhibits relatively large-scale variability (through its dependence on u, v, and T), the behavior of two other model variables, q and w, in

terms of their ensemble spread (measured by standard deviation), is presented here briefly for comparison. The time evolution of the horizontal distribution of *q* spread (Figure 30a-d) exhibits a strikingly similar behavior to RM_DTE with most of the ensemble uncertainty appears to be generated near the frontal boundaries associated with the larger-scale circulation. Unlike RM_DTE, which exhibits very large values at upper levels, the vertical distribution of *q* spread is concentrated mostly in the PBL and peaks at around 800 hPa (Figure 30e). The power spectrum of *q* spread is very similar in nature to RM_DTE with large-scale dominance in the initial distribution, growth at smaller scales, and saturation within the first 24 hours of the forecast period (Figure 30f). Meanwhile, a much smaller-scale structure is observable for *w* spread through the time evolution of its horizontal distribution (Figure 31a-d). This is also confirmed by the evolution of the power spectra between 0-42 hours (Figure 31f) which exhibits both a stronger growth from the initial spectrum at smaller scales and a larger diurnal variability within the 24-42 hour period. A discernible diurnal variability for the same period is also present in the vertical profile of *w* spread (Figure 31e), which has a distinct two-peak structure. The upper-level peak near 300 hPa, already present in the initial vertical distribution of *w* spread, is related to the upper-level RM_DTE peak through the strong divergent horizontal upper-level circulation (not shown). Meanwhile, the weaker lower-level peak near 850 hPa appears to be a consequence of the frontal boundary that is found to be the dominant factor in determining the uncertainty associated with the control-forecast RM_DTE and *q*.

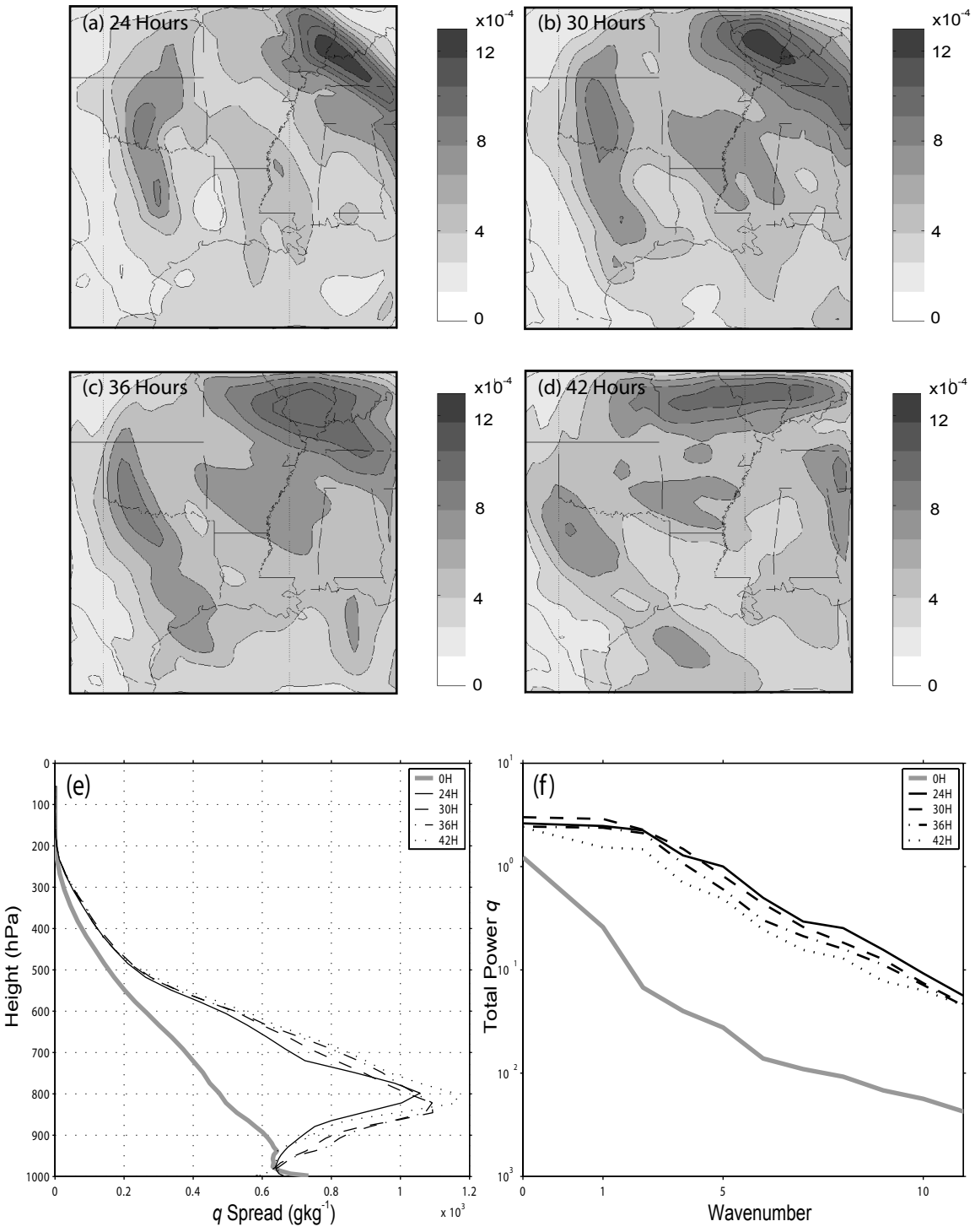

Figure 30. As in Figure 29 but for the ensemble spread (measured by the standard deviation) of q (gkg^{-1}).

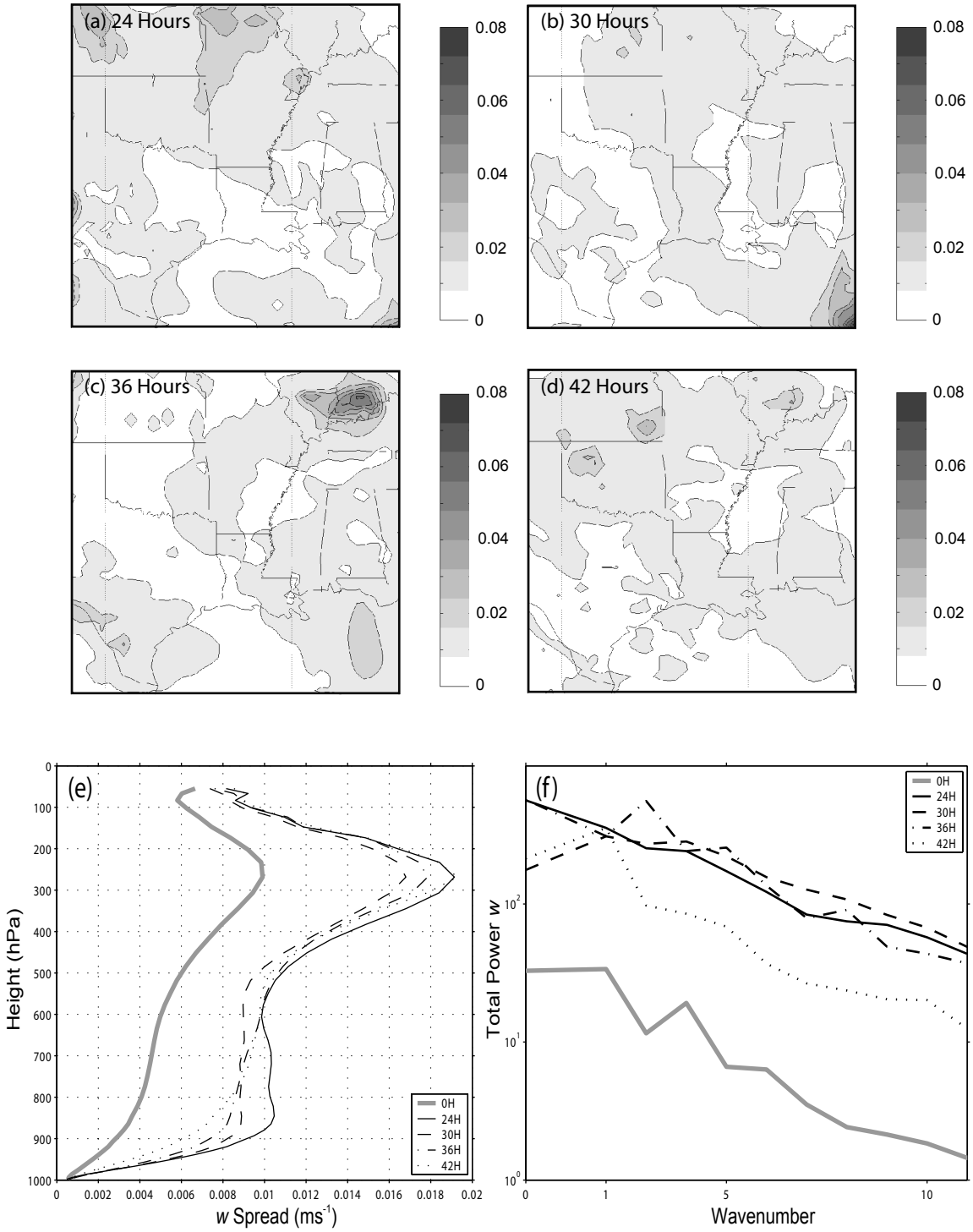

Figure 31. As in Figure 29 but for the ensemble spread (measured by the standard deviation) of w (ms^{-1}).

b. State-Only Estimation with Perfect-Model Statistics

In the perfect-model scenario, no parameter error is assumed for the forecast model. In other words, the same value for the parameter m_c (1.0) that is used for the truth simulation is assigned to each member of the forecast ensemble. Consequently, only state estimation is peformed (for the state variables u, v, w, T, q, and p'). During the 72-hour experiment, assimilation of observations with the EnKF are carried out every 12 hours beginning with the 12 hour forecast time. At each assimilation time, surface observations (72-km resolution) and sounding observations (324-km resolution) of u, v, and T are simulated from the truth simulation with an assumed observational error of 1 ms^{-1} for u and v and 0.5 K for T.

A primary indicator of the EnKF performance for this experiment is the horizontal distribution of forecast and analysis RM_DTE at any given assimilation time, as this is a quantity that reflects the cumulative deviation of the observed variables u, v, and T from their respective true values. Figure 32 shows these distributions for the assimilation times 12 and 24 hours. In general, we see that most of the forecast RM_DTE at both times is concentrated around the high-pressure area (Figure 32a and c), with the 24-hour forecast (Figure 32c) exhibiting a more distinct structure of low RM_DTE values over Alabama and the frontal boundary signature over western Gulf of Mexico. The distributions of the analysis RM_DTE at 12- and 24-hour assimilation times (Figure 32b and d) reveal that the EnKF performs exceptionally well as indicated by the domain-wide decrease of RM_DTE at both forecast times compared to their

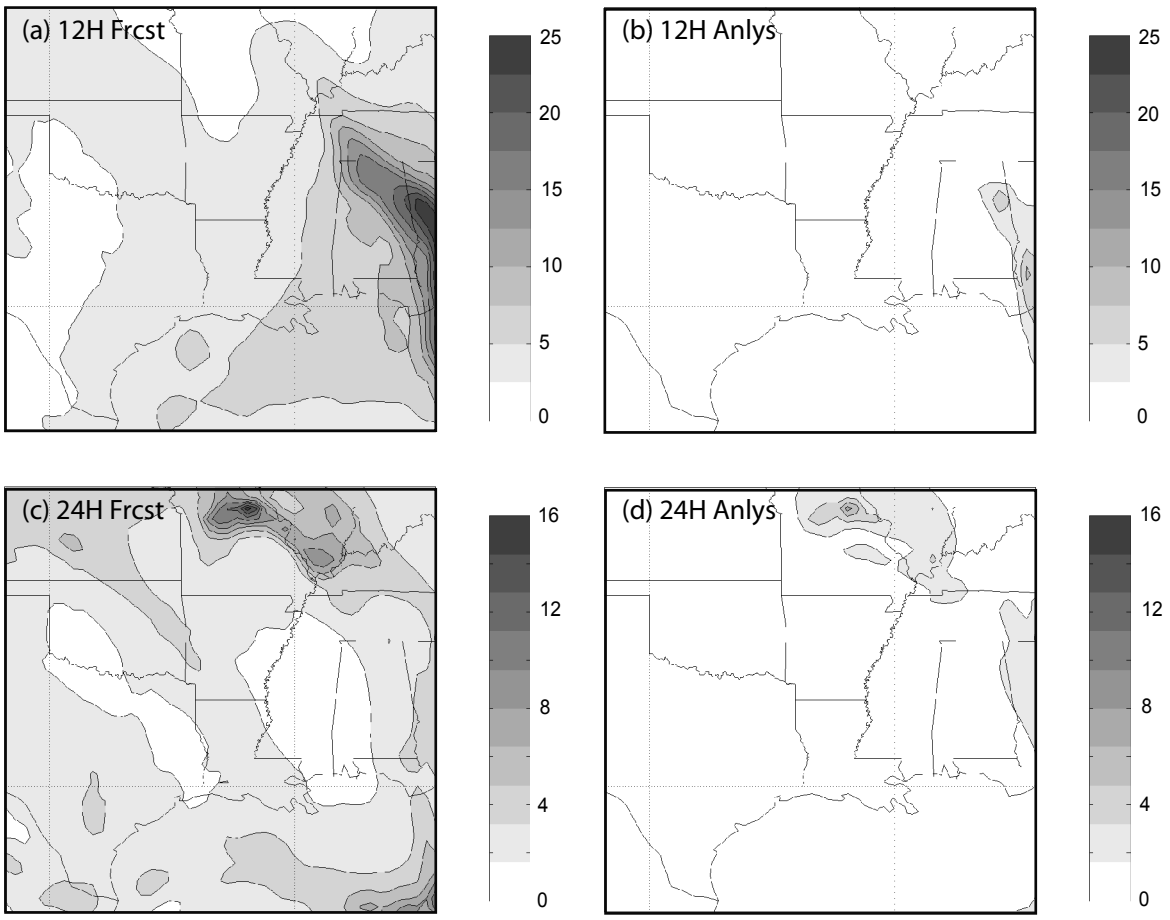

Figure 32. The horizontal distribution of the vertically-averaged RM_DTE (ms^{-1}) from 12-hour forecast (a), 12-hour analysis (b), 24-hour forecast (c), and 24-hour analysis (d).

respective forecast distributions. Specifically, the decrease in domain-averaged RM_DTE for 12-hour and 24-hour assimilation times is 86% and 74%, respectively. Compared to the initial domain-averaged RM_DTE, the overall reduction by the filter at the end of the 72-hour experiment is computed as 71%.

Further investigation of EnKF performance is carried out by plotting the horizontal forecast and analysis distributions of two unobserved variables *q* and *w* (Figure 33 and Figure 34). As was pointed out previously for the analysis of the pure-forecast control experiment, *w* exhibits a smaller-scale structure compared to *q*. It is believed that this scale disparity between *q* and *w* impacts the level of EnKF performance in the estimation of these two variables. The horizontal distribution of *q* rms error exhibits noticeable decrease at 12-hour and 24-hour assimilation times (compare Figure 33a to b, Figure 33c to d) with 48% and 28% reductions in domain-averaged rms error, respectively. In contrast, only minor error reduction is observed for *w* (compare Figure 34a to b, Figure 34c to d) with 15% and 8% at the two assimilation times 12 and 24 hours, respectively. Similarly, the overall decrease of rms error from initial to the 72-hour analysis times of 52% and 9% for *q* and *w*, respectively, also reflects lucidly the discrepancy of the EnKF performance between these two variables.

The vertical profiles of RM_DTE and the rms error of *q* and *w* for assimilation times 12 and 24 hours further unveil in what aspects the EnKF performance is different for these variables (Figure 35). While RM_DTE growth within the first 12-hour integration occurs mostly at lower levels, growth between the 12-hour and 24-hour

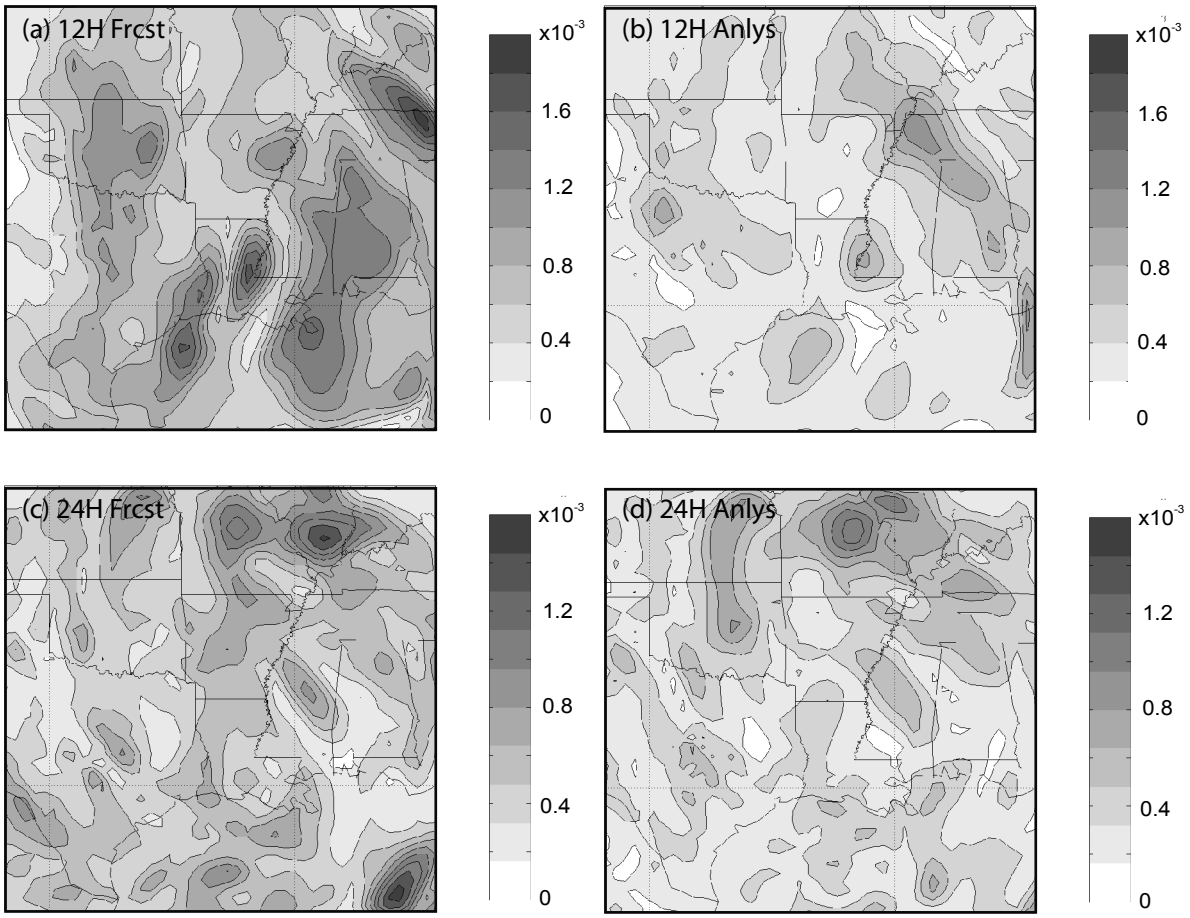

Figure 33. As in Figure 32 but for q (gkg^{-1}).

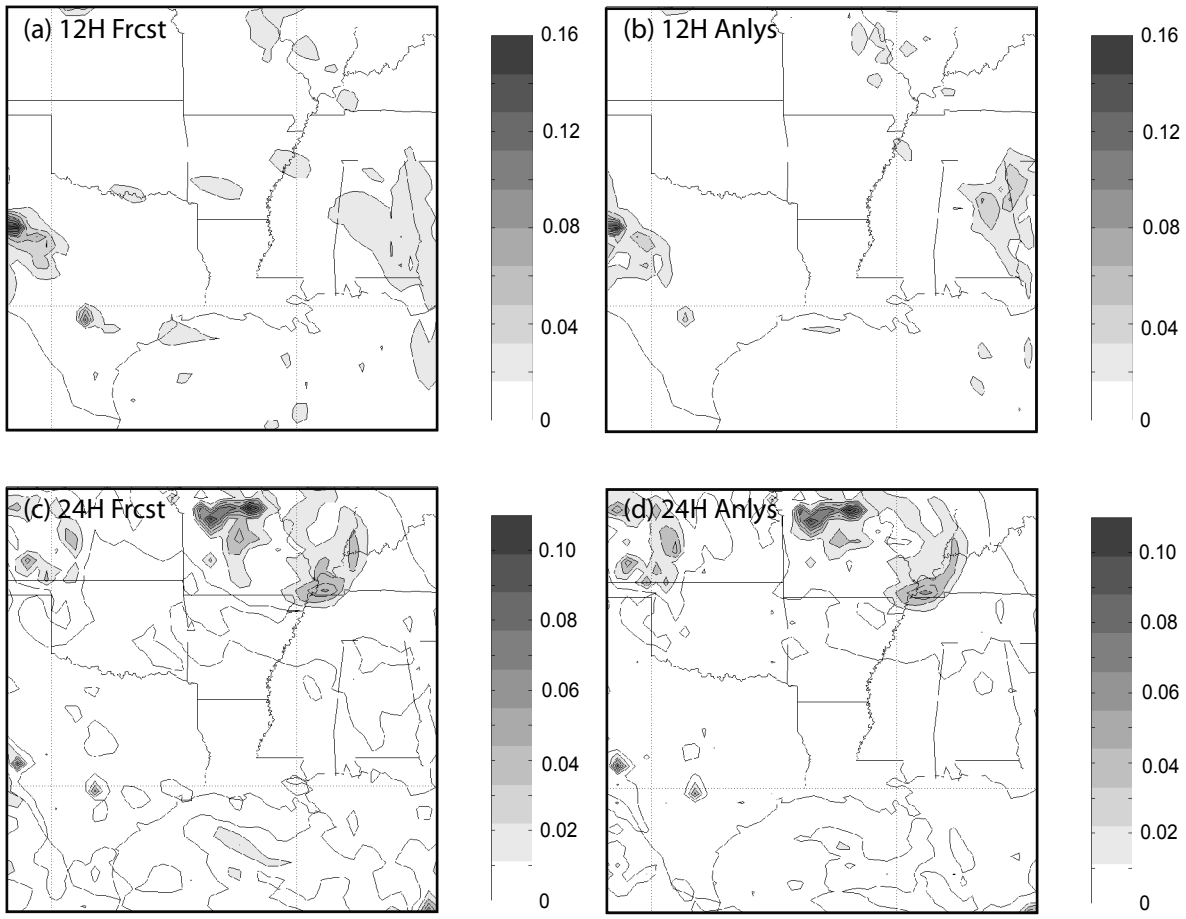

Figure 34. As in Figure 32 but for w (ms^{-1}).

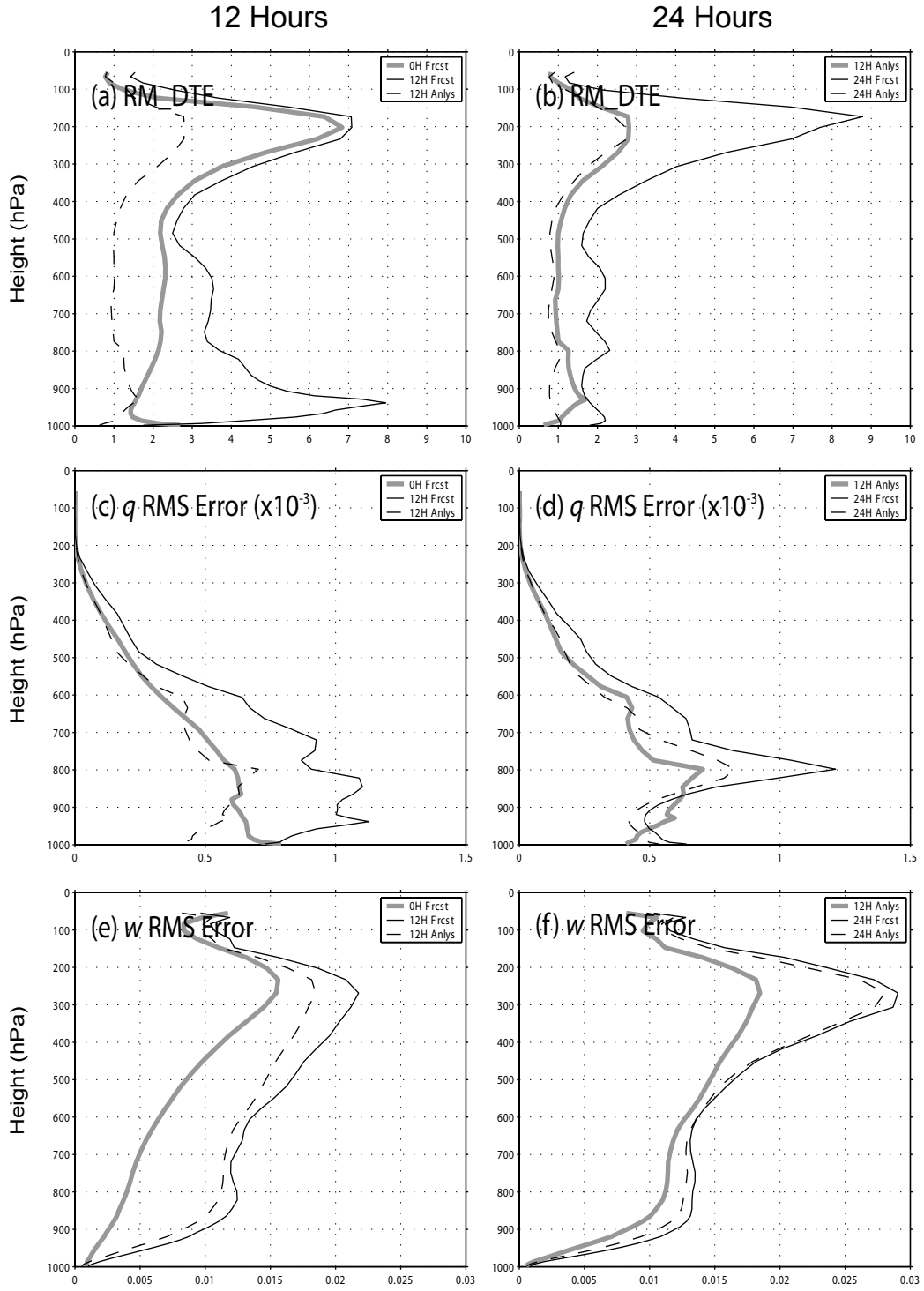

Figure 35. The vertical profiles of the horizontally- averaged RM_DTE (ms^{-1}, panels a and b), rms error of water vapor mixing ratio (q, gkg^{-1}, panels c and d) , and rms error of vertical motion (w, ms^{-1}, panels e and f). Assimilation times are 12 hours (left panels) and 24 hours (right panels).

assimilation times appears to shift toward the upper levels. At the 12-hour assimilation time, the EnKF is capable of removing RM_DTE across all levels. However, most of RM_DTE reduction at the 24-hour assimilation occurs at the upper levels and the almost perfect overlapping of the 24-hour and 12-hour analysis profiles hints to saturation for RM_DTE. The signs of error saturation at 24 hours is also evident for *q*. In agreement with previous findings, most of error growth for *q* takes place at or below 800 hPa and the EnKF appears to be capable of successfully removing these errors. Not surprisingly, EnKF peformance is least impressive for *w* which exhibits considerable error growth during both integration periods.

To further investigate the scale-dependent behavior of the EnKF for different variables, domain-total power spectra of RM_DTE and rms error of *q* and *w* are computed for the 12-hour and 24-hour assimilation times (Figure 36). For all three variables, error growth within the first 12-hour integration occurs dominantly at smaller scales. However, at the 12-hour assimilation time, while most of RM_DTE removal comes from larger scales, error removal for both *q* and *w* appear to be uniformly distributed at all scales. For all three variables, further error growth between the 12-hour and 24-hour assimilations remains primarily limited to the larger scales which is an indication that small-scale error saturation is possibly already taking place within the first 12 hours of model integration. Meanwhile, the EnKF performance at the 24-hour assimilation time becomes more confined to larger scales especially for RM_DTE and *q*, while for *w*, the EnKF appears not to be very effective in reducing errors across all

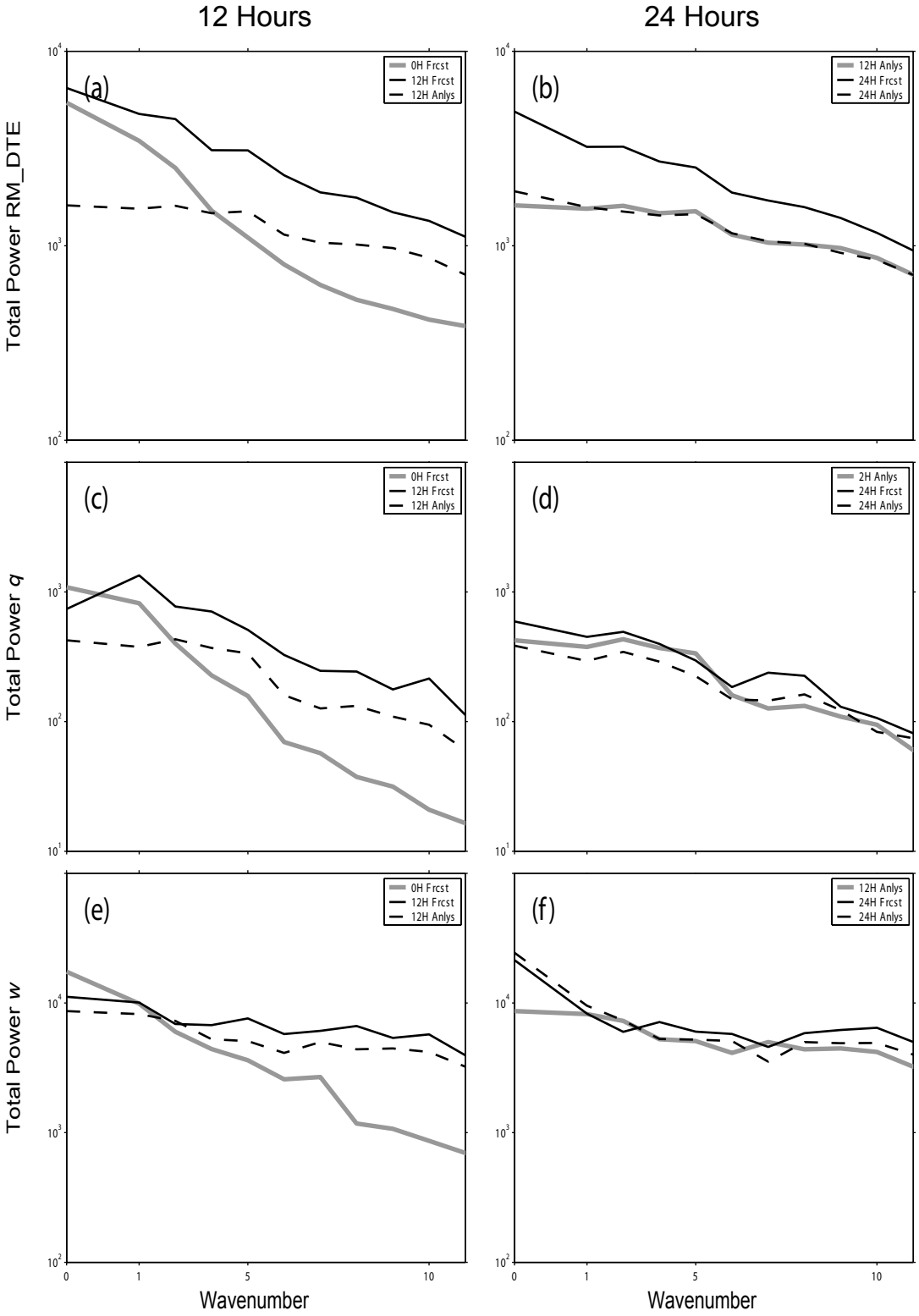

Figure 36. As in Figure 35 but for the domain-total power spectra as a function of wavenumber.

scales. This points to an inconsistency between the dominant scales of the information content of observations and the active scales of *w*.

The EnKF performance is best summarized by the error time evolution plots. For this purpose, plots for RM_DTE (Figure 37a) and rms errors of *T* (Figure 37b), *q* (Figure 37c), and *w* (Figure 37d) are generated. For comparison, the error evolution from the pure-forecast control experiment for each respective variable is also shown. In the pure-forecast experiment, fastest error growth for all variables almost exclusively occurs during the first 12 hours of the integration, confirming previous findings. Moreover, all variables except *w* appear to be very responsive to the EnKF assimilation process and exhibit vigorous error evolution characteristics. As was discussed before, *w*, because of its strong small-scale variability, is not very sensitive to the larger-scale information content of the simulated observations and thus the fluctuations in its rms error throughout the 72-hour EnKF experiment seem to be rather random and the rms error of the EnKF experiment remains rather close to that of the pure-forecast experiment for the 72-hour period. However, for other variables including the unobserved variable *q*, EnKF performance is strikingly strong. For instance, the mean error reduction for RM_DTE, *T*, and *q* over the 6 assimilation times is computed as 75%, 41%, and 25%, respectively. Moreover, compared to the final (72-hour) pure-forecast error, the EnKF achieves an overall error reduction of 87%, 62%, and 44%, respectively, for the three variables. Finally, another indication of satisfactory EnKF performance is

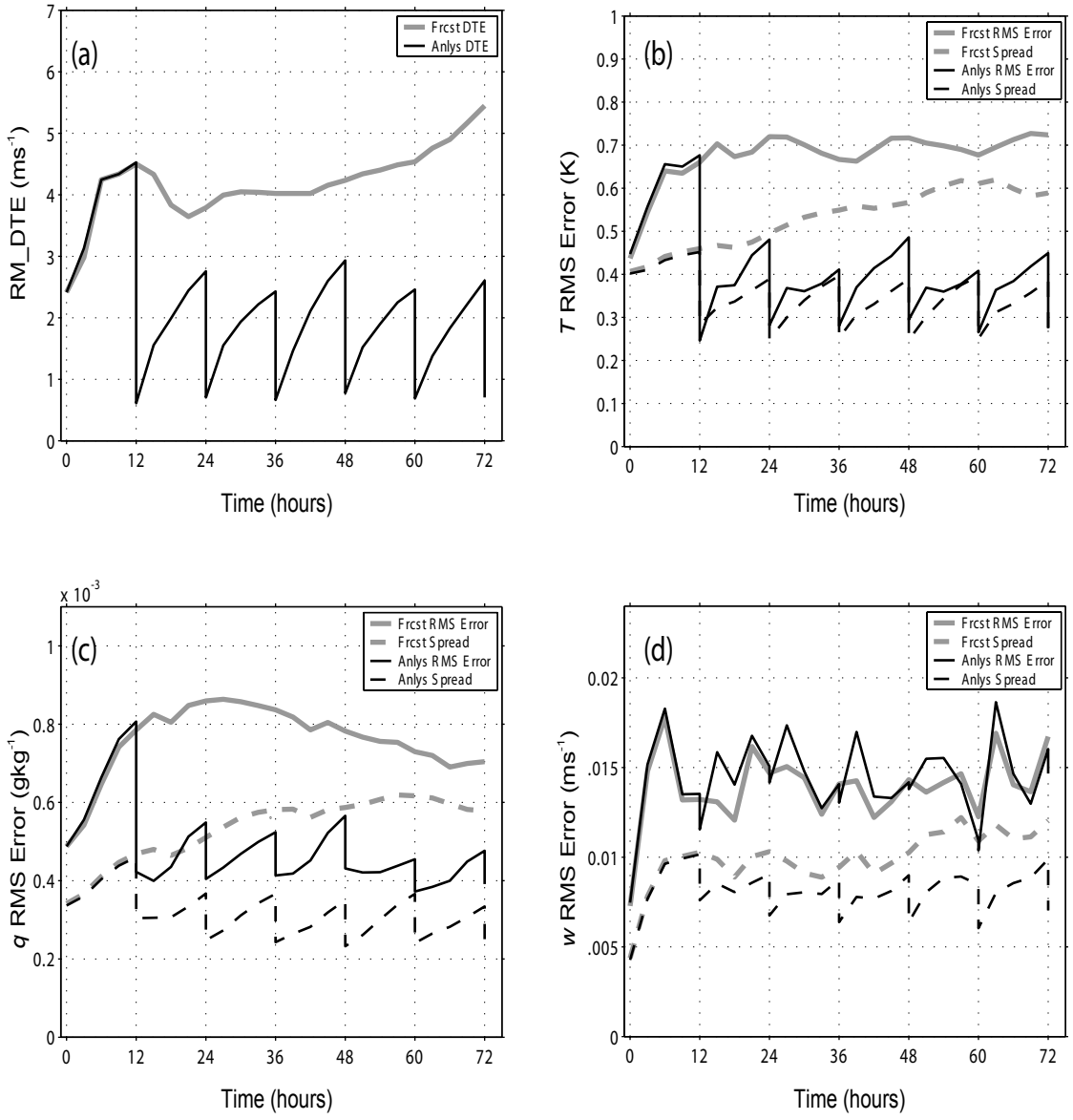

Figure 37. 72-hour evolution of RM_DTE (ms^{-1}, panel a), rms error (solid) and standard deviation (dashed) of T (K, panel b), q (gkg^{-1}, panel c), and w (ms^{-1}, panel d). In all panels, results from the pure-forecast (EnKF) experiments are shown with gray (black) lines.

the fact that, both for T and q, the respective rms error and standard deviation stay relatively close and do not diverge throughout the assimilation experiment (Figure 37b and Figure 37c), which is interpreted as a sign that filter divergence is not an issue for the state-only estimation experiment with the EnKF.

c. Parameter Identifiability

Similar to the procedure followed on pp. 73-83, identifiability for the parameter m_c is investigated through the rms correlation, $\overline{r}$, between m_c and the observed variables T, u, and v in a pure-forecast experiment where both the state and m_c are perturbed initially. To better analyze the information content of the surface and sounding observations, the horizontal distribution of $\overline{r}$ is computed both at the surface and as a vertically-averaged quantity and plotted for the variables T, u, and v in Figure 38, Figure 39, and Figure 40, respectively, for the forecast times 24 and 36 hours. A flow- and height-dependent distribution is apparent for all three observed variables. This is an indication that model dynamics contributes significantly to the evolution of the correlation between the observed model variables and m_c. Although the correlation signal at the surface is generally stronger compared to its vertically-averaged counterpart, its distribution exhibits smaller-scale structure. Consequently, while surface observations appear to be valuable because of the generally stronger correlation signal at the surface, sounding observations seem to have their value through the larger scale of the vertically-averaged correlation signal because of the better EnKF response to larger-scale information content of observations.

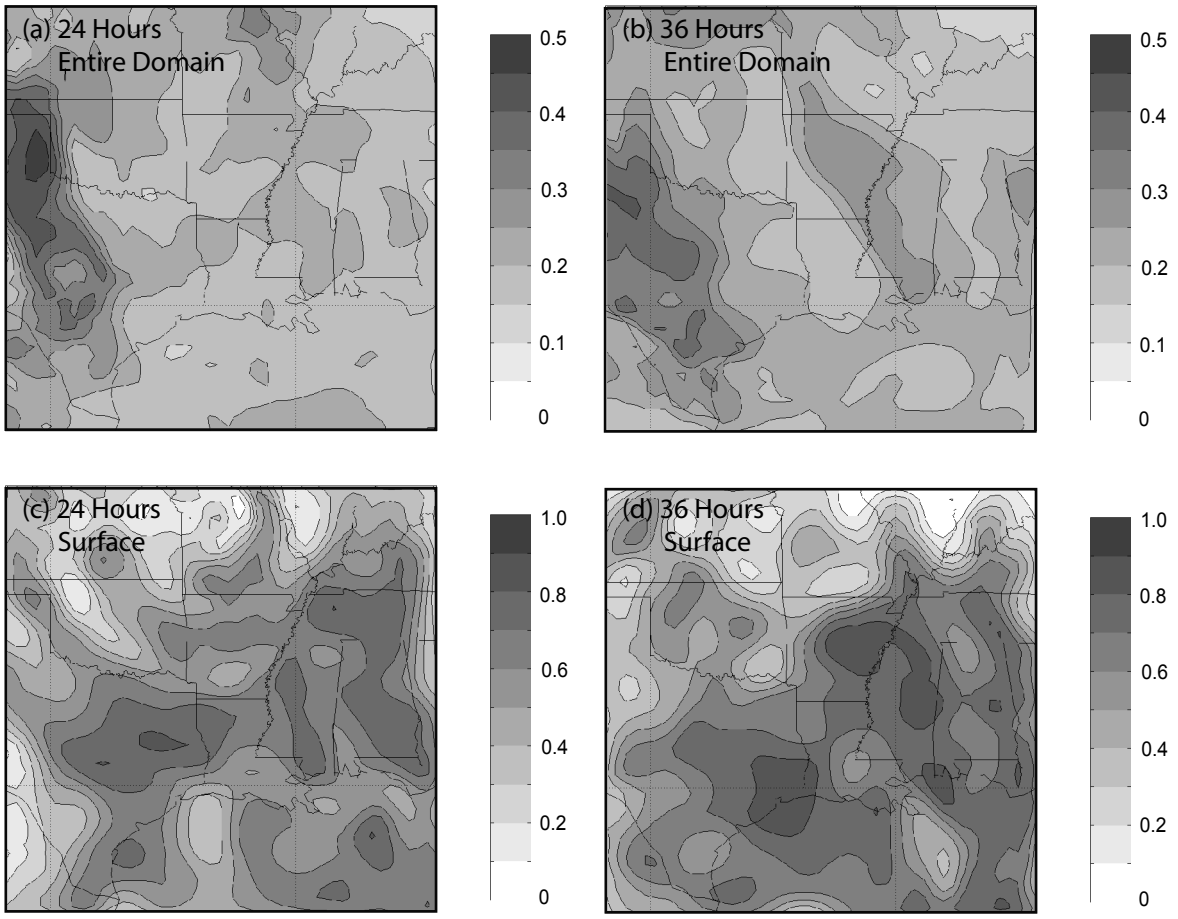

Figure 38. Horizontal distribution of the vertically-averaged (upper panels) and surface (lower panels) rms correlation between the parameter m_c and the variable T at forecast times 24 hours (left panels) and 36 hours (right panels). Contour interval is 0.05 (0.1) for the upper (lower) panels. The plots are generated from a pure-forecast experiment where both the state and the parameter are perturbed initially.

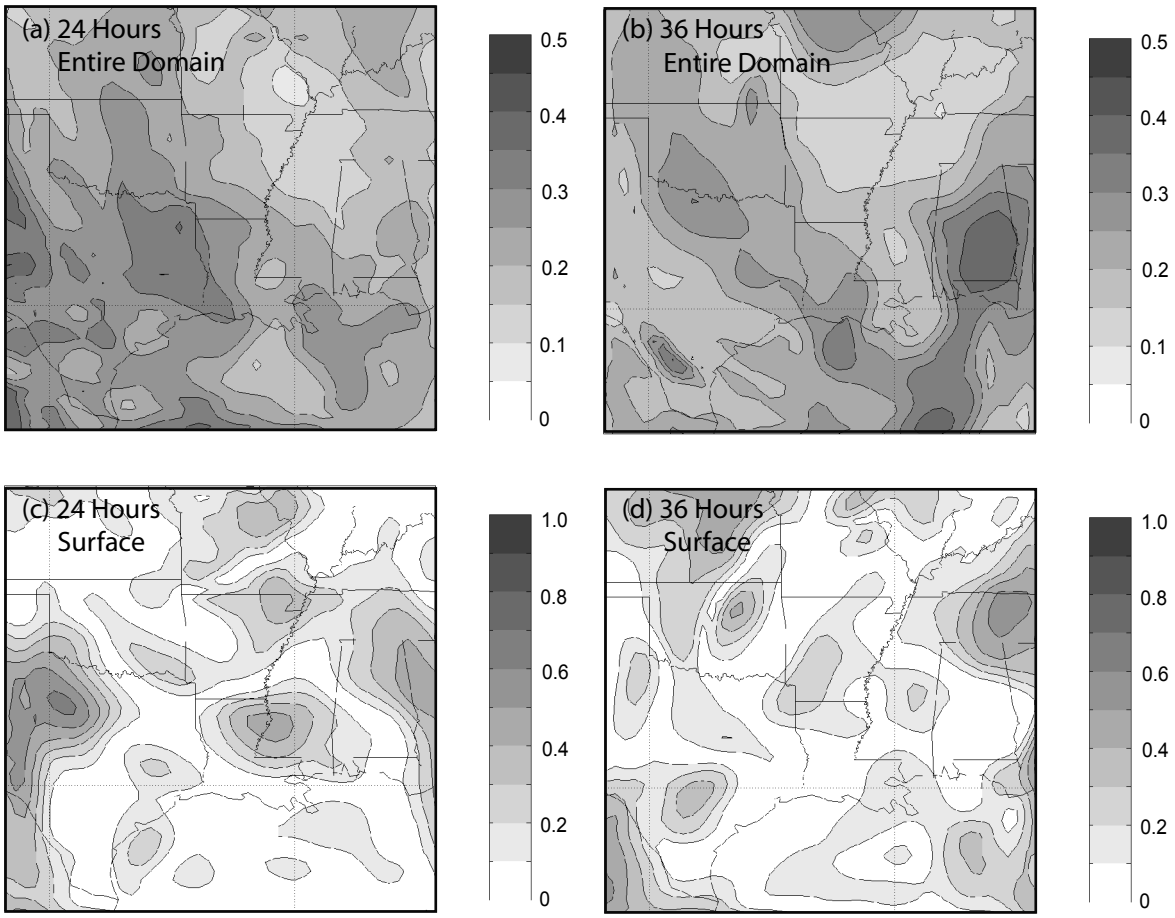

Figure 39. As in Figure 38 but for the variable *u*.

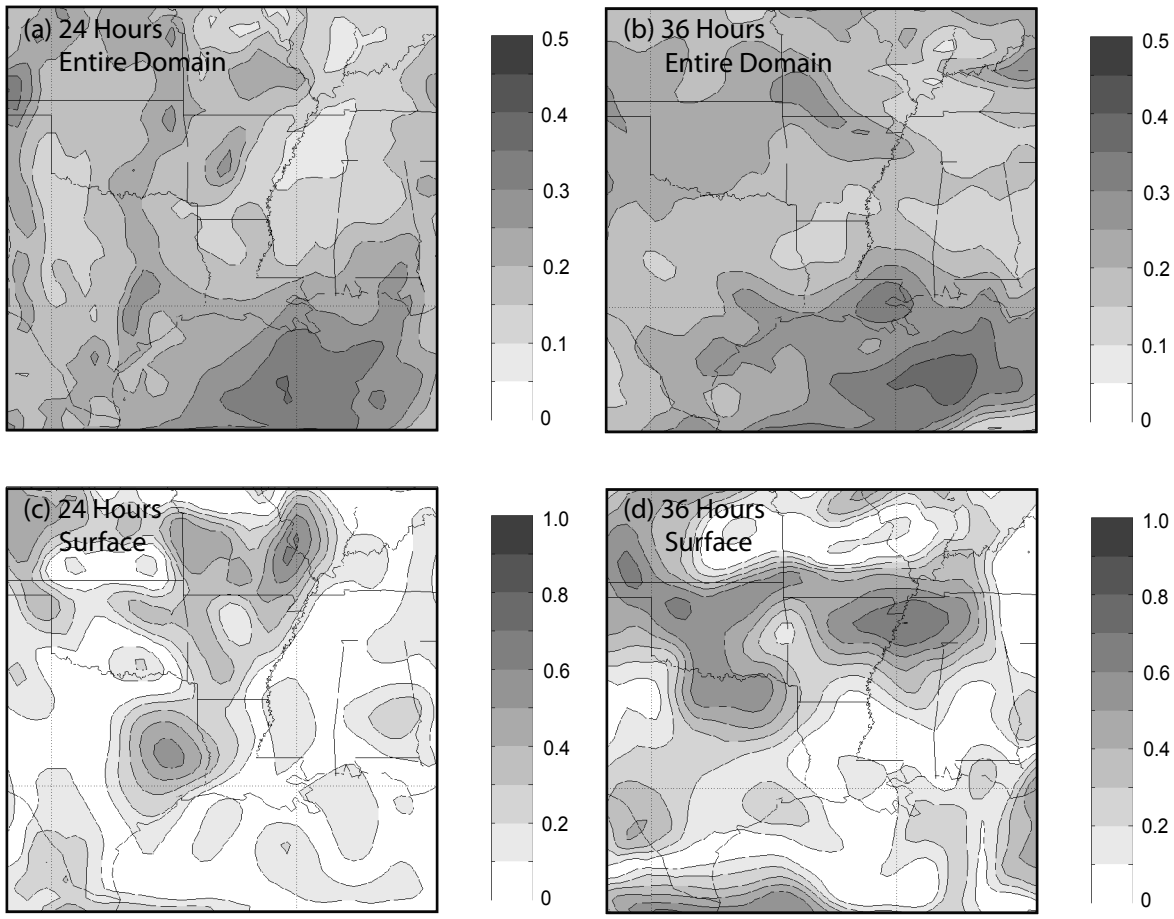

Figure 40. As in Figure 38 but for the variable *v*.

The 72-hour evolution of the vertically-averaged and surface $\overline{r}$ is shown in Figure 41 for the observed variables *T*, *u*, and *v*. The vertically-averaged $\overline{r}$ values consistently stay between 0.2-0.3 for all variables, which, according to previous findings with the two-dimensional sea breeze model (see pp. 73-83), appears to be sufficiently high from a parameter identifiability point of view. Meanwhile, almost no diurnal variability can be detected in the vertically-averaged $\overline{r}$ values for any of the observed variables, hinting to the large-scale nature of the dynamical processes that generate the correlation signal with the parameter m_c. In contrast, there is a significant discrepancy of surface $\overline{r}$ values among the three variables, with *T* exhibiting a stronger signal compared to *u* and *v*, which both remain very close in magnitude to their vertically-averaged counterparts. This discrepancy is likely to result in the information content of *T* dominating over *u* and *v* at the surface, possibly limiting the influence of surface observations over the overall EnKF performance.

In general, there appear to be competing factors that are likely to favor surface observations and sounding observations in different ways. At this point, there is no convincing argument for any preference of one observation type over the other and it is believed that both observation types will have a positive impact through their complex response to flow dependence, scale sensitivity, and information content. Nevertheless, correlation analysis suggests that a sufficiently strong signal is present in the surface and sounding observations of *T*, *u*, and *v* making it likely for the parameter m_c to be estimated through the EnKF process.

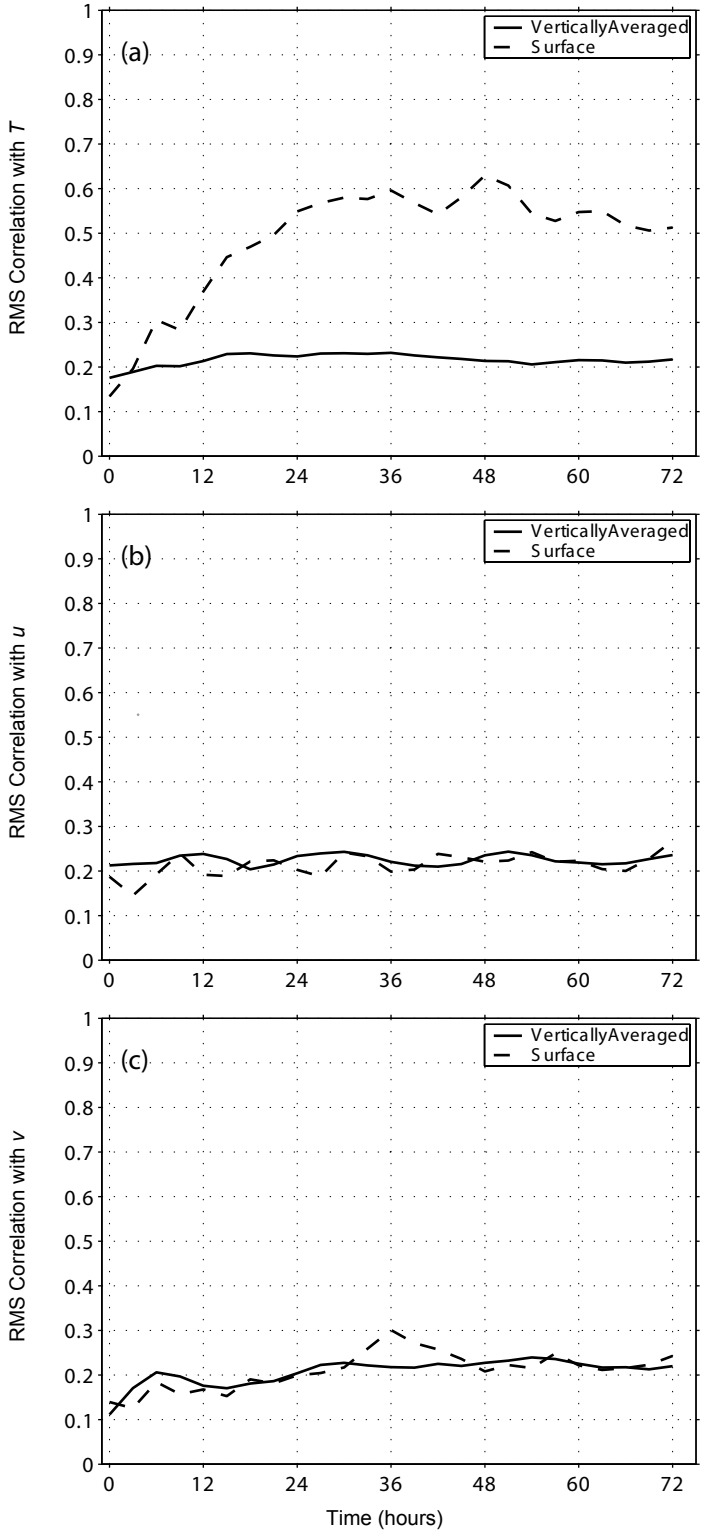

Figure 41. The 72-hour evolution of the vertically-averaged (solid) and surface (dashed) rms correlation between the parameter m_c and the variables T (a), u (b), and v (c).

d. Parameter Sensitivity

To better understand how the model responds to the error in the value of the parameter m_c, results from pure-forecast experiments with and without initial parameter perturbation are briefly compared in this section. For this purpose, two experiments are performed. In one case, only the initial parameter is perturbed (standard deviation of 0.3) about the incorrect mean parameter value (1.2), while in a second experiment, both initial state and initial parameter are perturbed. These experiments are then compared to the perfect-model pure-forecast experiment where only the initial state is perturbed. The analysis is carried out through the comparison of the ensemble spread of the model variables T, u, q, and w from the three experiments (Figure 42). With only the initial parameter perturbed (pure model error, Figure 42, solid gray lines), we see that about 10-30% of the pure initial-state ensemble spread (Figure 42, solid black lines) is generated throughout the experiment for all four variables. Because a quantitative comparison of the initial state and initial parameter error is not possible because of the difference of the nature of these two sources of error, an absolute judgement about the relative magnitudes of the ensemble spread that results from pure initial-condition and pure model errors is not possible. Nevertheless, the model appears to exhibit some degree of sensitivity to the initial parameter perturbation as seen through the growth of the ensemble spread for all of the model variables shown.

When both the initial state and parameter are perturbed (combination of initial-condition and model, Figure 42, dashed black lines), the resulting ensemble spread for

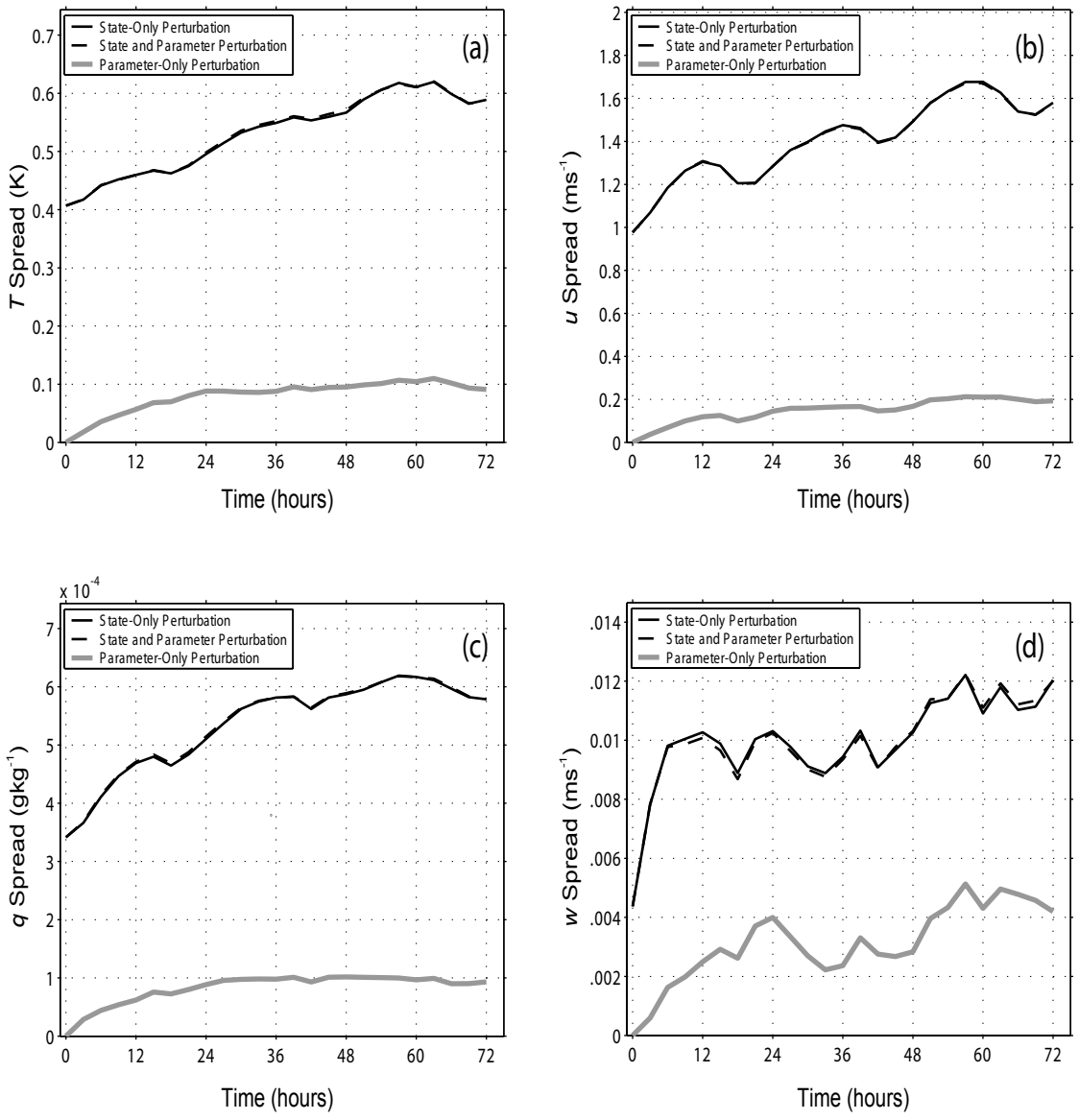

Figure 42. The 72-hour evolution of the ensemble spread from the pure-forecast experiments with only intial state perturbed (solid black), both initial state and parameter perturbed (dashed black), and only initial parameter perturbed (solid gray) for the variables *T* (a), *u* (b), *q* (c), and w (*d*).

all variables remains very close to the pure initial-state ensemble spread (Figure 42, solid black lines). Apparently, the existence of model sensitivity to pure model error does not necessarily translate into sensitivity when both initial-condition and model errors are present. In other words, when initial-condition error is present, the model uncertainty seems to span a sufficiently large phase space to possibly include the uncertainty of the model error associated with the parameter m_c (for the magnitude of the parameter tested in the experiments).

e. Parameter Estimation Experiments

Two 72-hour estimation experiments for the parameter m_c are conducted with mean initial parameter values of 1.2 and 1.65 (as opposed to the true value of 1.0). Again, 12-hour assimilations are performed with the same filter and observation characteristics as the perfect-model case (pp. 109-119). The time evolution of the estimated mean parameter value for both experiments, along with the true parameter value and the 1-σ spread limits, are shown in Figure 43. As discussed on pp. 61-65, the shaded area is intended to be a visual guidance for the acceptable variability of the mean parameter value. When ensemble statistics are perfect, the true parameter value should be expected to be found within this interval 68% of the time. In the experiment with the initial parameter error of 0.2 (Figure 43a), the estimation performance even exceeds this expectation with the true value remaining within the 1-σ limits during the entirety of the experiment. The estimated mean parameter value consistently converges toward the true value by the end of the second assimilation cycle (24 hours) and then

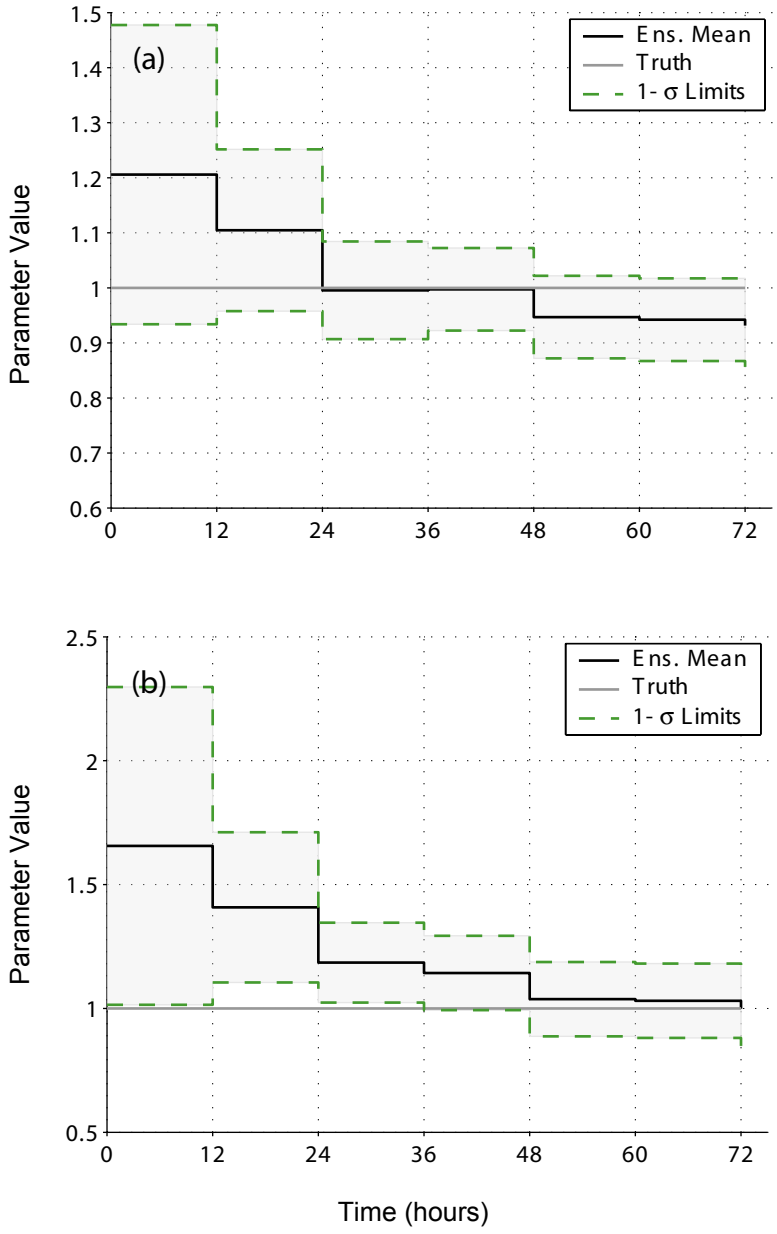

Figure 43. The time evolution of the mean parameter (m_c) value (solid black) vs. the true parameter value (solid gray) for the experiments with initial parameter error of 0.2 (a) and 0.65 (b). The shaded area represents the one-standard-deviation limits of the parameter spread.

stays within about 5% of the true value during the remainder of the experiment. When the initial parameter error is increased to 0.65, a slower convergence of the estimated mean parameter value is observed (it takes about 48 hours as opposed to 24 hours for the mean parameter to converge within the same relative neighborhood of the true parameter value). Nevertheless, from the view point of the final estimated parameter value, the experiment is very successful as the mean estimated value almost exactly matches the true parameter value. In terms of parameter variability, EnKF performance is also found satisfactory as the true value remains within the 1-σ limits for 4 assimilation cycles out of 6 (or 66%, counting the first cycle where the slight discrepancy is ignored as it is related to the initialization of the parameter and not attributable to filter performance).

Finally, the performance of parameter estimation is also investigated through an error analysis. For this purpose, the time evolution of RM_DTE, *T* rms error and spread, and *q* rms error and spread are plotted for the two experiments with initial parameter error of 0.2 and 0.65 (Figure 44). For comparison, results from the respective worst case experiments, which are initialized with the same respective initial parameter error but not involve estimation of the parameter, are also plotted. In both estimation experiments, the evolution of the error for the different variables is stable. Moreover, consistent with the findings in the previous section, for the initial parameter error of 0.2, the overall level of error is very similar for the estimation and worst-case experiments. In general, only 1-2% overall error reduction (measured by the time-average of RM_DTE and rms error for each variable) is achieved compared to the worst case.

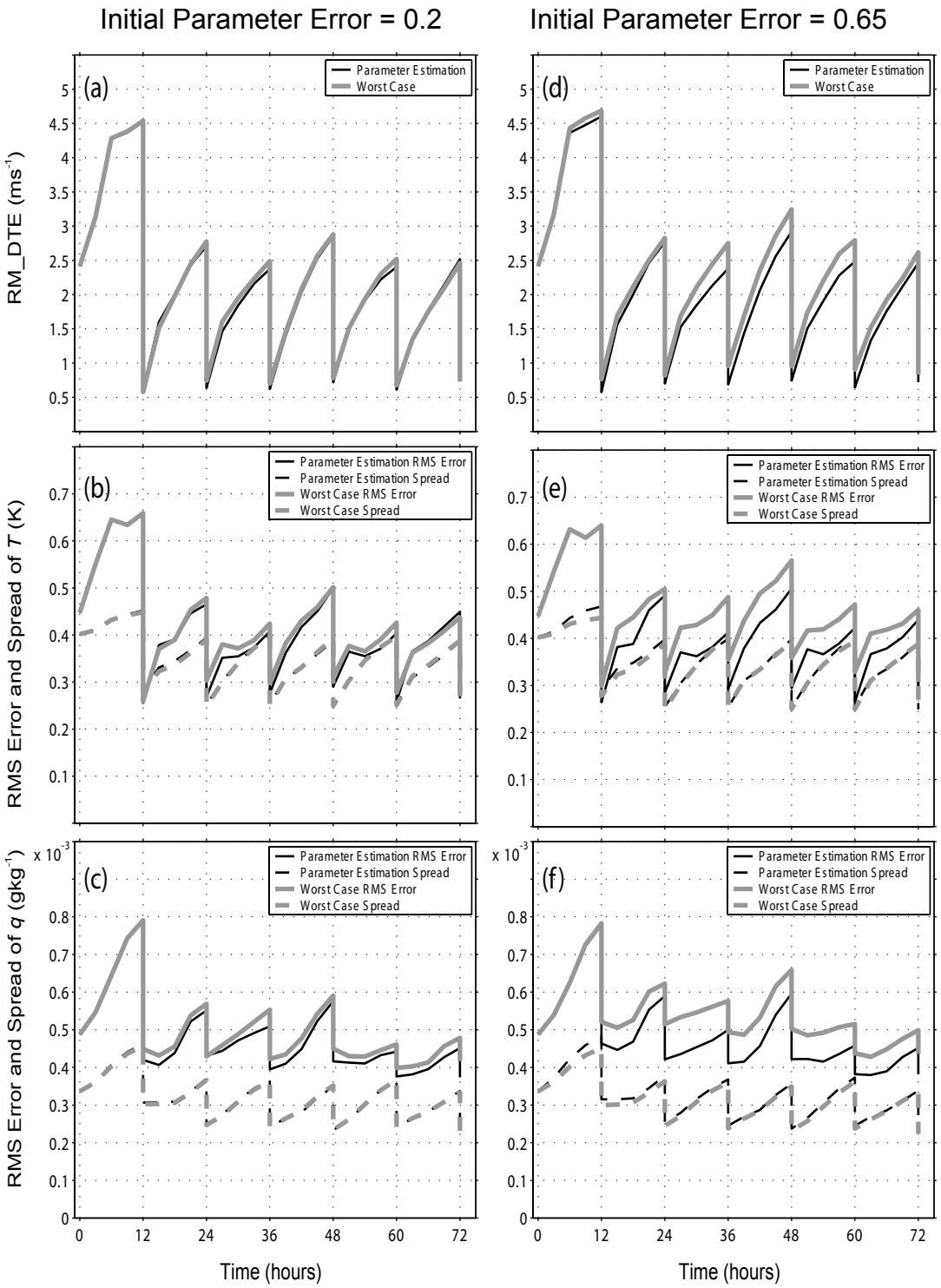

Figure 44. The time evolution of RM_DTE (panels a and d) and the rms error (solid black) and spread (dashed black) of T (panels b and e) and q (panels c and f) from estimation experiments with initial parameter error of 0.2 (left panels) and 0.65 (right panels). The same quantities from respective worst-case experiments are shown with gray lines.

Similarly, the average percentage of error reduction over the 6 assimilation steps is also very similar for the two cases with the EnKF performing better only by about 1-2 percentage points for the estimation experiment. Nevertheless, the improvement in error becomes more pronounced when the initial parameter error is increased to 0.65. For this case, while the improvement in the overall level of error is now a more noticeable 7-8% compared to the worst case, the average percentage of error reduction is also stronger by about 4-5 points.

SUMMARY AND CONCLUSIONS

This dissertation documents the effectiveness of ensemble-based Kalman filtering for simultaneous state and parameter estimation in the context of thermally-forced circulations for two models with progressively increasing complexity. In the two-dimensional sea breeze model written for the purpose of this study, forcing is maintained through an explicit spatially- and diurnally-varying heating function with an added stochastic component. Pure forecast experiments reveal that the model exhibits moderate levels of overall nonlinearity. Ensemble spread of both buoyancy and vorticity is found to remain stabilized (error saturation) at a certain level and does not show signs of large-scale growth over a 10-day period. Strongest nonlinearity coincides with the peak sea breeze phase of the circulation in timing and with the sea breeze front spatially. Considerable small-scale error growth occurs at this phase, which is most pronounced in the vorticity field. Nevertheless, at other phases of the sea breeze, the model tends to diffuse and advect vorticity errors out of the domain and lacks a mechanism to translate small-scale errors produced during the peak sea breeze phase into larger-scale errors at later times. As a result, the overall vorticity error appears stabilized and fluctuates in a diurnal manner with distinct day-to-day variability. However, buoyancy retains its memory of large-scale initial-condition error for a much longer duration because of its horizontally uniform distribution and weaker diffusion. This results in a dominantly large-scale error structure for buoyancy so that it exhibits no diurnal variability.

EnKF control experiments are performed with simulated surface buoyancy observations on land that are placed 40 km apart and sequentially assimilated at 3-hour intervals. At the first analysis step, the filter is observed to successfully remove most of the large-scale phase-difference errors resulting from the initial conditions. At this step, domain-averaged error for buoyancy and vorticity is reduced by about 83% and 42%, respectively. Subsequent analyses continue to remove error at an increasingly slower rate and error ultimately saturates within about 24 hours at a level that is proportional to observation accuracy.

Surface buoyancy observations with 40-km spacing are found to selectively resolve the large-scale features of the buoyancy field. As a result, the filter performs much better at larger scales for buoyancy. This becomes especially important at later stages of an assimilation experiment when most of the large-scale initial-condition error is already removed from the forecast domain. Stochastic heating then consistently results in large-scale errors in buoyancy which are then effectively removed by the filter at each analysis step. Meanwhile, small-scale vorticity errors are mostly induced by nonlinear processes near the front during the peak sea breeze phase. As a result, even though error growth of vorticity becomes more pronounced during the peak sea breeze phases, long-term vorticity error remains small because growth only occurs for a limited duration during the diurnal cycle. Moreover, the filter is observed to perform well in reducing the small-scale vorticity error during such active phases. It is believed that 40-km surface buoyancy observations, in addition to their natural large-scale information content consistent with their spacing, contain sufficient small-scale information so that

the filter is effective at both removing large-scale errors due to the stochastic heating and small-scale errors due to the nonlinearities of the sea breeze front.

Sensitivity experiments demonstrate that the rms error of the unobserved variable vorticity is most sensitive to observation accuracy, ensemble size, analysis frequency, and radius of influence. On the other hand, vorticity error reduction by the filter is not sensitive to decreased observation spacing to 20 km or the assimilation of an additional single sounding. Apparently, the information content of buoyancy observations does not change so that the additional sounding or the reduction of observation spacing do not contribute significantly to the better sampling of the smaller-scale structure of vorticity.

There are a number of limitations of the model worth mentioning briefly, as they are relevant in terms of sea breeze dynamics and the application of the EnKF. Dynamical simplifications were made to achieve computational efficiency: The Coriolis force is omitted because it does not have a direct impact on the nonlinearity of the sea breeze circulation; the hydrostatic assumption enables vorticity to be independent of the horizontal distance so that the inversion algorithm (between vorticity and stream function) becomes much simpler to implement; and the assumption of dry dynamics eliminates one entire equation and allows the model to be integrated forward much more efficiently. Such simplifications undoubtedly make the sea breeze model less realistic yet more accommodating in terms of understanding and controlling otherwise complicated interactions among model and filter components. Lastly, an important limitation is related to the choice of representing thermal forcing through an explicit heating function rather than a flux-based scheme that implicitly resolves heating.

It is believed that the current model setup offers a sufficient level of simplicity to allow for the preliminary investigation of a novel application of the EnKF to forced-dissipative systems, while retaining most of the key characteristics of sea breeze dynamics such as the inertia-gravity-wave structure and the nonlinear sea breeze front. An interesting future approach is to estimate source/distribution properties of a scalar tracer through the integration of a chemical concentration model which would facilitate the investigation of connections between the sea breeze circulation and the transport of certain inert chemicals. Finally, the findings on the applicability of the EnKF to the sea breeze circulation also have implications for climate systems as they are large-scale forced-dissipative flow systems.

Estimation of the imperfect parameters by the EnKF is facilitated through state augmentation, which is the process of concatenating unknown parameters and state variables into a single vector. Up to six model parameters are subjected to estimation attempts in various experiments. These parameters are mean horizontal wind ($\overline{u}$), static stability (N^2), vertical diffusion coefficient of buoyancy (κ_b), vertical diffusion coefficient of vorticity (κ_η), heating amplitude (A_0), and heating depth (z_0). The estimation of single imperfect parameters with the EnKF is in general very successful resulting in rms error of model variables that is indistinguishable from the respective perfect-parameter cases. Parameters that appear to be most sensitive in their estimation are κ_η, N^2, and z_0.

Increasing the number of imperfect parameters leads to a decline in the level of improvement achieved by parameter estimation. However, the EnKF is observed to

consistently perform well and produce quantitatively similar results to single-parameter estimation for up to 3 imperfect parameters. When the number of imperfect parameters is increased to 6, which constitute a parameter space believed to control most of the uncertainty of the sea breeze circulation, a noticeable decline in the estimation power of the filter is observed, although the overall EnKF performance in terms of the error statistics is still superior to the worst-case scenario (when no parameter estimation is performed), as is demonstrated by the consistently improved MREs of both model variables (60% for buoyancy and 54% for vorticity). At this point, parameters that appear to have reached their identifiability threshold are N^2 and κ_η. It is believed that the identifiability of N^2 is linked to the lack of information content of the land surface buoyancy observations so that a vertical profile is not appropriately sampled. On the other hand, the lack of identifiability of κ_η is rather related to numerical instability issues and does not appear to be critical for the overall multi-parameter performance of the filter as a 5-parameter experiment with perfect κ_η does not reveal any significant improvement over the 6-parameter results. Similarly, when the 6-parameter estimation results with land surface observations are compared to a 6-parameter experiment with sounding observations of same frequency, although an improvement is observed in the estimation of N^2, a significant overall rms error performance is not obtained because of the worsened estimation performance in other parameters.

Several aspects of the filter configuration have been found to considerably influence the identifiability of the parameters. One such significant factor is the ensemble size. Through its direct impact on sampling quality, while an increase in the

ensemble size to 100 members results in the improved estimation of κ_η, experiments with a smaller ensemble size of 20 members lead to the complete loss of identifiability of the critical parameters N^2 and κ_η. Interesting results are obtained from the sensitivity experiments with smaller values of radius of influence (75 and 50 grid points). While the parameters κ_b and z_0, which otherwise exhibit strong identifiability, become completely non-responsive to estimation attempts with a radius of influence of 50 grid points, N^2 actually benefits significantly from the smaller radius of influence in terms of its identifiability. As is also hinted by the comparison of land-based and sounding observations, this parameter-specific response indicates that there is a complicated relationship between the global model parameters and the spatial information content of observations. It is conjectured that a spatially-oriented strategy for covariance "localization" does not necessarily lead to an optimal solution from a parameter estimation point of view.

Another important result that is obtained pertains to the sensitivity of the parameter estimation to the parameter variance limit. Experiments with a smaller (1/10 of initial parameter error) and a larger (1/2 of initial parameter error) variance limit indicate that the optimal limit is parameter-specific. While most parameters appear to be identifiable when a systemwide limit of 1/4 initial error is applied, κ_η becomes more responsive with the smaller limit tested while N^2 exhibits better identifiability with the larger limit. Although the method that is applied for the treatment of parameter variance is ad hoc in nature, it is nevertheless concluded that such parameter-dependent sensitivity to variance limit provides insight for the behavior of the variability of

individual parameters. While the goal here is not to investigate the nature of parameter variability in specific details, it is believed that a better understanding of it that would lead to a parameter-specific treatment of variance is imperative for the optimality of the parameter estimation.

An important conclusion that is reached through the estimation and sensitivity experiments with multiple uncertain parameters is that significant nonlinearities exist between the model variables and model parameters so that the errors associated with individual parameters tend to counterbalance each other in many complicated ways. As a result, attempts to improve the estimation of one parameter unavoidably influence the estimation of other parameters. Such interactions will clearly be more critical in more complicated models with many more parameters and thus greater degrees of freedom. The parameter-dependent differences in the overall level of correlations for different spatial observation configurations and the parameter-specific sensitivity to radius of influence suggest that a straightforward spatial covariance localization does not necessarily produce optimality. It is therefore believed that a key to success in such complicated models will require a unified "meta-localization" approach and conjectured that a global localization in the correlation space may be a feasible alternative. Such a technique should be expected to improve the identifiability of the model parameters considerably especially for larger models with many complex parameterization schemes.

As a further note, at its current condition, there are several ad hoc components of the estimation scheme that need to be addressed in the future. As there is no direct observational or physical evidence about the variability of parameter values, in this

study, the magnitude of initial parameter spread has been chosen through a subjective evaluation of sensitivity of model performance to different parameter values. For applications to more complicated models, real observations, and/or operational environments, a more systematic approach would be required to establish techniques for determining an appropriate magnitude of parameter spread.

An investigation of the suitability of the EnKF for parameter estimation in the context of a meteorological model of operational complexity is also conducted in this study. For this purpose, the Pennsylvania State University-National Center for Atmospheric Research MM5 model is used with a 36-km horizontal resolution and ~2000 km domain size (55×55 grid points) covering the southern United States and northern Gulf of Mexico. The model has 43 layers in the terrain-following vertical coordinate and is configured to employ the MRF PBL, Grell cumulus, and simple ice microphysics parameterization schemes. With the current configuration, a total of 6 prognostic variables are available including the Cartesian velocity components (u, v, w), pressure perturbation (p'), temperature (T), and the mixing ratio for water vapor (q). The ensemble size for all experiments is chosen as 40 and a 41st member is generated as the truth with the same ensemble statistics. The state initialization is carried out by a climatological technique similar to the one used for the two-dimensional sea breeze model. The EnKF configuration for the estimation of the state is also very similar to the filter designed for the two-dimensional sea breeze model. Assimilations are performed with a 12-hour interval with simulated sounding and surface observations of u, v, and T assuming observational errors of 1 ms^{-1} for u and v and 0.5 K for T. To realistically

represent the operational observational spacing for the continental United States, horizontal spacing for the sounding and surface observations is set at 324 km (9 grid points) and 72 km (2 grid points), respectively.

In this study, only single-parameter estimation experiments are performed. The parameter chosen for this purpose is a multiplier (m_c) that modifies the global eddy mixing coefficient computed within the MRF PBL scheme. Initial parameter perturbation is obtained randomly with a standard deviation of ~0.3 in most of the experiments. To overcome the rank inconsistency between the observational vector and the single parameter m_c, the global updating strategy adopted for the two-dimensional sea breeze model is modified such that prior m_c is transformed into a homogeneous two-dimensional vector defined at the surface with the same prior value at every grid point and the updating performed spatially using the same localization characteristics as the updating of the state. Following the updating, the global updated parameter value is retrieved by spatially averaging the updated m_c vector.

The 72-hour perfect-model forecast experiments reveal the existence of a persistent anti-cyclonic circulation centered around Louisiana with a weak local sea breeze circulation detectable across the coastline between East Texas to Louisiana in the PBL and especially during the second day of the simulation. However, deviations from the truth simulation are mostly dominated by the large-scale circulation and imply that largest uncertainties in the meteorological prediction arise from the large-scale circulations and their associated frontal systems while the sea breeze circulation is more predictable and does not contribute to the uncertainty significantly. In terms of root-

mean difference total energy (RM_DTE) and q, initial conditions are found to be concentrated mostly at larger scales, while smaller-scale error growth and saturation occurs within 12-24 hours. Meanwhile, a much smaller-scale structure is observable for w, with a stronger initial error growth at smaller scales and a more distinct diurnal variability across forecast times.

State estimation with perfect-model statistics reveals that the EnKF performs well for most variables. The mean error reduction for RM_DTE, T, and q over the 6 assimilation times is computed as 75%, 41%, and 25%, respectively. Moreover, for the same three variables, the EnKF achieves an overall error reduction of 87%, 62%, and 44%, respectively, compared to the final (72-hour) pure-forecast error. For T and q, the respective rms error and standard deviation stay relatively close and do not diverge throughout the assimilation experiment indicating that filter divergence is not an issue for the state-only estimation experiment with the EnKF. The EnKF is also found to be more responsive to larger-scale information contained by the observations. Because of this reason, variables such as RM_DTE and q that exhibit larger-scale behavior benefit more from the EnKF while for w, because of its smaller-scale structure, the EnKF appears not to be very effective in reducing errors across all scales.

Finally, preliminary parameter estimation experiments also produce very encouraging results. Two experiments with initial m_c error of 0.2 and 0.65 are conducted for this purpose, both of which result in the successful estimation of the parameter. In both experiments, the mean estimated parameter value consistently converges to the true value of 1.0 by the end of the 72-hour experiment while exhibiting

a satisfactory level of variability. This indicates that a sufficient flow-dependent correlation signal exists between the estimated parameter m_c and the observed variables u, v, and T, leading to the satisfactory performance of the EnKF in retrieving the true parameter value within a 72-hour assimilation experiment. Meanwhile, compared to the worst-case experiment with the wrong mean parameter value and no parameter estimation, the improvement in the overall error reduction throughout the experiment appears not to be very noticeable for the initial parameter error of 0.2, which indicates that when state and model errors are both present, the model uncertainty space is mostly dominated by the state errors (for the stated level of initial parameter error). A confirmation of this hypothesis is also obtained from pure-forecast experiments with the possible combinations of state and model error. When the forecast is initialized with parameter error only (of magnitude 0.2), all model variables exhibit reasonably detectable levels of ensemble spread at 10-30% compared to the forecast with only initial-condition error. However, the spread associated with a forecast initialized with both initial-condition and parameter errors appears to be very similar in magnitude and behavior to that of the forecast with only initial-condition error. This shows, at least for the model error associated with the parameter m_c and a magnitude of 0.2 for its initial error, that the presence of state error suppresses error growth resulting from model error and dominates model uncertainty. Consequently, although the EnKF successfully retrieves the true parameter value, improvement in the reduction of error remains very limited. Nevertheless, the improvement becomes more pronounced when the initial

parameter error is increased to 0.65, when the overall error reduction, compared to the worst case, is 7-8% for RM_DTE and the rms errors of T and q.

It is believed that the preliminary evaluation of the EnKF for simultaneous state and parameter estimation with MM5 is, in general, very successful. A very important achievement is obtained by the satisfactory retrieval of the true parameter value. By itself, this result is significant from several points of view. First and foremost, it shows that a sufficiently strong flow-dependent covariance structure is present between observed model variables and the estimated parameter for a complex numerical weather prediction model, suggesting the prospect that a possible tratment of model error for operational data assimilation could be conceived through ensemble-based parameter estimation. The retrieval of case- and flow-dependent parameter values is also extremely valuable for the testing and validation of the many model parameters, values of which are normally obtained empirically or by trial-and-error. Improvement of numerical models, in this respect, has a direct consequence for deterministic weather forecasting where it is not possible to account for model uncertainties through the probabilistic ensemble approach.

An interesting result pertaining to error characteristics related to parameter estimation is that only minor amounts of improvement in error reduction are achieved with the current configuration and initial error magnitude of 0.2. It should be noted, however, that these results are preliminary and only reflect the response of the MM5 model to a very specific parameter (m_c) and its limited uncertainty space as applied in this study. Nevertheless, one possible explanation for this behavior is linked to the

interaction between the model uncertainty associated with initial conditions versus model error. In the specific configuration adopted for this study, it appears that the covariance structure generated through initial-condition uncertainty may span a phase space with sufficiently high dimension to also account for the limited model error uncertainty generated through the initial perturbation of the parameter m_c. Another possible reason for such behavior may also be linked to the rate at which forecast error responds to model error. The parameter uncertainty examined in this study is associated with the relatively slow diffusive processes in the PBL and thus 12-hour intervals between assimilation steps may not be sufficiently long to allow for a significant divergence to emerge.

The existence of a level of parameter uncertainty to which error growth is not very responsive also suggests that such behavior can possibly be utilized to "calibrate" the acceptable level of parameter variability. In this study, the acceptable level of parameter variability is assumed to be known where a minimum parameter spread of 1/4 of initial parameter spread is imposed. However, sensitivity experiments with the sea breeze model reveal that assimilation performance critically depends on the limiting spread chosen and that this behavior is also parameter-specific. In other words, there is clearly a need to establish the parameter spread limits through a more rigorous analysis so that they represent the actual physical level of parameter variability that does not significantly contribute to forecast error during an assimilation cycle. For the parameter m_c which was the focus of estimation in this study, the initial spread of 1.2 appears to be an example of such a situation, although a more complete analysis of the uncertainty

space associated with this parameter is necessary before decisive conclusions can be drawn.

It should be noted that the presented study regarding parameter estimation for MM5 is based on a limited sample space for a single parameter, m_c. Nevertheless, a rigorous analysis including pure forecasts, perfect-model EnKF experiments, parameter sensitivity, and parameter identifiability are carried out so that the satisfactory results discussed here are the product of a complete investigation despite their limited scope. The method of spatial updating of global parameters is also observed to contribute substantially to the performance of the estimation process. Previously in the discussion of the sea breeze model results, it is argued that a unified "meta-localization" approach for the simultaneous state and parameter estimation might prove necessary for complicated numerical models and is conjectured that a global localization in the correlation space may be a feasible alternative to global updating. It is believed that the devised method of spatial updating of global parameters, although ad hoc in nature, is one further step toward this goal, primarily because the spatial information content of observations and the advantages of localization are now being realized. However, the theoretical implications of this procedure on the correlation space itself and if and how convergence properties can be improved are not addressed in this study. Future directions for research, in this regard, are believed to be multiple. They possibly include expansion of the sampling of model error to a larger parameter uncertainty space (possibly including parameters from different parameterization schemes), investigation of parameter estimation for flow types with different scales and characteristics,

application with real observations, representation of the impacts of spatial localization in the correlation space, and many more.

REFERENCES

Ananthasayanam, M.R., 2000: Fascinating perspectives of state and parameter estimation techniques. *AIAA Atmospheric Flight Mechanics Conference,* Denver, CO, Amer. Inst. Aeronaut. Astronaut., 860-870.

Anderson, J.L., 2001: An ensemble adjustment Kalman filter for data assimilation. *Mon. Wea. Rev.*, **129**, 2884-2903.

——— and S.L. Anderson, 1999: A Monte Carlo implementation of the nonlinear filtering problem to produce ensemble assimilations and forecasts. *Mon. Wea. Rev.*, **127**, 2741-2758.

Anthes, R.A., 1978: The height of the planetary boundary layer and the production of circulation in a sea breeze model. *J. Atmos. Sci.*, **35**, 1231-1239.

——— and T.T. Warner, 1978: Development of hydrodynamic models suitable for air pollution and other mesometeorological studies. *Mon. Wea. Rev.*, **106**, 1045-1078.

Asselin, R., 1972: Frequency filter for time integrations. *Mon. Wea. Rev.*, **100**, 487-490.

Åström, K.J. and P. Eykhoff, 1971: System identification – a survey. *Automatica*, **7**, 123-162.

Atkins, N.T., R.M. Wakimoto, and T.M. Weckwerth, 1995: Observations of the sea-breeze front during CaPE. Part II: Dual-Doppler and aircraft analysis. *Mon. Wea. Rev.*, **123**, 944-969.

Beck, J.V. and K.A. Woodbury, 1998: Inverse problems and parameter estimation: Integration of measurements and analysis. *Meas. Sci. Techol.*, **9**, 839-847.

Bohn, C. and H. Unbehauen, 2001: Sensitivity models for nonlinear filters with application to recursive parameter estimation for nonlinear state-space models. *IEE Proc. – Control Theory Appl.*, **148**, 137-145.

Burgers, G., P.J. van Leeuwen, and G. Evensen, 1998: Analysis scheme in the ensemble Kalman filter. *Mon. Wea. Rev.*, **126**, 1719-1724.

Charney, J.G. and J.G. DeVore, 1979: Multiple flow equilibria in the atmosphere and blocking. *J. Atmos. Sci.*, **36**, 1205-1216.

———, R.G. Fleagle, V.E. Lally, H. Riehl, and D.Q. Wark, 1966: The feasibility of a global observation and analysis experiment. *Bull. Amer. Meteor. Soc.*, **47**, 200-220.

Cox, H., 1964: On the estimation of state variables and parameters for noisy dynamic systems. *IEEE Trans. Automat. Contr.*, **9**, 5-12.

D'Andera, F. and R. Vautard, 2000: Reducing systematic errors by empirically correcting model errors. *Tellus*, **52A**, 21-41.

Dee, D.P., 1995: On the estimation of error covariance parameters for atmospheric data assimilation. *Mon. Wea. Rev.*, **123**, 1128-1145.

——— and A.M. Da Silva, 1998: Data assimilation in the presence of forecast bias. *Quart. J. Roy. Meteorol. Soc.*, **124**, 269-295.

——— and ———, 1999: Maximum-likelihood estimation of forecast and observation error covariance parameters. Part I: Methodology. *Mon. Wea. Rev.*, **127**, 1822-1834.

———, G. Gaspari, C. Redder, L. Rukhovets, and A.M. Da Silva, 1999: Maximum-likelihood estimation of forecast and observation error covariance parameters. Part II: Applications. *Mon. Wea. Rev.*, **127**, 1835-1849.

Derber, J.C., 1989: A variational continuous assimilation technique. *Mon. Wea. Rev.*, **117**, 2437-2446.

Dowell, D., F. Zhang, L. Wicker, C. Snyder, A. Crook, 2004: Wind and temperature retrievals in the 17 May Arcadia, Oklahoma, supercell: Ensemble Kalman filter experiments. *Mon. Wea. Rev.*, **132**, 1982-2005.

Dudhia, J., 1993: A nonhydrostatic version of the Penn State-NCAR mesoscale model: Validation tests and simulation of an Atlantic cyclone and cold front. *Mon. Wea. Rev.*, **121**, 1493-1513.

Emery, A.F., B.F. Blackwell, and K.J. Dowding, 2002: The relationship between information, sampling rates, and parameter estimation models. *J. Heat Transf.*, **124**, 1192-1199.

Etherton, B.J. and C.H. Bishop, 2004: Resilience of hybrid ensemble/3DVAR analysis schemes to model error and ensemble covariance error. *Mon. Wea. Rev.*, **132**, 1065-1080.

Evensen, G., 1994: Sequential data assimilation with a nonlinear quasi-geostrophic model using Monte Carlo methods to forecast error statistics. *J. Geophys. Res.*, **99 (C5)**, 10143-10162.

———, 1997: Advanced data assimilation for strongly nonlinear dynamics. *Mon. Wea. Rev.*, **125**, 1342-1354.

——— and P.J. van Leeuwen, 1996: Assimilation of Geosat altimeter data for the Agulhas Current using the ensemble Kalman filter with a quasigeostrophic model. *Mon. Wea. Rev.*, **124**, 85-96.

Ewald, B., C. Penland, and R. Temam, 2004: Accurate integration of stochastic climate models with application to El Niño. *Mon. Wea. Rev.*, **132**, 154-164.

Feliks, Y., 2004: Nonlinear dynamics and chaos in the sea and land breeze. *J. Atmos. Sci.*, **61**, 2169-2187.

Gaspari, G. and S.E. Cohn, 1999: Construction of correlation functions in two and three dimensions. *Quart. J. Roy. Meteorol. Soc.*, **125**, 723-757.

Gelb, A. (Ed.), 1986: *Applied Optimal Estimation.* The M.I.T. Press, Cambridge, MA.

Ghil, M., 1989: Meteorological data assimilation for oceanographers. Part I: Description and theoretical framework. *Dynamics Atmos. Oceans*, **13**, 171-218.

———, S.E. Cohn, J. Tavantzis, K. Bube, and E. Isaacson, 1981: Applications of estimation theory to numerical weather prediction. *Dynamic Meteorology: Data Assimilation Methods*, L. Bengtsson, M. Ghil, and E. Kallen, Eds., Springer-Verlag, New York, 139-224.

Glielmo, L., R. Setola, and F. Vasca, 1999: An interlaced extended Kalman filter. *IEEE Tran. Automat. Contr.*, **44**, 1546-1549.

Gong, J., G. Wahba, D.R. Johnson, and J. Tribbia, 1998: Adaptive tuning of numerical weather prediction models: Simultaneous estimation of weighting, smoothing, and physical parameters. *Mon. Wea. Rev.*, **126**, 210-231.

Grell, G.A., 1993: Prognostic evaluation of assumptions used by cumulus parameterizations. *Mon. Wea. Rev.*, **121**, 764-787.

Ham, J., 2002: Mesoscale predictability and background error covariance estimation through ensemble forecasting. Unpublished M.S. thesis. Texas A&M University, College Station, TX.

Hamill, T.M. and C. Snyder, 2000: A hybrid ensemble Kalman filter-3D variational analysis scheme. *Mon. Wea. Rev.*, **128**, 2905-2918.

Ho, Y. and B. Whalen, 1963: An approach to the identification and control of linear dynamics systems with unknown parameters. *IEEE Trans. Automat. Contr.*, **8**, 255-256.

Holton, J.R., 1992: *An Introduction to Dynamic Meteorology*. Academic Press, San Diego, CA.

Hong, S.-Y. and H.-L. Pan, 1996: Nonlocal boundary layer vertical diffusion in a medium-range forecast model. *Mon. Wea. Rev.*, **124**, 2322-2339.

Houtekamer, P.L. and H. Mitchell, 1998: Data assimilation using an ensemble Kalman filter technique. *Mon. Wea. Rev.*, **126**, 796-811.

——— and ———, 2001:, A sequential ensemble Kalman filter for data assimilation. *Mon. Wea. Rev.*, **129**, 123-137.

———, L. M. Herschel, G. Pellerin, M. Buehner, M. Charron, L. Spacek, and B. Hansen, 2004: Atmospheric data assimilation with an ensemble Kalman filter: Results with real observations. *Mon. Wea. Rev.*, **133**, 604-620.

Kalman, R.E., 1960: A new approach to linear filtering and prediction problems. *Trans. ASME, J. Basic Eng.*, **82D**, 95-108.

Kalnay, E., 2003: *Atmospheric Modeling, Data Assimilation, and Predictability*. Cambridge University Press, Cambridge, United Kingdom.

Keppenne, C., 2000: Data assimilation into a primitive-equation model with a parallel ensemble Kalman filter. *Mon. Wea. Rev.*, **128**, 1971-1981.

——— and M.M. Rienecker, 2002: Initial testing of a massively parallel ensemble Kalman filter with the Poseidon isopycnal ocean general circulation model. *Mon. Wea. Rev.*, **130**, 2951-2965.

Lee, M.-S. and D.-K. Lee, 2003: An application of a weakly constrained 4DVAR to satellite data assimilation and heavy rainfall estimation. *Mon. Wea. Rev.*, **131**, 2151-2176.

Liu, J.S. and M. West, 2001: Combined parameter and state estimation in simulation-based filtering. *Sequential Monte Carlo Methods in Practice*, Doucet A., N. de Freitas, and N. Gordon, Eds., Springer-Verlag, New York, 197-223.

Ljung, L., 1979: Asymptotic behavior of the extended Kalman filter as a parameter estimator for linear systems. *IEEE Trans. Automat. Contr.*, **24**, 36-50.

Lorenz, E.N., 1963: Deterministic nonperiodic flow. *J. Atmos. Sci.*, **20**, 130-141.

———, 1969a: The predictability of a flow which possesses many scales of motion. *Tellus*, **21**, 289-307.

———, 1969b: Three approaches to atmospheric predictability. *Bull. Amer. Met. Soc.*, **50**, 345-349.

———, 1996: Predictability: A problem partly solved. *Proc. ECMWF Seminar on Predictability*, Vol. I, Reading, United Kingdom, ECMWF, 1-18.

Louis, J.F., 1979: A parametric model of vertical eddy fluxes in the atmosphere. *Bound.-Layer Meteor.*, **17**, 187-202.

Mayne, D.Q., 1966: Parameter estimation. *Automatica*, **3**, 245-255.

Mehra, R.K., 1971: On-line identification of linear dynamic systems with applications to Kalman filtering. *IEEE Trans. Automat. Contr.*, **16**, 12-21.

Miller, R.N., 1986: Toward the application of the Kalman filter to regional open ocean modeling. *J. Phys. Oceanogr.*, **16**, 72-86.

Miller, S.T.K., B.D. Keim, R.W. Talbot, and H. Mao, 2003: Sea breeze: Structure, forecasting, and impacts. *Rev. Geophys.*, **41(3)**, 1011.

Mitchell, H. and P.L. Houtekamer, 2000: An adaptive ensemble Kalman filter. *Mon. Wea. Rev.*, **128**, 416-433.

———, ———, and G. Pellerin, 2002: Ensemble size, balance, and model-error representation in an ensemble Kalman filter. *Mon. Wea. Rev.*, **130**, 2791-2808.

Mitchell, K.E. and J.A. Dutton, 1981: Bifurcations from stationary to periodic solutions in a low-order model of forced, dissipative barotropic flow. *J. Atmos. Sci.*, **38**, 690-716.

Navon, I.M., 1998: Practical and theoretical aspects of adjoint parameter estimation and identifiability in meteorology and oceanography. *Dynamics Atmos. Oceans*, **27**, 55-79.

Nelson, L.W. and E. Stear, 1976: The simultaneous on-line estimation of parameters and states in linear systems. *IEEE Trans. Automat. Contr.*, **21**, 94-98.

Nicolis, C., 2003: Dynamics of model error: Some generic features. *J. Atmos. Sci.*, **60**, 2208-2218.

———, 2004: Dynamics of model error: The role of unresolved scales revisited. *J. Atmos. Sci.*, **61**, 1740-1753.

Niu, S.S. and D.G. Fisher, 1997: Detecting parameter identifiability problems in system identification. *Int. J. Adapt. Control*, **11**, 603-619.

Penland, C., 1996: A stochastic model of IndoPacific sea surface temperature anomalies. *Physica D*, **96**, 534-558.

Rinne, J. and H. Järvinen, 1993: Estimation of the Cressman term for a barotropic model through optimization with use of the adjoint model. *Mon. Wea. Rev.*, **121**, 825-833.

Rotunno, R., 1983: On the linear theory of land and sea breeze. *J. Atmos. Sci.*, **40**, 1999-2009.

Schubert, S. and Y. Chang, 1996: An objective method for inferring sources of model error. *Mon. Wea. Rev.*, **124**, 325-340.

Simpson, J.E., 1994: *Sea Breeze and Local Wind*. Cambridge University Press, Cambridge, Great Britain.

Singer, H., 2002: Parameter estimation of nonlinear stochastic differential equations: Simulated maximum likelihood versus extended Kalman filter and Itô-Taylor expansion. *J. Comput. Graph. Stat.*, **11**, 972-995.

Sivillo, J.K., J.E. Ahlquist, and Z. Toth, 1997: An ensemble forecasting primer. *Wea. Forecasting*, **12**, 809-818.

Sneddon, G., 2000: A statistical perspective on data assimilation in numerical models. *Studies in the Atmospheric Sciences (Lecture Notes in Statistics; 144)*, Berliner, L.M., D. Nychka, and T. Hoar, Eds., Springer-Verlag, New York, 7-21.

Snyder, C. and F. Zhang, 2003:, Assimilation of simulated Doppler radar observations with an ensemble Kalman filter. *Mon. Wea. Rev.*, **131**, 1663-1677.

Talagrand, O., 1997: Assimilation of observations, an introduction. *J. Meteor. Soc. Japan*, **75**, 191-209.

Thompson, P.D., 1957: Uncertainty of initial state as a factor in the predictability of large-scale atmospheric flow patterns. *Tellus*, **9**, 275-295.

Timmer, J., 2000: Parameter estimation in nonlinear stochastic differential equations. *Chaos Soliton. Fract.*, **11**, 2571-2578.

Troen, I. and L. Mahrt, 1986: A simple model of the atmospheric boundary layer; sensitivity to surface evaporation. *Bound.-Layer Meteor.*, **37**, 129-148.

Van Leeuwen, P.J., 1999: Comment on "Data assimilation using an ensemble Kalman filter technique". *Mon. Wea. Rev.*, **127**, 1374-1377.

Vannitsem, S., 2003: Intrinsic error growth in a large-domain Eta regional model. *Mon. Wea. Rev.*, **131**, 2697-2704.

——— and Z. Toth, 2002: Short-term dynamics of model errors. *J. Atmos. Sci.*, **59**, 2594-2604.

Vickroy, J.G. and J.A. Dutton, 1979: Bifurcation and catastrophe in simple, forced, dissipative quasi-geostrophic flow, *J. Atmos. Sci.*, **36**, 42-52.

Vukicevic, T. and R.M. Errico, 1990: The influence of artificial and physical factors upon predictability estimates using a complex limited-area model. *Mon. Wea. Rev.*, **118**, 1460-1482.

Wakimoto, R.M. and N.T. Atkins, 1994: Observations of the sea-breeze front during CaPE. Part I: Single-Doppler radar, satellite, and cloud photogrammetry analysis. *Mon. Wea. Rev.*, **122**, 1092-1114.

Walsh, J.E., 1974: Sea breeze theory and applications. *J. Atmos. Sci.*, **31**, 2012-2026.

Walter, K.R., 2004: The nonlinear dynamics of the sea breeze. 112 pp., M.S. thesis, Texas A&M University, College Station.

Whitaker, J.S. and T.M. Hamill, 2002: Ensemble data assimilation without perturbed observations. *Mon. Wea. Rev.*, **130**, 1913-1924.

Zhang, F., Z. Meng, and A. Aksoy, 2005: Tests of an ensemble Kalman filter for mesoscale and regional-scale data assimilation. *Mon. Wea. Rev.*, in review, manuscript available online at www.met.tamu.edu/personnel/faculty/fzhang.html.

———, C. Snyder, and J. Sun, 2004: Impacts of initial estimate and observations availability on convective-scale data assimilation with an ensemble Kalman filter. *Mon. Wea. Rev.*, **132**, 1238-1253.

Zhu, Y. and I.M. Navon, 1999: Impact of parameter estimation on the performance of the FSU global spectral model using its full-physics adjoint. *Mon. Wea. Rev.*, **127**, 1497-1517.

Zou, X., I.M. Navon, and F.X. Ledimet, 1992: An optimal nudging data assimilation scheme using parameter estimation. *Quart. J. Roy. Meteorol. Soc.*, **118**, 1163-1186.

Zupanski, D., 1997: A general weak constraint applicable to operational 4DVAR data assimilation systems. *Mon. Wea. Rev.*, **125**, 2274-2292.

Zupanski, M., 1993: Regional four-dimensional variational data assimilation in a quasi-operational forecasting environment. *Mon. Wea. Rev.*, **121**, 2396-2408.

VITA

Altug Aksoy
Department of Atmospheric Sciences, Texas A&M University
College Station, TX 77843-3150

Education

M.B.A. (January 1994) - School of Business and Public Management, *The George Washington University*, Washington, DC

B.S. in Mechanical Engineering (July 1991) - Department of Mechanical Engineering, *Boğazici University*, Istanbul, Turkey

Experience

Research Assistant (2002 – 2005) - Department of Atmospheric Sciences, *Texas A&M University*

Student Visitor (July 2003) - *National Center for Atmospheric Research*, Boulder, Colorado

Instructor (Fall 2002) - Department of Atmospheric Sciences, *Texas A&M University*

Teaching Assistant (Spring and Fall 2001) - Department of Atmospheric Sciences, *Texas A&M University*

Graduate Assistant (Spring 2000) - Department of Geography, *Texas A&M University*

Inspector (August 1994 - July 1999) - Inspection Board, *Istanbul Stock Exchange*, Istanbul, Turkey

Honors and Awards

College of Geosciences Graduate Excellence Scholarship, August 2003, *Texas A&M University*

Mr./Mrs. Kenneth P. Pike Fellowship, August 2002, *Texas A&M University*

Honor Degree for the 5th Rank in Graduating Class of 1991, *Boğazici University*